Determining the Jet Energy Scale for ATLAS in the Z+Jet Channel

by

Sundeep Singh

B.Sc., University of British Columbia, 2016

Thesis Submitted in Partial Fulfillment of the
Requirements for the Degree of
Master of Science

in the
Department of Physics
Faculty of Science

SIMON FRASER UNIVERSITY
Fall 2020

Declaration of Committee

Name:	**Sundeep Singh**
Degree:	**Master of Science**
Thesis title:	**Determining the Jet Energy Scale for ATLAS in the Z+Jet Channel**
Committee:	**Chair:** Malcolm Kennett Associate Professor, Physics
	Michel Vetterli Supervisor Professor, Physics
	Bernd Stelzer Committee Member Professor, Physics
	Matthias Danninger Examiner Assistant Professor, Physics

Abstract

This thesis presents a determination of the jet energy scale for the ATLAS detector using in-situ measurements. This calibration is critical, as jets are found in many analyses, and the energy measurement of jets contributes significantly to the uncertainty in numerous ATLAS results. The energy of the jet is initially taken to be the detector measurement, but this is lower than the true energy because the detector is calibrated for electromagnetic particles, not jets. One can find a correction to this energy by balancing the jet's transverse momentum against a well-measured reference object. Directly calibrating the calorimeter-level jet to the particle-level is called Direct Balance; here, a different method called the Missing E_T Projection Fraction (MPF) method is used instead, which balances the p_t of the recoiling system against the reference object. The MPF's pile-up resistant nature makes it more suitable to use in the ATLAS environment. Results for the MPF method in the $Z + Jet$ channel are presented. A relative calibration of data to Monte Carlo simulation is provided, including a complete systematic uncertainty analysis. The uncertainty on the in-situ calibration is reduced to around 1% for most transverse momenta.

Keywords: Simon Fraser University; ATLAS; Jet Energy Scale

Table of Contents

List of Figures

List of Tables

Chapter 1

Introduction

1.1 Physics

The purpose of physics is to describe nature and how it works. This task encompasses everything, ranging from the smallest distances and energies to the largest. Over the past 40-50 years, the Standard Model of particle physics (SM) has been used successfully to describe three of the four fundamental forces: the electromagnetic, weak, and strong forces. However, it does not include the gravitational force. The Standard Model also identifies the known elementary particles. Despite the missing description of gravity, the Standard Model is one of the pillars of modern science.

It is possible to classify particles by their statistical behavior: those that obey Fermi-Dirac statistics and ones that obey Bose-Einstein statistics. These are called fermions and bosons, respectively. The elementary matter particles are fermions, while force-carriers are bosons. Fermions are further separated into leptons and quarks (shown in table 1.1) due to quarks having color charge and undergoing strong interactions; this is analogous to how electrons feel the electromagnetic force due to the presence of electric charge. The strong force differs from familiar forces in the way that it behaves as a function of distance. For the strong force, the energy of interaction is the sum of two terms. The first is proportional to the distance between two colored objects: $E \propto r$ (this dominates at large distances). The second is a Coulomb-like potential that goes as $E \propto r^{-1}$ (this term dominates at small distances) [58]. At large distances, the potential results in the phenomenon of colour confinement and the formation of jets, as will be outlined later. This behaviour is in contrast with the familiar electromagnetic force, which goes as $E \propto r^{-1}$ for all r.

The electron, electron neutrino, up-quark, and down-quark constitute the first generation. There are second and third generations, which are comprised of similar particles that are heavier (for example, the muon can be seen as a more massive electron).

Quarks combine to form hadrons. There are two types of hadrons: baryons and mesons. In the simplest models, baryons consist of three valence quarks, and mesons are comprised of a quark and an anti-quark. Baryons are fermions, while mesons are bosons. The proton is a baryon, having two up and one down valence quarks. It also has a sea of quark-antiquark pairs and gluons in addition to the valence quarks. The constituents of hadrons are called *partons*.

fermion	mass [GeV]	spin	electric charge	colour charge	generation
charged leptons					
e	5.11 x10^{-4}	$\frac{1}{2}$	-1	no	1
μ	1.06 x10^{-1}	$\frac{1}{2}$	-1	no	2
τ	1.78	$\frac{1}{2}$	-1	no	3
neutral leptons					
ν_e	0	$\frac{1}{2}$	0	no	1
ν_μ	0	$\frac{1}{2}$	0	no	2
ν_τ	0	$\frac{1}{2}$	0	no	3
up-type quarks					
u	2.3 x10^{-3}	$\frac{1}{2}$	$+\frac{2}{3}$	yes	1
c	1.28	$\frac{1}{2}$	$+\frac{2}{3}$	yes	2
t	173.5	$\frac{1}{2}$	$+\frac{2}{3}$	yes	3
down-type quarks					
d	4.8 x10^{-3}	$\frac{1}{2}$	$-\frac{1}{3}$	yes	1
s	9.5 x10^{-2}	$\frac{1}{2}$	$-\frac{1}{3}$	yes	2
b	4.18	$\frac{1}{2}$	$-\frac{1}{3}$	yes	3

Table 1.1: [46]. Basic properties of the SM fermions. Note that the neutrino masses are not zero, but they are extremely small and can effectively be taken as zero for the purpose of this thesis. [58]

The spin-1 bosons are responsible for mediating the fundamental forces, meaning that two particles interacting via a force exchange the corresponding boson. This idea differs from the action-at-a-distance view of classical physics. Instead, it is a discretized particle exchange, in which the distance interaction consists of two local interactions. The bosons in the Standard Model are [58]:

- γ : Mediates the electromagnetic force.
- $W^{\pm}$: Carries the weak force.
- Z : Carries the weak force.
- Gluon : Carries the strong force.

- Higgs boson: Fundamentally different, as it has spin 0 and does not carry a force.

  Responsible for giving elementary particles mass.

Table 1.2 shows some properties of the Standard Model bosons. The work presented in this thesis is concerned with quarks, gluons, and the Z boson (which is studied via its decay to $Z \to ee^+/\mu\mu^+$).

interaction	boson	mass [GeV]	spin	electric charge	colour charge
force carrying bosons					
Electromagnetic	γ (photon)	0	1	0	no
Weak	$W^{\pm}$	80.39	1	±1	no
	Z	91.19	1	0	no
Strong	g (gluon)	0	1	0	yes
non-force carrying bosons					
-	Higgs	125.09	0	0	no

Table 1.2: [41]. The bosons of the Standard Model, consisting of spin-1 bosons, which are responsible for mediating forces, and the spin-0 Higgs, which gives elementary particles mass.

When two protons collide with each other, the dynamics of the interaction depend on the energy of the collision. The energy regimes are set by the de Broglie wavelength of the colliding protons. If the beam energy is low, resulting in a wavelength that is long relative to the size of the proton, the electromagnetic interaction strength and the macroscopic properties of the protons determine the dynamics of the event. However, if the energy is high (meaning the de Broglie wavelength of the protons is on the order of or smaller than the proton size), the parton-level properties determine the interaction [54, 58]. By raising the energy to this regime, the interaction becomes akin to colliding groups of quarks/gluons together. In this way, one can study a qq (or qg/gg) interaction (the *Parton Distribution Function* - detailed later - describes how the momentum of the particle is distributed amongst the quarks/gluons). This is the only way to study parton-parton collisions because isolated quarks do not exist in nature due to color confinement [58]. Color confinement is the phenomenon that particles carrying the color charge cannot be isolated; they must come in colorless combinations due the distance behaviour of the strong force. At the LHC, high energies are provided by the 6.5 TeV proton beams. This thesis presents studies of pp (qq, qg, or gg) interactions which result in a Z+jet event topology (to be detailed later).

At high energy, proton-proton collisions produce quarks and gluons. Because the strong force increases with distance, quarks spontaneously emit gluons, which split into $q\bar{q}$ pairs. These subsequent quarks emit gluons, and this iterative process continues until the energies

are low enough that resulting quarks and anti-quarks form colorless combinations instead of emitting further gluons. Since the initiating quark had significant momentum, the resulting particles are boosted in the initial direction, which results in the production of a collimated spray of particles called a *jet*.

The process through which a quark evolves into a jet is called fragmentation. The fragmentation process can be divided into two different stages. The first is called *parton showering*, which is the process detailed above wherein the quarks emit gluons, which then split into $q\bar{q}$ pairs, and the process continues until the energies are low enough to initiate the next step. This second step is called *hadronization*, which is the process where low energy quarks combine into colorless combinations and produce hadrons (composite particles of quarks and anti-quarks). The strong force is described by Quantum Chromodynamics (QCD), which is *non-perturbative* at low-energies (energies at which the hadronization process occurs), but can be treated perturbatively at high-energies (the regime in which parton showering occurs) [58]. This stems from the coupling constant of the strong force being greater than 1 at lower energies but dropping below 1 at high energies. The key difference between the two stages is that the parton shower can be calculated in principle (due to being able to treat QCD perturbatively), while the hadronization must be modeled (as QCD is non-perturbative at low energies). A schematic of a parton shower is shown in figure 1.1. To be more specific, this is a quark-initiated jet, or simply a quark jet. A gluon can also undergo the fragmentation process, resulting in a gluon-initiated jet. A validation of the energy calibration of jets is presented in this thesis.

At ATLAS, the energy calibration is determined through Monte Carlo simulation and is validated by data and in-situ measurements. The idea is to look for events in which a quark (or a gluon) and a Z boson are produced from the collision (Feynman diagrams for which can be seen in figures 3.7 and 3.8), and use momentum conservation in the transverse plane to determine the true energy of the jet by using the Z boson as a reference. The Z boson can be identified by its decay via the $Z \to e^+e^-/\mu^+\mu^-$ processes. Quark jets dominate in the $Z+jet$ topology. The selected events (see the *Event Selection* subsection in the *Methods* chapter) are of the form $qg \to q(Z|\gamma)$, or $q\bar{q} \to g(Z|\gamma)$. The former is more prevalent as qg interactions are more abundant than $q\bar{q}$ due to the existence of eight gluon colors (in contrast to the three quark colors).

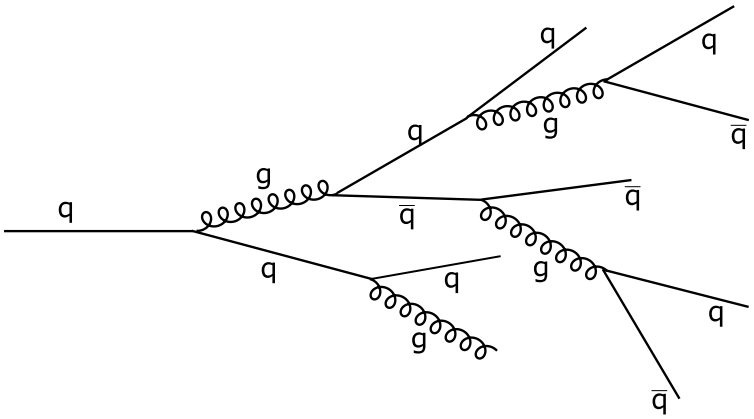

Figure 1.1: When a quark is scattered from the proton-proton collision, it can emit a gluon. This gluon can, in turn, decay into a quark-antiquark pair. These quarks can then continue to emit gluons, and the process repeats. When the momentum is low enough, the quarks form colorless combinations, resulting in a collimated spray of particles known as a jet. Note that a gluon can also initiate the jet.

1.2 Objectives and Motivation

The primary purpose of the research presented here is to determine the *Jet Energy Scale* (JES), and to improve on previous calibrations by reducing systematic uncertainties. The primary detector component considered is the calorimeter, the purpose of which is to absorb particles in order to measure their energy (more details in chapter 2.3). The jet reconstruction algorithm groups together objects (energy depositions in the calorimeter or particle trajectories, for example). When the jet is simply the sum of individual particles as measured by the calorimeter, it is called an Electromagnetic Topocluster jet (an EMTopo jet). Jets can also be reconstructed using a combination of the trajectories of the particles and the calorimeter measurements (called Particle Flow jets, abbreviated as PFlow jets). Both methods, however, do not measure the true energy of the jet as there is energy lost to nuclear interactions in the calorimeter (which are poorly measured), dead regions of the detector, jets not fully contained in the calorimeter, and other effects (see the *Expected Outcome* section in the *Methods* chapter for more details). The JES provides a factor that is applied to measured jet energies to correct for these effects. This task can be broken down into two parts.

First is the provision of the jet response as a function of the momentum. The response is defined as

$$R = \frac{E_{measured}}{E_{truth}} \tag{1.1}$$

For the reasons listed above, it is known that $E_{measured}$ will be smaller than the jet energy ($R < 1$). It is expected that with higher momenta, the response improves (see the *Expected Outcomes* section for more detail). Thus, the response is given as a function of the momentum of the jet. These response curves are derived for data as well as Monte-Carlo (MC) simulations. In the jet calibration chain (see the *Jet Calibration Chain* section), there are corrections to the energy and direction of jets that are based on MC simulations. This calibration assumes that the MC perfectly describes the data, which is shown to be incorrect (see the *Results* chapter). Therefore, the jet energy from either MC or data must be corrected to match the other. ATLAS corrects data to match the MC, and this correction is the relative in-situ calibration shown in this thesis. The data are corrected because the MC tracks the difference between processes (quark vs gluon jets for example), while the in-situ calibration tests mainly quark jets.

The second task is a full analysis of the systematic uncertainties on the calibration. A systematic source of error (called a systematic for short) is intrinsic to the system. Each source of systematic uncertainty is varied, and the effect of this variation on the calculated response is taken as an uncertainty. This process needs to be done for each systematic, and a total uncertainty is then derived.

The main goals of the research presented here are:

- To provide an in-situ jet energy calibration using the 2015-2017 data and the new MC samples.
- To improve on past uncertainties.

These are essential tasks as jets are always produced in LHC collisions, and so affect many different analyses. By providing a calibration with small uncertainties, many ATLAS physics results improve.

1.3 Overall Thesis Structure

In this thesis, the steps taken in the derivation of the jet energy scale will be clearly outlined. First, a description of the detector and data is presented in Chapter 2. After this, jets and related physics are discussed in chapter 3. The software will be briefly discussed in chapter 4, and can be skipped without loss of continuity. The results are presented in chapter 5, followed by conclusions in chapter 6.

Chapter 2

The Experiment: ATLAS and the LHC

2.1 Design Considerations and Layout

2.1.1 Motivation

The research presented here relies on collisions recorded at the Large Hadron Collider (LHC), which is a particle accelerator that lies on the border of Switzerland and France. It is located in an underground tunnel at a depth ranging from 50 m to 175 m, and is 26.7 km in circumference. It comprises two rings that accelerate protons in opposite directions, with steering magnets throughout the ring to bend the protons in the circular path and focussing magnets to keep the beam from diffusing. The protons are accelerated in bunches to nearly the speed of light, and collide at four points around the ring that are enclosed in straight sections. The spacing between bunch crossings is 25 ns, and the design collision rate is 23 interactions per crossing [13], although this has gone up with increased luminosity. *Luminosity* is the number of incident particles per time per area, and when multiplied by the probability (cross-section) of a process, yields the rate of production. The interaction (collision) points (IPs) are set by crossing the rings at four different locations. There are extra steering and focusing magnets at each interaction point to ensure maximal collision rate. There is a detector at each IP [54, 55, 22]. The four detectors are ATLAS (AToroidal LHC ApparatuS), CMS, ALICE, and LHC-B. The analysis presented in this thesis uses data taken by the ATLAS detector.

When discussing the energy/momentum of particles, the direction transverse to the beam is used. The initial momentum of the proton along the beam is known. However, the distribution of the momentum of the partons in the proton is determined by proton structure functions, more often referred to as *Parton Distribution Functions* (PDF). The momentum of a particular parton in a particular collision is therefore not known. On the other hand, the initial momentum in the transverse direction is small (on the order of MeV

compared to the typical GeV scales at ATLAS), and can be neglected. In an event, the sum of all the transverse energy/momentum components should be negligible, and is assumed to be zero. If there is a significant component, it signifies something that was not measured (in this thesis, the missing energy is attributed to the mismeasurement of the jet energy, explained in detail later).

The design of the ATLAS detector was motivated by various physics goals [2]. The primary benchmark is the search for the Standard Model Higgs boson [40] and the need to probe the electroweak scale [14]. The mass of the Higgs m_H was expected to be greater than 80 GeV and less than 1 TeV. To be sensitive to the entire possible range of m_H, the detector was designed to be sensitive to the following processes (where ℓ means an electron, muon, or tau):

$H \rightarrow \gamma\gamma$
- which covers 80 GeV $< m_H <$ 150 GeV

$H \rightarrow ZZ^* \rightarrow 4\ell^{\pm}$
- which covers 130 GeV $< m_H <$ $2m_z$

$H \rightarrow ZZ \rightarrow 4\ell^{\pm},\ 2\ell^{\pm}2\nu$
- which covers $2m_z < m_H <$ 800 GeV

$H \rightarrow WW,\ ZZ \rightarrow \ell^{\pm}\nu\ 2jets,\ 2\ell^{\pm}\ 2jets,\ 2\ell^{\pm}2\nu,\ 4\ell^{\pm}$
- which covers $m_H <$ 1 TeV

The branching ratios (probabilities for decay channels) of the Higgs boson are shown in figure 2.1. The expected cross-sections for the Higgs boson production are small, requiring high luminosities.

The ATLAS detector is a general-purpose detector and has benchmarks set by other physics searches as well. A second such motivation is a search for particles of the Minimal Supersymmetric Standard Model [2, 34]. This model requires sensitivity to additional processes such as:

$A \rightarrow \tau^+\tau^- \rightarrow e\mu\ plus\ \nu's$

$H^{\pm} \rightarrow \tau^{\pm}\nu$

$H^{\pm} \rightarrow 2\ jets$

$H \rightarrow \tau^+\tau^-$

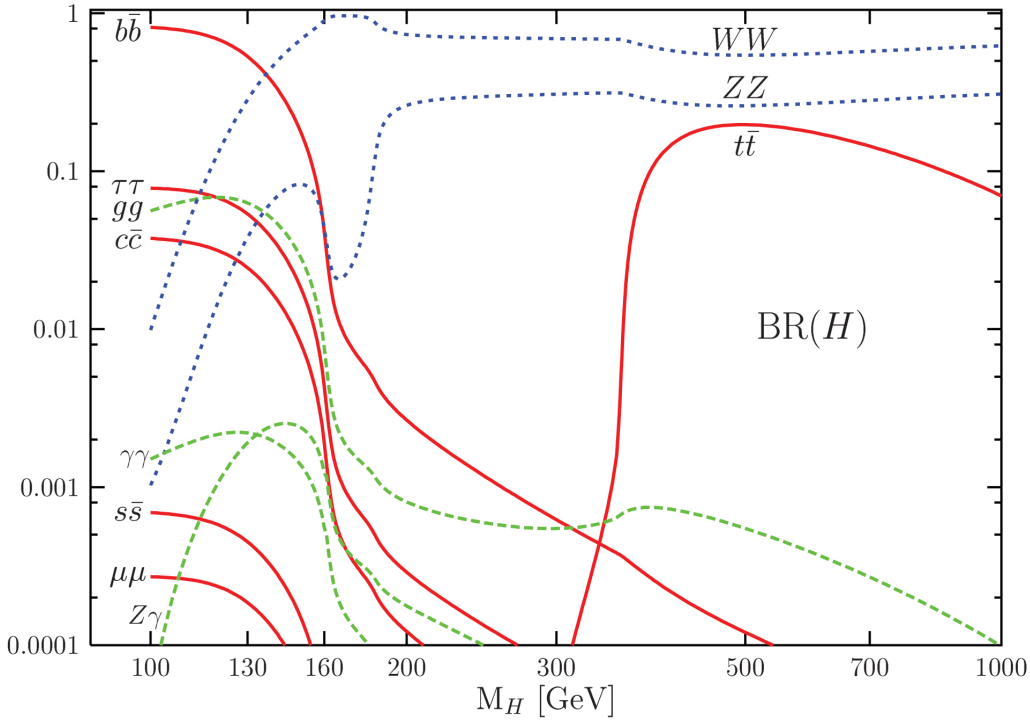

Figure 2.1: [36] The branching ratios of the decay channels of the Higgs boson.

where A and $H^{\pm}$ are extra Higgs bosons seen in this model. There are other motivators for the ATLAS design, which are not discussed here for the sake of brevity. Due to the required sensitivity to various process signatures, the design considerations are [2, 13]:

- Good electromagnetic calorimetry is needed for energy measurements, and electron/photon identification. High granularity allows for precise measurement of jet radii, as well as discrimination between single photons and two close photons from the neutral pion decay $\pi^0 \to \gamma\gamma$ (this is done in the first layer of the EM calorimeter).
- In order to measure jet energies well, good hadronic calorimetry is required. Hadronic showers (detailed later) are driven by nuclear interactions, and have wide/long profiles.
- Efficient tracking at high luminosities is needed to measure charged-particle momenta, as well as provide better particle identification in the ATLAS environment.
- Precision muon momentum measurements, and the requirement of a stand-alone muon measurement at high luminosities.
- Efficient measurement and triggering of low momentum particles. The trigger system determines if the event is of interest, and when the detector should store the data (more details in chapter 2.5).

2.1.2 Coordinate System and Nomenclature

Due to the cylindrical geometry of ATLAS, the following coordinate system is used (shown in figure 2.2).

- The x-axis points towards the center of the LHC.
- The y-axis points up.
- The z-axis is along the beam, and requiring right-handed coordinates sets the direction.
- The azimuthal angle ϕ is measured around the beam axis in the x-y plane with $\phi = 0$ at the x-axis.
- The polar angle θ is measured from the z-axis. This also defines the derived pseudorapidity, which is $\eta = -\ln(\theta/2)$. Pseudorapidity is used instead of θ because differences in η are *invariant* under Lorentz boosts, while differences in θ are not. Highly boosted topologies are often encountered due to the high energy of the collisions, and a measurement system that is impervious to these effects is necessary.

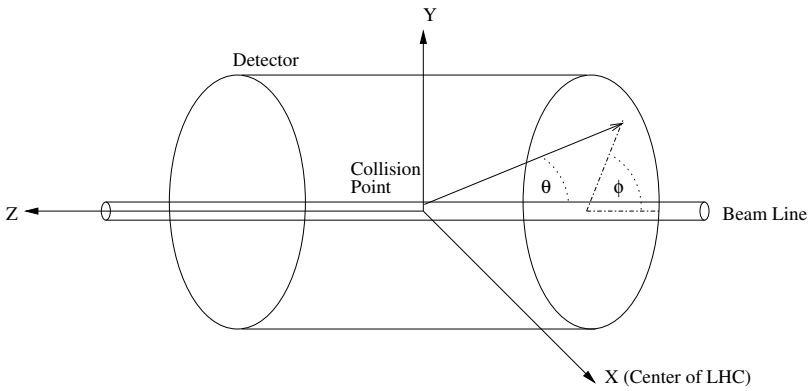

Figure 2.2: The coordinate system used for the ATLAS detector [53]. The beams are incident along the z-axis with a collision point set at the center. The x-axis points towards the center of the LHC, the y-axis points up, and the z-axis is along the beam with the direction defined by requiring the coordinate system to be right-handed. The azimuthal angle ϕ is defined around the beam axis, and the polar angle θ is measured from the z-axis.

2.1.3 Layout

The ATLAS detector is comprised of a large number of detector subsystems, for which an overview is shown in figure 2.3.

The three main sections of the detector are:

1. Inner Detector

   The Inner Detector is closest to the interaction point. The primary purpose of this system is to measure the trajectory of particles emerging from the proton-proton collisions. Typically, around 36 space points are measured for each particle in the Inner Detector [13]. The fit to the collection of trajectory points associated with a particle is called a *track*. The tracking system is enclosed in a solenoidal magnet, which bends charged particles. The combination of the magnetic field and the tracking system allows for the measurement of the momentum and charge of particles. The charge determines the direction in which a particle deflects in a magnetic field; positive particles deflect one way, negative particles bend the other way. The momentum of the particle determines the radius of curvature of the trajectory. The track measurement is non-destructive and interferes negligibly with the particles and minimally affects measurements by subsequent detector systems (however, multiple scattering can be a noticeable effect). High precision is needed in the tracking system to untangle the large number of particles present at high luminosities. By placing the Inner Detector close to the interaction point, a better measurement of the IP and the scattering angle is achieved. Even though the default location of the interaction is defined as the center of the detector, the actual IP can be displaced from this due to the sizeable longitudinal overlap of the two proton beams. The actual collision point is called the *vertex*, and the Inner Detector must be close to the interaction point to reconstruct the vertex accurately. The tracking system comprises three separate systems: the pixel detector, the semiconductor-strip tracker, and the transition radiation tracker. See reference [3] for more details.

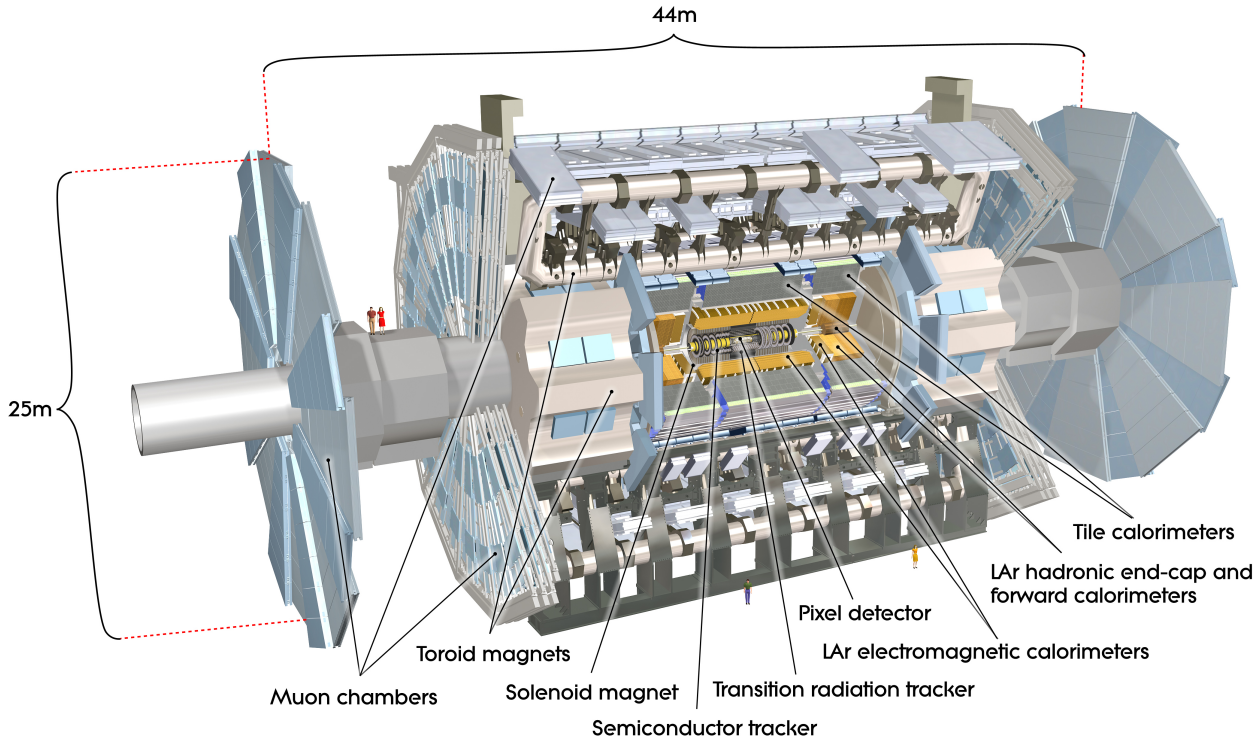

Figure 2.3: A view of the ATLAS detector, courtesy of CERN [50]. The detector consists of three main sections: the inner detector, the calorimeters, and the muon spectrometer. The inner detector consists of a pixel detector, a semiconductor tracker, and a transition radiation tracker. These together provide track information. The inner detector is surrounded by a solenoidal magnet, which provides a constant magnetic field in the tracker (excluding fringes). The calorimeter has electromagnetic and hadronic sections. Calorimetry absorbs the particle in order to measure its energy. The muon spectrometer encloses the entire setup, and is designed to measure the muons that survive through the calorimeters. The toroidal magnet system lies in the muon spectrometer and bends the muons in order to measure their momentum and charge [39, 41, 54, 22].

2. Calorimeter

The purpose of this system is to measure the energy of particles. In order to do this, the particle is absorbed, making calorimetry a fundamentally destructive measurement [39]. The calorimeter is therefore placed outside of the Inner Detector, as it ends the paths of and absorbs most particles (except muons, neutrinos, and exotic particles). Particles that enter a calorimeter go through an iterative process known as *showering* [16, 41]. The particles interact with the material, producing more particles, which in turn propagate through the calorimeter. These products undergo interactions, and this chain reaction continues until the energy of the resultant particles is low enough to be absorbed via ionization.

Calorimeters can be classified into two types: sampling and homogenous. Sampling calorimeters contain many alternating layers: the active layer and the absorber. The absorber is optimized to cause showers in a small space, while the active sections are optimized to measure energy depositions. The energy measured is proportional to the shower produced predominantly in the absorber. The active sections "sample" the shower. A homogenous calorimeter is made of one material that both generates the shower and measures the energy of the resulting particles. The advantage is that the full shower is measured so that the energy resolution is typically better. On the other hand, a sampling calorimeter is cheaper, and the quicker development of showers in the absorber results in a smaller volume.

Depending on the particle being measured, two types of showers exist. Electromagnetic showers are caused by electromagnetic processes and have a resulting profile that is short/narrow, and measure electrons and photons. Hadronic showers are caused predominantly by nuclear interactions, and are wide/long, and measure hadrons [39]. The calorimeter system is therefore divided into two sections that are optimized for each shower type: the Electromagnetic Calorimeter and the Hadronic Calorimeter. The EM calorimeter is a sampling calorimeter with a lead absorber and liquid Argon (LAr) as the active material [13]. It is highly granular in order to make a good measurement of the smaller electromagnetic showers, and the first layer is segmented enough to discriminate between two close photons (to distinguish $\pi^0 \to \gamma\gamma$ from a single photon). The Hadronic Calorimeter, which completes the measurement of hadronic showers, is located outside the Electromagnetic Calorimeter. It is also a sampling calorimeter, but the materials differ depending on the η region. In the central part of the de-

tector ($\eta < 1.7$), steel is used as the absorber material, and plastic scintillator tiles are used as the active material. Outside this η region, LAr calorimeters are chosen due to their intrinsic radiation-hardness. The region $1.5 < \eta < 3.2$ defines the hadronic end-cap calorimeter (HEC), while $3.1 < \eta < 4.9$ is covered by the high-density forward calorimeter (FCAL) [13]. These use liquid argon as the active material, and copper as the absorber, except for the hadronic section of the FCAL, where the absorber is tungsten. Since the calorimeter system is used for energy measurements, it is the component of the detector that the research presented in this thesis most heavily uses. It is shown later that the showering process is critical to the shape of the calorimeter response curves.

3. Muon Spectrometer

The Muon Spectrometer (MS) is located outside the calorimeters. The purpose of the MS is to measure the momentum of muons. At the energies relevant to this work, these are minimum ionizing particles (MIPs), which means that their energy loss rate is minimal (in contrast to other particles that can deposit a significant amount of their energy through electromagnetic processes) [39]. This is because they do not interact strongly and are too heavy to emit significant bremsstrahlung, except at very high energies. Bremsstrahlung is one of the primary electromagnetic methods of energy deposition in calorimeters. Therefore, muons survive through the Inner Detector and the calorimeter. Thus, in order to measure muons, a separate system is needed. The Muon Spectrometer - like the Inner Detector - is also a tracker. It has a large system of superconducting air-core toroid magnets and a dedicated tracking system [13, 22]. Muon identification is easily accomplished, as any isolated particle present in the Muon Spectrometer is tagged as a muon (although energy can leak through the calorimeter into the MS for a small number of showers, notably for high-energy jets). As with the Inner Detector, the charge and momentum of the muons are inferred by analyzing the measured trajectories. Four detector technologies are implemented in the tracking system: thin gap chambers, resistive plate chambers, monitored drift tubes, and cathode strip chambers [39]. Details are given in chapter 2.4.

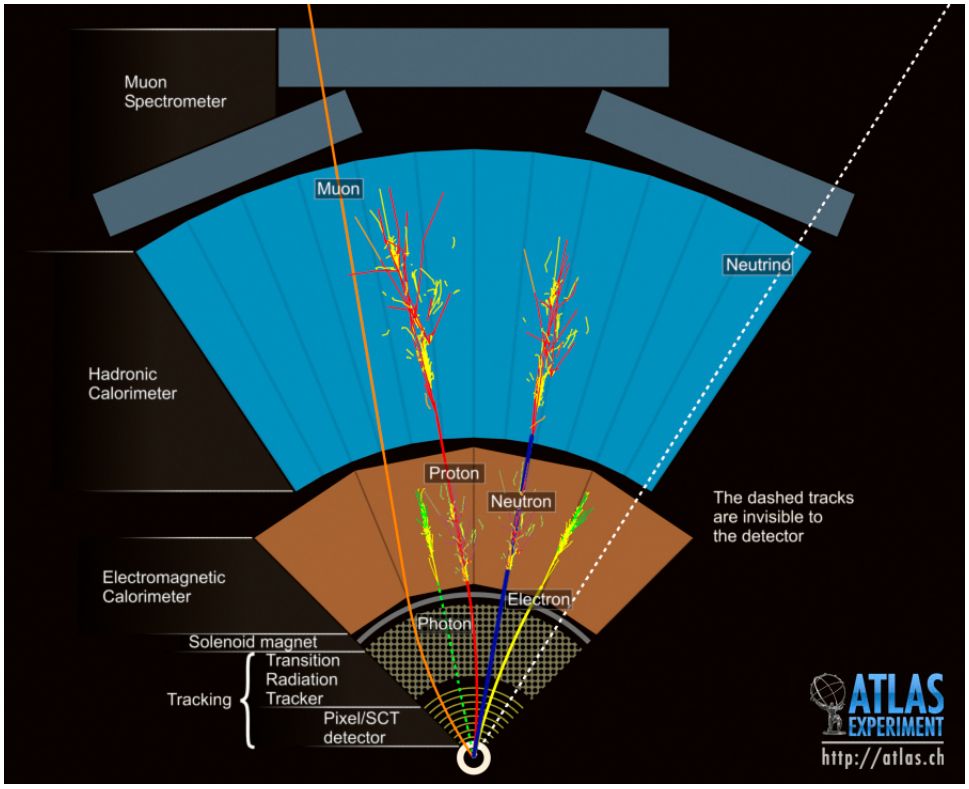

Figure 2.4: A cross sectional view of a portion of the ATLAS detector, courtesy of CERN [51]. Shown are the three sections of the ATLAS detector: the Inner Detector (labelled tracking), the calorimeter system (electromagnetic and hadronic calorimeters), all surrounded by the muon spectrometer.

A cross-sectional view of a portion of the ATLAS detector is shown in figure 2.4. The layout and design were motivated by the physics described earlier.

2.2 Inner Detector

A charged particle that passes through a magnetic field is deflected based on a few parameters: the strength of the magnetic field, the charge of the particle, and the momentum. The radius of the curved trajectory is

$$R = \frac{\gamma p}{qB} \tag{2.1}$$

where γ is the Lorentz factor. If one measures the trajectory of the particle and calculates the radius of curvature, the momentum and direction of the particle can be deduced. That is the role of the Inner Detector. The ID is enclosed in a large solenoidal magnet that provides a constant magnetic field (excluding fringe effects). The tracking system must be able to distinguish a large number of particles with high precision, as the LHC runs in high luminosity conditions. Semiconductor detectors are used due to their good position resolution and high-rate capability. There are two semiconductor technologies implemented in the Inner Detector: the silicon microstrip tracker (SCT), and the pixel detector [13]. The latter is placed closest to the interaction point due to its high granularity, which is necessary for vertex reconstruction. As a charged particle passes through a semiconductor detector, it produces electron-hole pairs, which is a measurable signal. The segmentation allows for high precision trajectory measurements. The Pixel detector has 80 million pixels over an area of 1.7 m^2. The pixel size is 50×400 μm^2 with a resolution of 12×66 μm. The semiconductor sensors are segmented in two dimensions, with advanced electronic methods of reading out the channels (such as readout interconnections and large-area radiation-hardened readout chips with data buffering systems) [13]. The SCT has 6 million channels distributed over 60 m^2. There are readout strips every 80 μm (strips are used here to lower the number of channels as the area has dramatically increased), resulting in a precision of 16 μm in the direction transverse to the strips, and 580 μm along the strips [13]. At the start of run 2, the *Insertable B-Layer* (IBL) was added in as the layer closest to the interaction point [57]. It is also a pixel detector, with 12 million pixels that are 50×250 μm^2 each. These are the layers of the Inner Detector used for high precision. Due to the high cost of semiconductor technology, another type of technology is used at larger radii [13].

The Transition Radiation Tracker (TRT) [44] is outside the semiconductor trackers. The TRT has 350,000 straw drift tubes that are 4 mm in diameter (50,000 straws in the barrel that have both ends read out, and 250,000 straws in both endcaps). The drift tubes have 30 μm diameter gold-plated tungsten wires at their centre, and are filled with a 70-27-3 % mixture of $Xe - CO_2 - O_2$ gas. The straw tubes are weaved with polypropylene foils. When

a charged particle passes through a foil layer, it has a probability to produce a photon. A charged particle moving towards a boundary induces a charge, which can be treated as a mirror charge. The particle and its mirror charge produce an varying electric dipole, and a resulting electromagnetic field. When the particle moves across the boundary, the field changes and disappears, resulting in the emission of X-rays. The transition radiation energy is proportional to the Lorentz factor γ, and is typically on the order of 10 KeV, but for minimum ionizing particles it is around 2 KeV (this is dependent on the relativistic γ factor)[39]. This can be used to discriminate between lighter/heavier particles by studying how many photons are produced. For example, the TRT helps discriminate electrons from pions by counting the number of hits, as well as the number of hits passing a high threshold (HT hits). The fraction of HT hits provides a variable that has 90% electron ID efficiency [43]. By reading out hits along the particle trajectory as well as analyzing the transition radiation, the TRT provides a measurement of the trajectory as well as particle ID. The TRT has 350,000 readout channels over a volume of 12 m^3.

The tracking system works with the solenoidal magnet that encloses the Inner Detector. This magnet provides a constant magnetic field of 2 T through the tracking systems in order to bend the charged particles. The layout of the Inner Detector can be seen in figure 2.5, with some parameter information given in table 2.1.

System	Position	Area (m^2)	Resolution $\sigma(\mu$m)	Channels 10^6	η coverage
Pixels	1 removable barrel layer (B-layer)	0.2	$R\phi = 12$, $z = 66$	16	$\pm$2.5
	2 barrel layers	1.4	$R\phi = 12$, $z = 66$	81	$\pm$1.7
	5 end-cap disks on each side	0.7	$R\phi = 12$, $z = 77$	43	$\pm$1.7-2.5
Silicon Strips	4 barrel layers	34.4	$R\phi = 16$, $z = 580$	3.2	$\pm$1.4
	9 end-cap wheels on each side	26.7	$R\phi = 16$, $z = 580$	3.0	$\pm$1.4-2.5
TRT	Axial barrel straws		170 (per straw)	0.1	$\pm$0.7
	Radial end-cap straws		170 (per straw)	0.32	$\pm$0.7-2.5
	36 straws per track				

Table 2.1: Parameters for the Inner Detector components (IBL not included) [13].

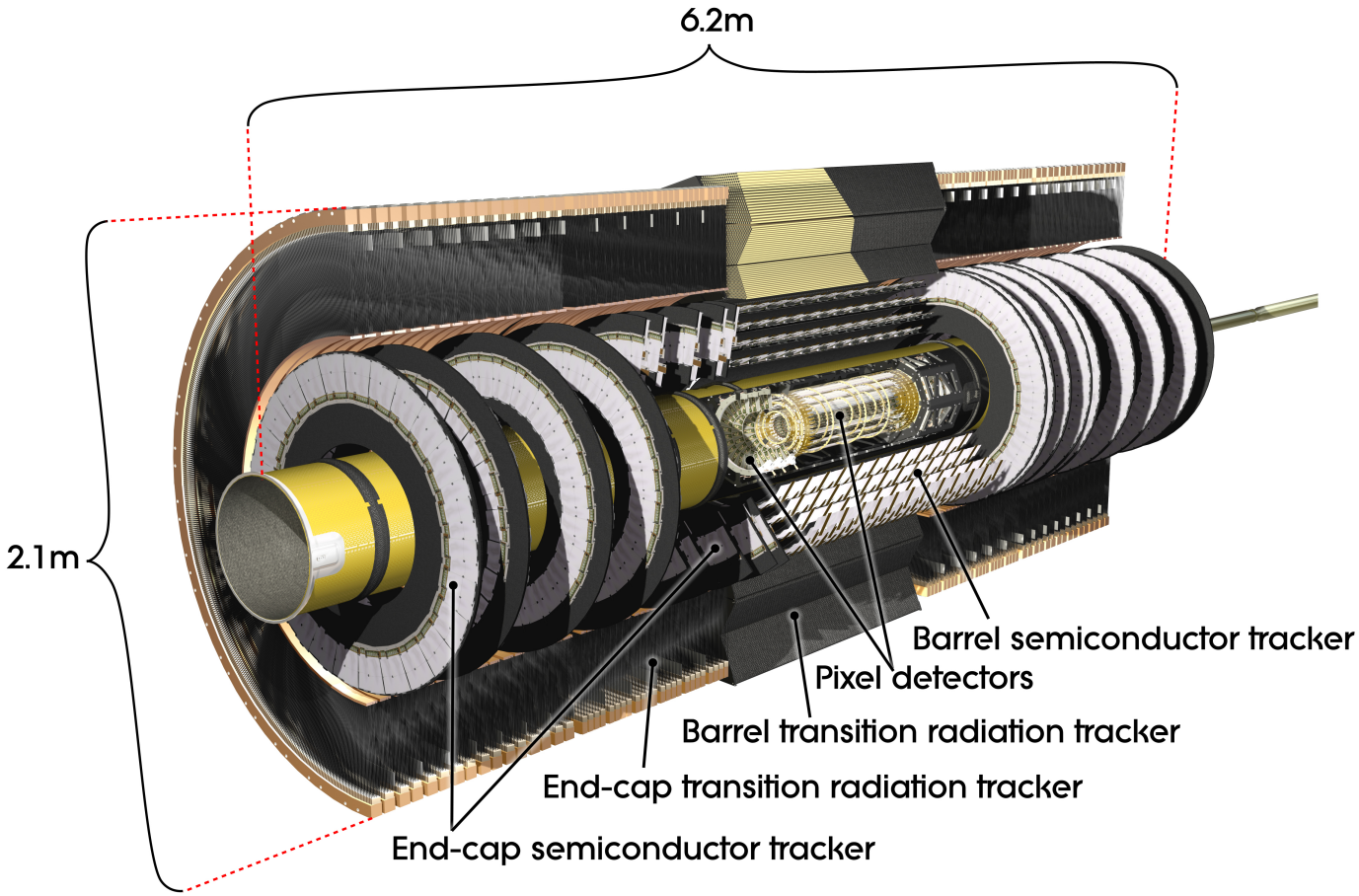

Figure 2.5: A view of the Inner Detector system at ATLAS [13] and its three components: the pixel detector, the semiconductor tracker, and the transition radiation tracker. Figure courtesy of CERN [48].

2.3 Calorimeter

In calorimetry, the goal is to determine the energy of an incoming particle. This measurement is done by absorbing the particle and measuring the energy it deposits in the material. The manner in which a particle deposits energy determines how well the calorimeter performs, and how much/what type of material is needed. Note that, unlike the inner detector, this process is *fundamentally destructive* in that it absorbs the particle. Consequently, the calorimeter must come after the tracking system. A particle interacts with the material of the calorimeter and produces more particles, which go forward through the calorimeter. The initial energy of the particle distributes over the produced lower-energy particles. When the resultant particles interact with the material, they produce more particles, all of which have less energy. This iterative process continues until the energies of the produced particles are low enough that they are absorbed via ionization. This process is called showering. This should not be confused with the *parton* showering described earlier which was in the context of jet formation.

There are two types of showering processes, depending on the underlying interactions: electromagnetic (EM) and hadronic showers. EM showers are driven by the electromagnetic processes of bremsstrahlung and pair production (for high energies), as well as ionization, Compton scattering, and the photoelectric effect (for lower energies). Hadronic showers are driven by strong and EM interactions [39]. The hadronic interactions involve $\pi^{0,\pm}$ which dominate, as well as kaons, protons, and neutrons. The charged pions undergo subsequent nuclear interactions, while the neutral pions almost instantly decay via $\pi^0 \to \gamma\gamma$, providing an EM component to hadronic showers. These two types of showers have different profiles.

The electromagnetic processes result in efficient energy absorption and have a narrow angular distribution (largely determined by multiple scattering). In hadronic showers, the energy absorption is not as efficient, and the lateral width is determined by momentum transfer in nuclear interactions. Therefore, EM showers are narrow and short, while hadronic showers are long and wide [39]. Furthermore, hadronic showers are not well measured as they have *invisible energy* - energy deposited that cannot be measured, for example, nuclear bond breaking. The difference between the development of the two types of showers is shown is figure 2.6.

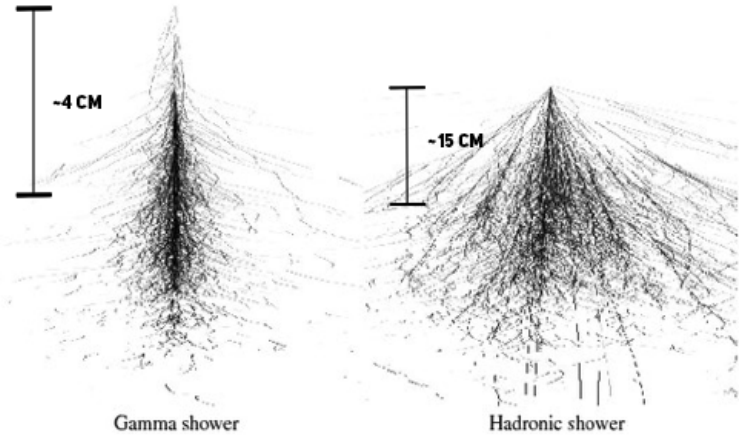

Figure 2.6: [37] The characteristic shapes of the two different types of showers. The electromagnetic case can be seen on the left, while the hadronic can be seen on the right. Electromagnetic showers are more narrow and well-contained, while hadronic showers tend to have wider and longer profiles. The scales are an estimate, added manually using the characteristic energy deposition plots of hadronic and electromagnetic showers vs interaction/radiation lengths in lead.

Additional care has to be taken when dealing with hadronic showers, as they are long. If not enough material is used, the shower survives through the calorimeter, yielding an incomplete energy measurement; this is called *punch-through*. Two parameters are defined to characterize the lengths of these interactions: the radiation length X_0 and the interaction length λ_I. The radiation length is the length over which an electromagnetic shower's energy is reduced to a factor of e of its initial value, while the interaction length is the average distance a particle will travel before initiating a nuclear interaction [39].

The ATLAS EM calorimeter is a sampling calorimeter that uses lead as the absorber, and liquid-argon (LAr) as the active material. It is divided into two parts: the barrel region $\eta < 1.475$, and the end-cap region $1.375 < \eta < 3.2$. The barrel region EM calorimeter has finer granularity than the endcap EM calorimeter, and the total radiation lengths are $24X_0$ in the barrel and 26 X_0 in the endcap [13]. The EM barrel and endcap calorimeters have an accordion geometry in order to eliminate cracks in the azimuthal direction.

The hadronic calorimeter is also a sampling calorimeter, but the material changes depending on the η region. The barrel region covers $\eta < 1.7$, for which the absorber is steel, and the active material consists of plastic scintillator tiles. The LAr hadronic end-cap calorimeter covers the region of $1.5 < \eta < 3.2$ (slight overlap with the tile calorimeter). Here the scintillating tiles are replaced with LAr to provide radiation hardness, and copper is used instead of steel as the absorber.

And third, there is the LAr forward calorimeter (FCAL), which is located in the same cryostat as the endcap. The forward calorimeter has EM and hadronic components, and covers the region $3.2 < \eta < 4.9$ [22]. The total thickness is 11 λ_I [13]. The FCAL improves the hermetic coverage of ATLAS, allowing for an improved determination of the missing transverse energy as well as the detection of forward jets. These are important as they are needed for the momentum balance in an event, but they are also crucial in studying the parton structure of the proton, and the Higgs boson production in vector-boson-fusion processes [35].

A diagram of the calorimeter systems is shown in figure 2.7, while some extra information can be found in table 2.2.

EM Calorimeter	**Barrel**	**End-cap**	
Coverage	$\|\eta\| < 1.475$	$1.375 < \|\eta\| < 3.2$	
Longitudinal Segmentation	3 samplings	3 samplings	$1.5 < \|\eta\| < 2.5$
		2 samplings	$1.375 < \|\eta\| < 1.5$
			$2.5 < \|\eta\| < 3.2$
Granularity ($\Delta\eta$x$\Delta\phi$)			
Sampling 1	0.003 x 0.1	0.025 x 0.1	$1.375 < \|\eta\| < 1.5$
		0.003 x 0.1	$1.5 < \|\eta\| < 1.8$
		0.004 x 0.1	$1.8 < \|\eta\| < 2.0$
		0.006 x 0.1	$2.0 < \|\eta\| < 2.5$
		0.1 x 0.1	$2.5 < \|\eta\| < 3.2$
Sampling 2	0.025 x 0.025	0.025 x 0.025	$1.375 < \|\eta\| < 2.5$
		0.1 x 0.1	$2.5 < \|\eta\| < 3.2$
Sampling 3	0.05 x 0.025	0.05 x 0.025	$1.5 < \|\eta\| < 2.5$
Presampler	**Barrel**	**End-cap**	
Coverage	$\|\eta\| < 1.52$	$1.5 < \|\eta\| < 1.8$	
Longitudinal Segmentation	1 sampling	1 sampling	
Granularity ($\Delta\eta$x$\Delta\phi$)	0.025 x 0.1	0.025 x 0.1	
Hadronic Tile	**Barrel**	**Extended Barrel**	
Coverage	$\|\eta\| < 1.0$	$0.8 < \|\eta\| < 1.7$	
Longitudinal Segmentation	3 samplings	3 samplings	
Granularity ($\Delta\eta$x$\Delta\phi$)			
Samplings 1 and 2	0.1 x 0.1	0.1 x 0.1	
Samplings 3	0.2 x 0.1	0.2 x 0.1	
Hadronic LAr		**End-cap**	
Coverage		$1.5 < \|\eta\| < 3.2$	
Longitudinal Segmentation		4 samplings	
Granularity ($\Delta\eta$x$\Delta\phi$)		0.1 x 0.1	$1.5 < \|\eta\| < 2.5$
		0.2 x 0.2	$2.5 < \|\eta\| < 3.2$
Forward Calorimeter		**Forward**	
Coverage		$3.1 < \|\eta\| < 4.9$	
Longitudinal Segmentation		3 samplings	
Granularity ($\Delta\eta$x$\Delta\phi$)		~0.2 x 0.2	

Table 2.2: Parameters for the calorimeter components [22].

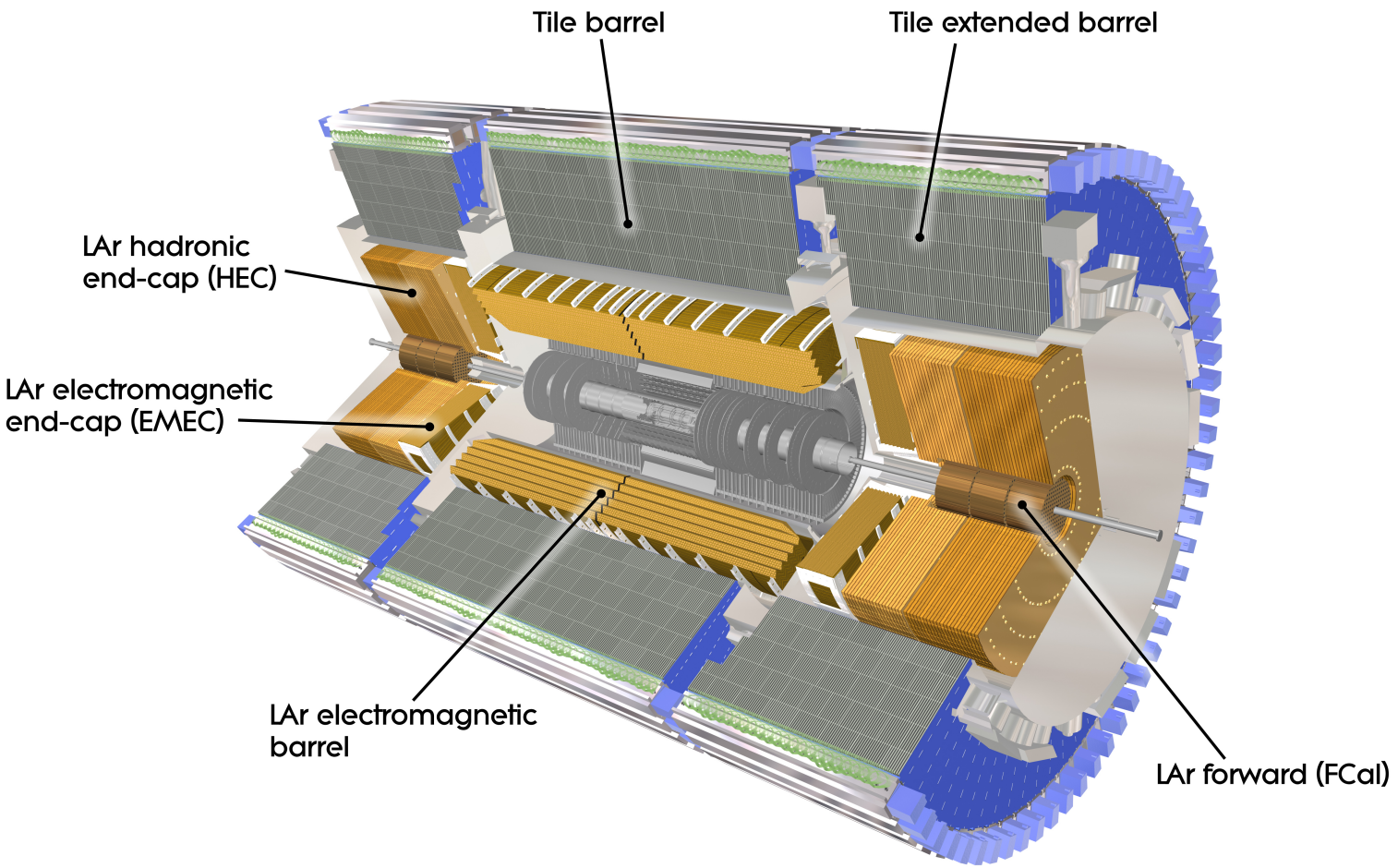

Figure 2.7: A view of the Calorimeter system at ATLAS [22]. Figure courtesy of CERN [47].

2.4 Muon Spectrometer

The calorimeter measures energies by absorbing the particles incident on it. Muons are typically not absorbed because they are Minimum Ionizing Particles (as explained earlier). They instead survive through the calorimeter system, depositing a minimum amount of energy. There is a dedicated part of ATLAS for measuring muons called the Muon Spectrometer. The basic idea is the same as the Inner Detector in that it provides the trajectory measurement of a particle moving through a magnetic field. To this end, the Muon Spectrometer has a separate magnet system. It uses a series of large superconducting air-core toroid magnets and four different tracking technologies [22, 13]. In the region $\eta < 1.4$, the barrel toroid supplies the magnetic field responsible for the bending. For the region $1.6 < \eta < 2.7$, two end-cap toroids provide the field.

Monitored Drift Tubes are used to track charged particles in the region $\eta < 2$. Drift tubes are filled with gas and a wire stretched down the center. When a charged particle passes through the gas, it ionizes it, producing electrons. These then drift to the wire (which has a positive potential), inducing a signal that is read out. A series of these tubes provides tracking hits along the trajectory of the muon [39]. For $2 < \eta < 2.7$, Cathode Strip Chambers (CSC) are used. The idea behind a Cathode Strip Chamber is the same as a drift tube, except that instead of isolated tubes, multiple wires are in a chamber filled with gas, and the strips are read out instead of the wires [39, 13].

Due to the requirement that the muon spectrometer be standalone, it must have a dedicated trigger system. The trigger system uses Resistive Plate Chambers (RPCs) in the barrel, and Thin Gap Chambers (TGCs) in the endcap [22]. RPCs provide a fast and reliable muon trigger system. They are composed of two oppositely charged parallel plates with gas filling the space between them. When a muon goes through, the gas is ionized, and the electrons drift to the readout plate, which is lined with readout strips. The TGC is a similar idea, but in this case, wires are strung between the plates. These are read out on the cathode planes via copper strips and pads. [39, 13, 52].

The muon spectrometer system is shown in figure 2.8, and some parameters for the different tracking technologies can be found in table 2.3.

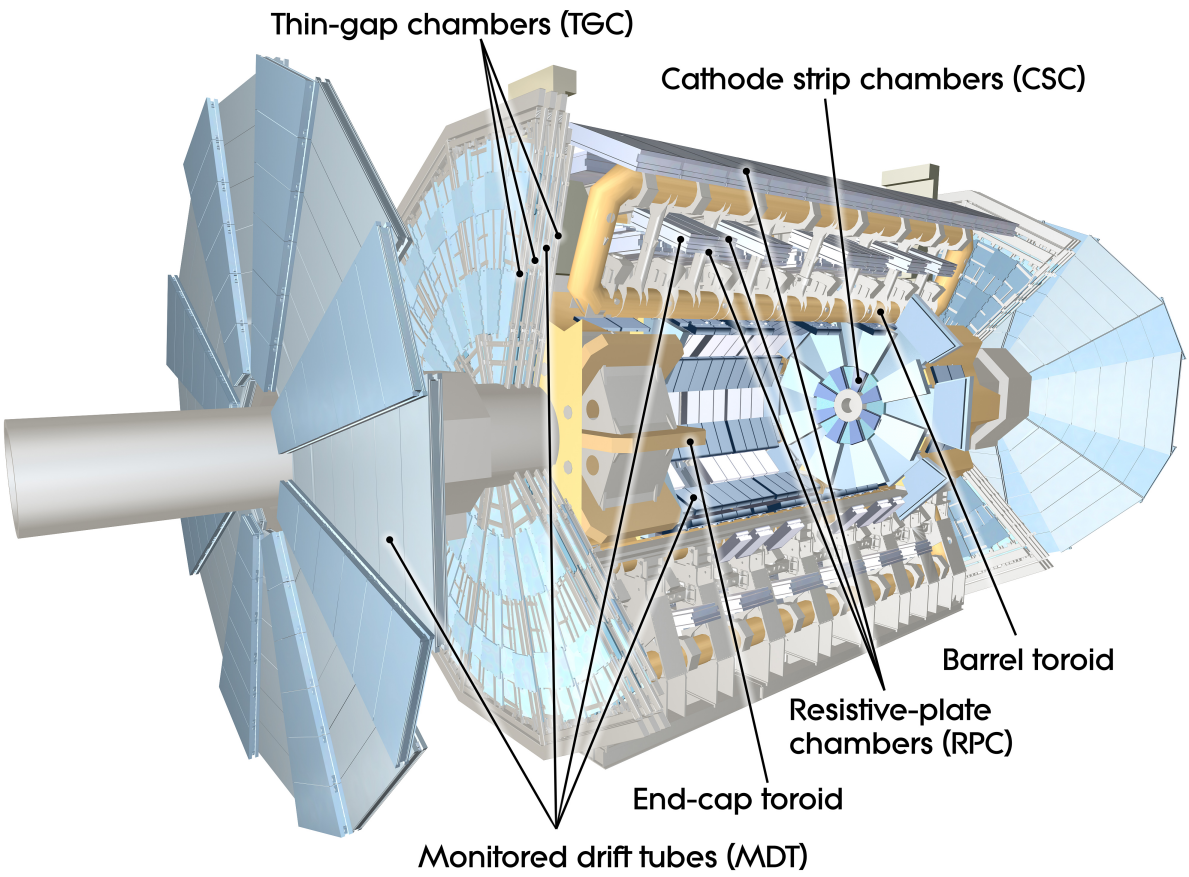

Figure 2.8: A view of the Muon Spectrometer system at ATLAS [13]. Figure courtesy of CERN [49].

Monitored Drift Tubes	**MDT**
Coverage	$\|\eta\|< 2.7$ (innermost later: $\|\eta\|< 2.0$)
Number of Chambers	1088 (1150)
Number of Channels	339,000 (354,000)
Function	Precision Tracking
Cathod Strip Chambers	**CSC**
Coverage	$2.0 < \|\eta\|< 2.7$
Number of Chambers	32
Number of Channels	31,000
Function	Precision Tracking
Resistive Plate Chambers	**RPC**
Coverage	$\|\eta\|< 1.05$
Number of Chambers	544 (606)
Number of Channels	359,000 (373,000)
Function	Triggering, Second Coordinate
Thin Gap Chambers	**TGC**
Coverage	$1.05 < \|\eta\|< 2.7$ (2.4 for triggering)
Number of Chambers	3,588
Number of Channels	318,000
Function	Triggering, Second Coodrinate

Table 2.3: Some parameters of the muon spectrometer components [13].

2.5 Trigger & DAQ

Due to the very large rate of events and the associated particles passing through the detector, an excellent trigger and data-acquisition (DAQ) system must be in place to limit the amount of data stored for further analysis. The trigger selects events that have a topology of interesting events. As the details are beyond the scope of this thesis, only a quick summary is provided here.

The ATLAS trigger system works in two stages [28]:

1. The Level-1 (L1) Trigger

   This L1 is a hardware-based trigger that uses information from the calorimeter and the muon trigger detectors to decide if events that occur are of interest. Many other subsystems are used to help with this task, such as the Minimum Bias Trigger Scintillators, the LUCID Cherenkov counter, and the Zero-Degree Calorimeter. The L1 trigger passes at most 100,000 events every second to the HLT.

2. The High-Level Trigger (HLT)

   The HLT is a software-based trigger that is made of a large CPU farm of 28,000 processors which are located behind shielding in a room near the detector. A detailed analysis of each event is executed, examining the entire event for selected technologies (tracker and calorimeter, for example), or analyzing the entire detector in isolated regions of the detector (looking at the ID, calorimeter, and MS for a specific η region). The HLT accepts around 1,000 events every second, which the DAQ then saves to disk and then computer tape.

If an event passes the L1 trigger and the HLT, it is transferred to the tier-0 site at CERN for storage and offline (post-run) analysis. The trigger has on the order of μs to make these decisions. The logic flow of the trigger and DAQ (TDAQ) system is shown in figure 2.9.

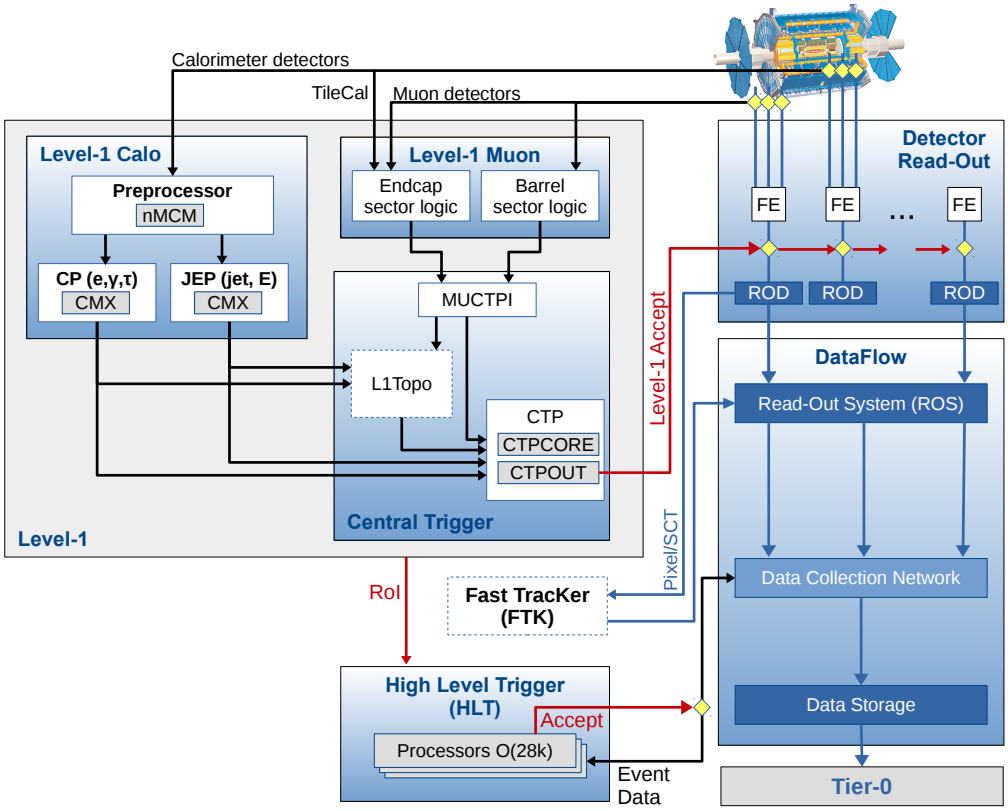

Figure 2.9: An overview of the ATLAS TDAQ system, courtesy of the ATLAS Collaboration [28]. There are two trigger subsystems: the hardware-based Level 1 (L1) trigger, and the software-based High-level trigger (HLT). The L1 trigger uses input from the calorimeter and muon systems, as well as some other subsystems. The decision formed by the L1 trigger goes into the Central Trigger Processor (CTP), which does dead-time processing. If the L1 trigger accepts the event, it is buffered in the Read-Out System (ROS) and passed into the HLT. The HLT then further analyzes the event in more detail. If the HLT decides to keep the event, it is then stored at the Tier-0 facility at CERN.

2.6 Data Preparation

The data are stored at the Tier-0 facility at CERN. A copy of the data is sent to eleven Tier-1 sites around the world to safeguard the data and for further refinement and analysis. The ATLAS Tier-1 sites are located in Canada (SFU/TRIUMF), Germany (FZK), Spain (PIC), France (IN2P3), Italy (CNAF), The Netherlands (SARA), Russia (JINR), Taiwan (ASGC), Nordugrid (Scandinavia), UK (Rutherford Appleton Laboratory), and the US (Brookhaven National Laboratory). There is then a calibration pass in which the detector readings are parsed. The data are then refined into Event Summary Data (ESD) files, which contain reconstructed information (such as data needed for particle ID or track reconstruction) sufficient for tuning algorithms/calibrations. Then, the ESDs are further refined into a dataset that contains all the key information needed for analyses. This data format is called an xAOD (Analysis Object Data), wherein the data are comprised of physics objects (reconstructed particles and jets). These xAODs are stored at 155 [1] Tier-2 sites around the world, which are comprised of universities and other scientific laboratories. After the xAOD stage, further refinement is performed by applying conditions to filter out specific subsets of events. These are called DxAODs (Derived xAODs). For the results presented here, the JETM3 DxAOD collection is used, which has a preliminary selection applied to filter for $Z \to ee/\mu\mu$ events. The DxAODs have multiple jet collections formed with different reconstruction algorithms (PFlow and EMTopo, described in chapter 3.1), as well as refined particle ID and track reconstruction. These are also stored at Tier-2 sites globally. Tier-3 sites correspond to university/institute clusters and storage facilities. The Grid is an interconnected system of computer centres spanning the globe, where users can access all the Tier-2 data and run analyses on them using resources associated with the servers. Most large-scale analysis is done on the Grid, including the production of all the results presented here.

Monte-Carlo (MC) simulated datasets are used to assess the performance of the triggers [28], to derive a Jet Energy Scale (MCJES) that provides a preliminary correction to the energy of the jets, and have many uses in analyses (such as background estimation). There are two main steps to event simulation:

1. Generate the collision (generator step). This step covers everything from the interaction up to the end of the hadronization process.

2. Propagate the particles through the detector (detector step). This step requires a detailed knowledge of the detector and has to incorporate every possible type of interaction that particles may experience in a material. The product is a pseudo-dataset, and so the readout of the detector must be simulated as well.

For the detector step, a framework called GEANT4 is used [31, 12]. For the generator step, there are many different algorithms used to describe the collision dynamics, as well as the parton showering and the formation of the jet particles (hadronization process). The two generators used in this analysis are called Sherpa [38] and Pythia [56]. Pythia is used as the nominal generator, while Sherpa is the alternate generator that is the most different from Pythia. The difference between the two generators largely comes from the hadronization (recall that the hadronization step of the fragmentation process cannot be treated perturbatively and so must be modelled). Pythia is chosen as the nominal generator by ATLAS. By comparing results from the two most different generators and using the ratio of responses as an uncertainty, all possible choices of generators in physics analyses are covered.

For the nominal MC dataset, the generator used is Powheg+Pythia8 [56], with the AZNLO underlying-event parameter set [9], and the CTEQ6L1 PDF set [45]. The alternate MC dataset uses the Sherpa-2.1.1 generator [38] and the default Sherpa underlying-event tune, alongside the NNPDF-3.0 NNLO PDF set [15].

Chapter 3

Jet Physics

3.1 Jet Reconstruction

Jets are reconstructed using readings from detector systems in an event. The ATLAS calorimeter system is comprised of many small segments that are called calorimeter cells. However, particles generally deposit energy in multiple cells, so the first step in jet reconstruction is to group cells into clusters. ATLAS uses an algorithm called the 4-2-0 clustering algorithm [29]. A visual representation of this process is shown in figure 3.1.

The difference between the energy deposited in a cell and the expected background noise is calculated, and then divided by said width (sigma) in order to determine the significance of the energy deposition. Any cell that exceeds the background by more than 4σ is deemed significant enough to warrant a cluster and is used as a seed. If any of the neighboring cells have a significance greater than 2σ, they are added to the cluster. Then, the immediate neighbors of these cells are also examined. If any of these have a significance larger than 2σ, they are also included. This iterative inclusion of 2σ neighbors continues until there are no remaining 2σ neighboring cells. A ring having a thickness of one cell is then included around the entire cluster, regardless of the significance (0σ), in order to include the tails of the deposited energy (which improves resolution). This comparison of neighbors is done in 3D, and also extends to cells that are in deeper layers. The end result is a three-dimensional collection of cells based on the significance values detailed above. These values were optimized for energy resolution, and the method is reported as $\sigma_{seed} - \sigma_{neighbour} - \sigma_{edge}$ [29]. Thus, the ATLAS clustering algorithm is called the 4-2-0 algorithm.

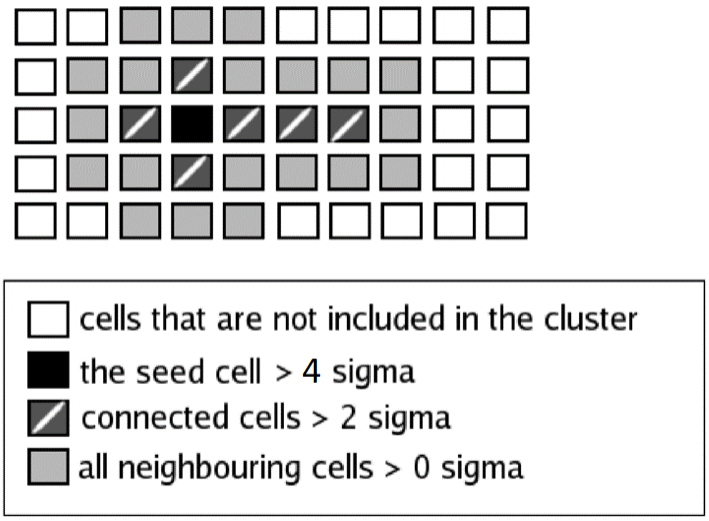

Figure 3.1: A cell that has energy that exceeds the background by more than 4σ is used as the seed for a cluster. Then, any neighbors that exceed 2σ are included in the cluster as well. This significance check proceeds until there are no more neighbors that exceed 2σ. Then, in order to include the tails/edges of the cluster, all remaining neighbors are also included, regardless of significance (0σ). All neighbor checks and inclusions are done in 3D. This process constitutes the 4-2-0 clustering algorithm. [54, 55].

If the energy of the clusters is not modified, they are said to be at the EMTopo scale. This is because the calorimeter is calibrated for electromagnetic showers. An alternative is the Local Calibration (LC) scale [16], which attempts to compensate for the energy loss in hadronic showers. However, it is no longer officially supported by ATLAS. The LC scale looks at the density of energy in a cluster, and scales the energy up accordingly. For electromagnetic-like energy deposits, the clusters are left untouched. But for hadronic-like deposits (low energy density), the cell energies are scaled up. This scale is used because, for hadronic interactions, the primary energy loss is from nuclear interactions in the calorimeter, and the energy lost to bond-breaking cannot be detected. This results in a lower response [39]. By looking at the energy density and neighboring cells, one can determine an energy scale-factor that compensates for these effects. However, this scale is mostly obsolete, as an algorithm for calibrating jets called the Global Sequential Calibration (GSC) has provided similar improvements to the energy resolution with a more general approach. The LC scale is not used in ATLAS recommendations or this thesis but may be present in some references or other research presentations.

Clusters can be grouped to form jets. Once can also combine tracking information with clusters to form a collection of jets known as PFlow jets (detailed later). In simulation, the real information of particles is saved as truth particles. These truth particles can be

grouped to form truth jets. All of these jet collections are formed with a common jet reconstruction algorithm, which must meet a certain set of criteria [16]:

1. Infrared Safety: the algorithm should be insensitive to soft (low energy) radiation in the event. If there is soft radiation present, it may provide a bridge for a jet reconstruction algorithm to cross from one jet to another, resulting in an oversized jet that is incorrect. An illustration of this is shown in figure 3.2.

2. Collinear Radiation Insensitivity: the algorithm should reconstruct the same jet, regardless of the presence of collinear radiation. There are two possible ways that collinear radiation may affect jet reconstruction. If a high energy particle emits boosted radiation, the initial energy is divided between two particles that are traveling very nearly in the same direction. These particles should still be a seed for a jet, but the energy splitting may lower the individual particle energies to the point where the algorithm does not recognize them as being significant enough to warrant a jet. This is illustrated in figure 3.3. Secondly, if a high-energy particle emits collinear radiation, the jet center may be skewed away from this particle by weighting effects. This is shown in figure 3.4. The chosen reconstruction algorithm must be immune to both these effects.

3. Invariance Under Boosts: the algorithm should be able to find the same jets regardless of any Lorentz Boost effects.

4. Boundary Stability: the kinematic variables that the algorithm determines for the jet must be insensitive to the specific details of the final state (such as the number and angle of particles).

5. Order Independence: the same jet should be reconstructed at particle level (jets reconstructed with particles before the interaction with the detector, also known as truth jets in MC) and at calorimeter level (jets reconstructed using detector information).

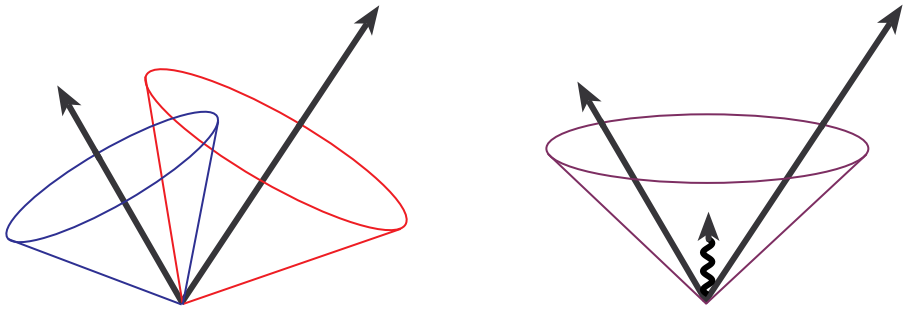

Figure 3.2: [16]. The presence of soft radiation could provide a bridge for jet reconstruction algorithms to group two distinct jets into one large jet. The ideal reconstruction algorithm would be insensitive to such effects.

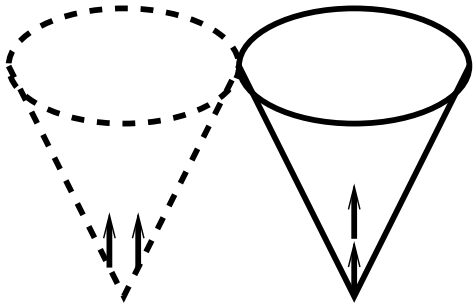

Figure 3.3: [16]. If the seed energy is split between two cells, a jet reconstruction algorithm may miss this jet due to low energy, although it would have been reconstructed if the energy was deposited in one cell. This is called collinear sensitivity, and an ideal jet reconstruction algorithm must reconstruct the same jet in both cases.

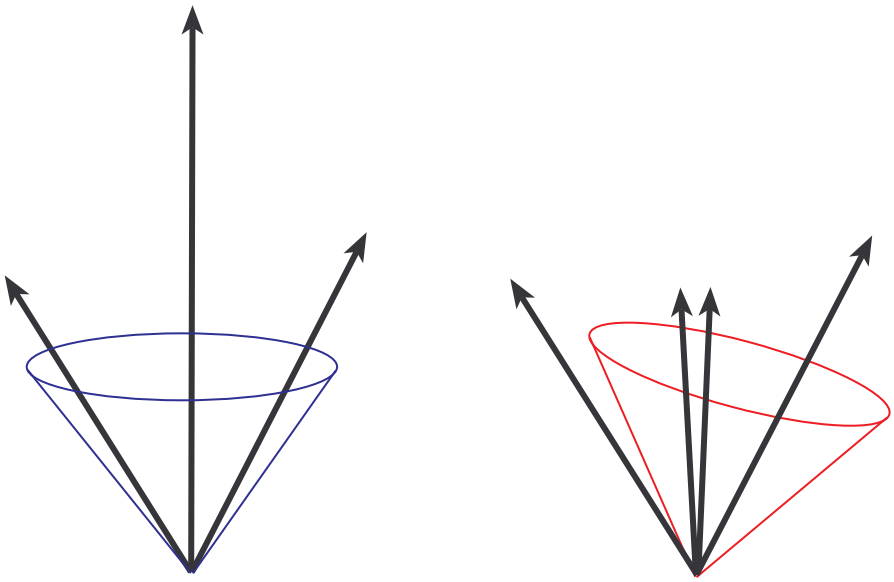

Figure 3.4: [16]. If the seed energy is split between two cells, a jet reconstruction algorithm may skew the jet towards one side, which is clearly incorrect. This effect of collinear radiation must not affect an ideal jet reconstruction algorithm. In this illustrated case, the skewing of the jet axis results in the exclusion of a particle that should be part of the jet as well.

One such family of jet-finding algorithms is the sequential recombination algorithms (also known as the k_t algorithms)[41, 16, 21]. They are defined using the quantities

$$d_{ij} = \min(p_{T,i}^{2n}, p_{T,j}^{2n}) \times \frac{\Delta_{i,j}^2}{R^2} \tag{3.1}$$

where

$$\Delta_{i,j} = \sqrt{(\phi_i - \phi_j)^2 + (y_i - y_j)^2} \tag{3.2}$$

$$d_{iB} = k_{t,i}^{2n} \tag{3.3}$$

The indices i, j represent objects in a running list of *proto-jets*, for example the list of clusters found in the previous step of the jet reconstruction. Proto-jets are candidate jets, which can be combined if they satisfy certain criteria. The other variables are the transverse momentum ($p_{T,i}$), azimuthal angle (ϕ_i), and the rapidity (y) of the particles. Here, R is a tunable parameter that determines the size of the jet in $y - \phi$ space.

The steps of the recursive k_t algorithm are [16, 21]:

1. A list of proto-jets is constructed that consists of all individual particles and partially combined jets from the previous iteration. It has a list of four-vectors for each proto-jet.
2. The parameter d_{ij} is calculated for every pair of proto-jets.
3. The distance parameter d_{iB} is calculated between every proto-jet and the beam pipe.
4. For a given proto-jet, if d_{iB} is smaller than all other d_{ij}, that proto-jet is promoted to a full jet. Otherwise, the proto-jet pair with the smallest d_{ij} is combined.
    - There are various ways of combining jets (such as p_t weighting), but ATLAS simply adds the four-vectors of the proto-jets [20].
    - After this step, the algorithm returns to step 1, and the process continues until all proto-jets have been combined into jets.

The behaviour and properties of the algorithm are determined by the parameter n, which can be set to: $n = -1, 0, 1$ [16, 21]. The corresponding algorithms are called:

- $n = 0$, Cambridge-Aachen algorithm: this is simply a geometrical clustering in $y - \phi$ space because the first term in d_{ij} is 1. It is the most intuitive of the methods and is used at ATLAS for grooming large radius jets (not relevant here).
- $n = 1$, k_t algorithm: the first term of the d_{ij} calculation favours small p_t, so that this algorithm starts by combining low-p_t proto-jets. The k_t algorithm has runaway boundary problems as the low-momentum particles can allow for bridges between multiple collections of proto-jets resulting in large non-uniform jets. The k_t algorithm is useful for studying jet substructure, but is not used as the main jet-finding algorithm at ATLAS.
- $n = -1$, anti-k_t algorithm: the first term of the d_{ij} calculation favours large p_t, so that this algorithm starts by combining high-p_t proto-jets. The idea is to construct

jets around large momentum seeds, which results in clearly defined cone-shaped jets if they are isolated. For overlapping jets, if $p_{t,jet1} >> p_{t,jet2}$ the overlapping particles will be attributed to the first jet (which will be a perfect cone), and the second jet will have a crescent shape. For equal momentum jets, the overlap area is divided between the jets by a straight line. For the general case where $p_{t,jet1} \approxeq p_{t,jet2}$, the overlap area is split using p_t weighting [21].

ATLAS uses the anti-k_t algorithm for its jet reconstruction because it meets the set of criteria outlined above, and gives jets that are centered on large energy depositions. The different jet-clustering methods and their results are shown in figure 3.5.

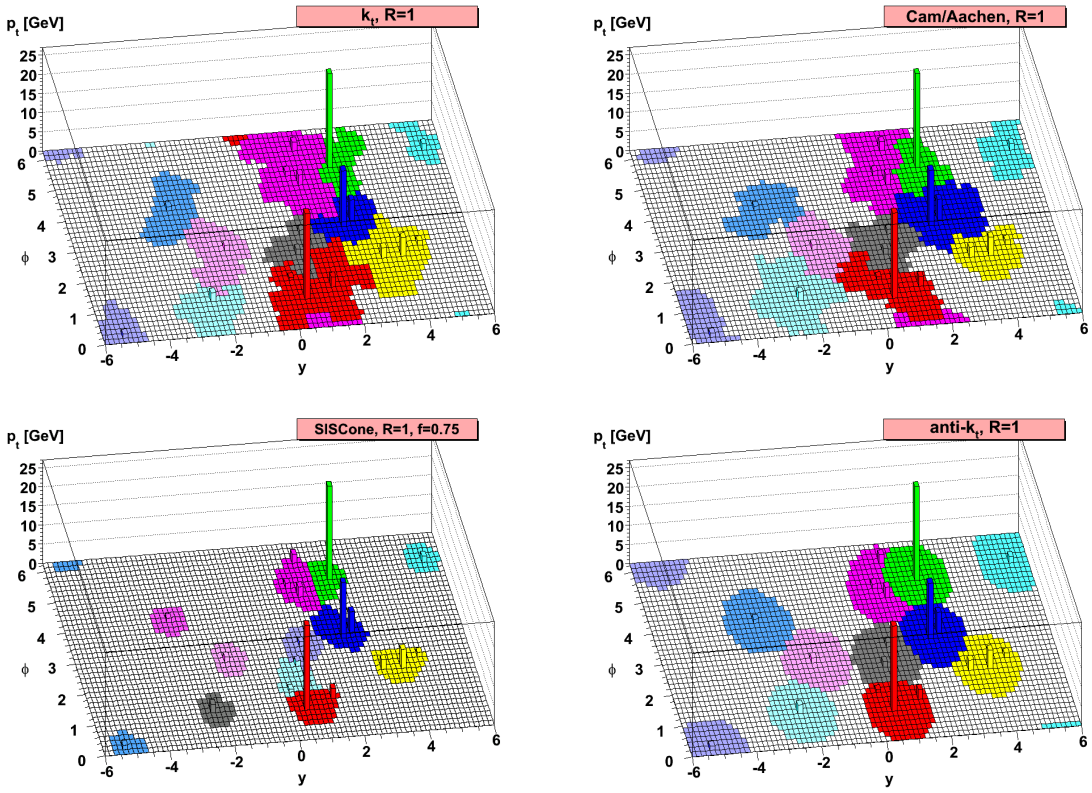

Figure 3.5: [21]. A characteristic MC event is shown. The performance of the different jet-clustering methods can be seen, where it is evident that the anti-k_t algorithm provides the most stable jet shapes. The SIScone algorithm is seedless, and begins by forming stable cones and then doing overlap merging/splitting between cones [19, 59]. It is not used at ATLAS.

In the JETM3 DxAOD collection, the jets are reconstructed with the anti-k_t algorithm with a handful of different R values (which roughly correspond with the maximum radii of the jets), and with different scales for the clusters (such as EMTopo or LC). Setting $R = 0.4$ results in the *small-R* jet collection, while $R = 1.0$ results in the *large-R* jets. While small-R jets are commonly used at ATLAS for analyses, large-R jets are used to study highly boosted topologies; for example, a boosted W boson and its decay products can be contained in a large-R jet.

Besides EMTopo and LC jets, there is a third collection called EMPFlow (PFlow for short) jets [27]. PFlow jets are formed using both tracking information and the calorimeter clusters (as opposed to only clusters). The idea here is that by combining two different measurements of the energy/momentum, a better energy resolution is achieved because the tracker measures low momentum particles better than the calorimeter. All tracks in the event are considered and are extrapolated through the calorimeter and the muon spectrometer. The extrapolated tracks are matched with clusters. In this way, each charged particle has an associated track, and a resultant jet has a set of tracks matched to it. At low-p_t, the calorimeter energy response is low (detailed later). In this regime, the measurement of the track curvature is more accurate.

At larger p_t, the calorimeter energy response is higher, but the track radius measurement is less accurate because the deflection in the magnetic field is smaller. Therefore, at low-p_t, one can expect a better measure of the energy of the jet using tracks instead of calorimeter clusters, and at high-p_t the converse is true. This scheme is reliable and gives improved energy resolution. It is now the default jet collection at ATLAS.

The PFlow algorithm proceeds as follows [27]:

1. Tracks are selected with tight restrictions (at least nine hits in the silicon detectors, no missing pixel hits, tracks within $|\eta| < 2.5$, $p_t^{track} > 0.5$ GeV, and which are not matched to medium-quality electrons or muons).

2. The selected tracks are then matched to *single* topo-clusters.

3. The energy in the topo-clusters (E) is compared to the expected energy (track momentum p), and an E/p value is calculated.

4. The probability that energy was deposited in multiple topo-clusters is calculated (the discriminant is the significance of the difference between the cluster energy and the expected energy).

5. If it is determined that the shower in the calorimeter was split over different topo-clusters, all topo-clusters within a cone of $\Delta R = 0.2$ around the track are considered matched to the track.

6. The expected energy deposition in the calorimeter is subtracted cell-by-cell from the topo-clusters to avoid double-counting the energy.

7. If the energy in the remaining cells is less than $1.5 \times \sigma(E_{expected})$ (if it is consistent with the width of the E/p curve), the remnant cell energy is attributed to shower fluctuations, and is removed from the topo-clusters.

   If the remnant cell energy is greater than this threshold, it is not removed as it may originate from a different particle.

8. The output of the algorithm is the collection of tracks and their associated energy-subtracted topo-clusters, as well as any unmatched clusters that remain unchanged.

For the research presented here, $R = 0.4$ anti-k_t jets are analyzed for EMTopo and PFlow inputs to the reconstruction algorithm.

3.2 Jet Calibration Chain

Once jets are reconstructed, they undergo a series of energy calibration steps. The calibration chain is shown in figure 3.6.

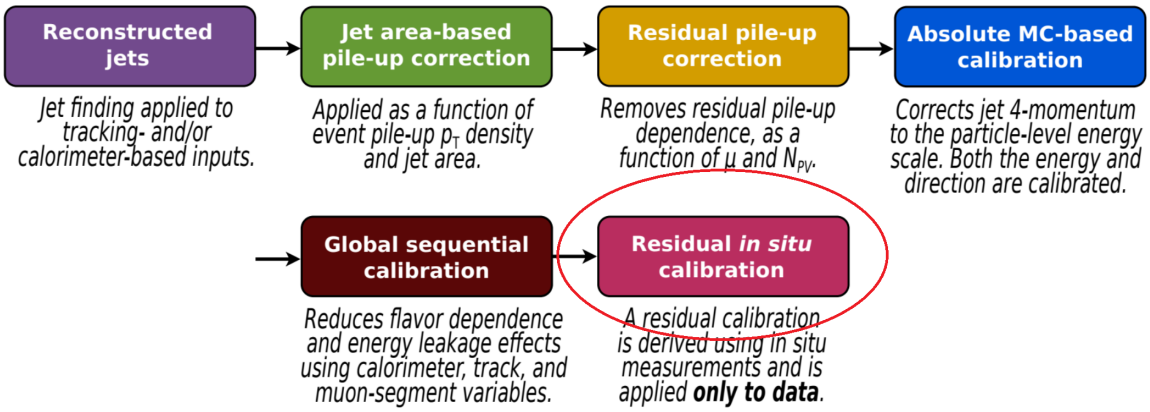

Figure 3.6: The calibration chain that is applied to small radius jets [41]. It is discussed in detail below. At the end of the chain is the Residual *in-situ* calibration (circled in red), which is the topic of this thesis.

Before the calibration chain is discussed, *pile-up* must be defined. Pile-up is the presence of excess energy in the event due to additional proton-proton collisions that occur simultaneously with the collision of interest. If there are extra interactions within the same bunch crossing, they lead to energy depositions in the calorimeter that overlap with the primary interaction. This pile-up is called in-time pile-up. It can be characterized by the number of primary vertices (N_{PV}) present in the event. The proton-proton collisions in nearby bunch crossings contribute energy to the current event, which is called out-of-time pile-up and can be characterized by the average number of interactions per bunch crossing (μ), since the number of collisions (i.e. vertices) is not measured for adjacent bunch crossings. The calorimeter is affected by this due to its long measurement time, while the tracking detectors are relatively unaffected (fast semiconductor sensor measurement which requires one process: the production of an electron-hole pair). It is impossible to determine if pile-up is in-time or out-of-time, so these two parameters are used together to characterise pile-up behaviour.

The steps in the calibration chain are shown in figure 3.6, and are as follows:

1. Reconstructed jets: this is the jet reconstruction described in the previous section. Clusters of calorimeter cells are formed using the 4-2-0 algorithm, and jets are constructed using the $R = 0.4$ anti-k_t algorithm. The inputs to the reconstruction algorithm are EMTopo calorimeter clusters and the PFlow collection.

2. Jet-area based pile-up correction [26, 23]: the jet has energy deposited by the particles that originated from the hard scatter, as well as in-time and out-of-time pile-up. To correct for the pile-up energy, the quantity $\rho \times A_{jet}$ is subtracted from the jet. Assuming that pile-up is uniformly distributed throughout the event, one can calculate the pile-up energy density ρ for each event by looking at sections of the detector that are not associated with any physics objects. The area of the jet is determined by *ghost particles* [32]. These are artificial particles that are added to the event offline. They have no mass and have extremely low momentum (magnitude of eV compared to the typical GeV scale particle energies) so that they do not affect the energy of the jet. The ghost particles are uniformly distributed in η-ϕ, so calculating the area of a jet is as simple as counting the number of ghost particles that are reconstructed in the jet. The pile-up energy density is derived by looking at low-occupancy areas of ATLAS in an event, while the area is determined on a per-jet basis.

3. Residual pile-up correction [23, 26]: the jet-area based pile-up correction is imperfect (because the energy density estimate does not describe forward regions of the detector or the high-density jet cores well), so there is a residual pile-up dependency. This can be seen when the jet energy is plotted as a function of N_{PV} or μ. In order to correct this, each distribution is flattened by the subtraction of residuals. This step is derived from an MC simulation, but is not perfect, as will be seen later.

4. Absolute EtaJES [23, 26]: this is the main calibration and is based on MC simulations. It corrects the average measured jet energy to the particle level as a function of energy and η. It accounts for the non-compensating calorimeter response, energy losses in dead material, and biases in the jet η reconstruction. It is derived using the Pythia generator with the previous steps of the chain applied, and is checked by the response of the calorimeter to single particles. These corrections assume that the MC perfectly describes data.

5. Global Sequential Calibration (GSC) [26, 33]: the GSC improves the energy resolution and reduces the flavor dependence of jets. It is comprised of many smaller MC based calibrations. It should ideally flatten dependencies on: the energy in the first layer of the Hadronic Calorimeter and the third layer of the Electromagnetic Calorimeter, the number of charged tracks in the jet, the width of the distribution of tracks, and the number of track segments behind the jets in the muon spectrometer.

6. Residual In-Situ Calibration: this is a relative calibration that uses in-situ (in data) measurements to correct the energy response of jets calculated in MC (step 4) to the actual response of the calorimeter in data. The ratio between data and MC response curves is used as a scaling factor, which is applied to jets in data.

The Residual In-Situ Calibration is critical because it normalizes the response determined in MC to the actual response in data. This crucial step is the focus of this thesis.

3.3 In-Situ Calibration

3.3.1 MPF Theory

The energy response was previously defined as

$$R = \frac{E_{measured}}{E_{truth}} \tag{3.4}$$

$E_{measured}$ is the energy read out by the detector, so a critical step in the calibration is determining the true energy of the jet. This information is provided in simulations, but it is not available in data. E_{truth} can be estimated by a well-measured reference object in an event topology that has a jet and the reference object produced back-to-back in ϕ (more details in section 3.3.3). This is predicated on the transverse momentum balance at the parton level (see figures 3.7 and 3.8). One such technique is the Missing E_T Projection Fraction (MPF) method. It was first used at CDF for the η inter-calibration [11], and at D0 to derive a data-based jet energy scale [42]. This section will begin by describing an alternate method called Direct Balance (DB), before moving to the MPF.

The initial transverse momentum of the partons in the collision is small (on the order of MeV compared to the typical GeV scales of the final state), and can be treated as 0 (on average). Thus, if there is a system in which a single reference object is back-to-back in ϕ with a jet, the reference object's p_t should balance the full recoil p_t. However, the recoil being discussed here includes all particles originating from the parton collision not associated with the reference object. In practice, the jets available for analysis are reconstructed using the detector with the anti-k_t algorithm and have a maximum radius of 0.4. Therefore, many particles that originated from the collision are not included in the jet, while extra pile-up particles and contributions from the underlying event are. The underlying event refers to the interactions of the proton remnants after a collision. These are colored and will undergo their own fragmentation process, as well as affect the fragmentation process of the jet through color reconnection. The measured jet is referred to as a *calorimeter jet* or a calo-jet. The jet reconstruction algorithm can also be applied to the particles before they propagate through the detector. Doing so yields the *particle-level jet* or *particle-jets*, which also do not include the full recoil. The goal of the JES calibration is to take the calo-jet back to the particle-level jet scale. The particle-level jet is the natural point of comparison to theory, as it is independent of the detector. So, the response is simply

$$R = \frac{p_t^{calo\ jet}}{p_t^{particle\ jet}} \tag{3.5}$$

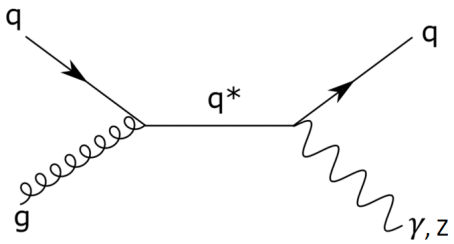

Figure 3.7: The s-channel Feynman diagram. The quark is excited via a gluon, and emits a γ/Z (either can be produced). This results in a quark jet back-to-back in ϕ with a reference object.

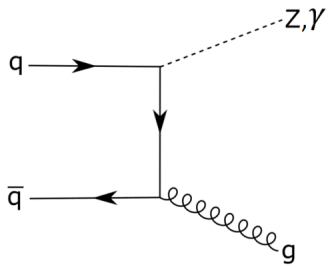

Figure 3.8: The t-channel Feynman diagram. The $q\bar{q}$ interact, resulting in the emission of a γ/Z (either can be produced) and a gluon. This results in a gluon jet back-to-back in ϕ with a reference object.

In data, the particle level information is not available. One can use p_t^{ref} as an estimate of the particle-jet momentum, but this is incorrect for the reasons discussed earlier; the particle-jet does not include all particles originating from the collision. A correction is needed to compensate for the missing and extra particles present in the particle-jet. This is called the *out-of-cone* (OOC) correction. Since the OOC correction compensates for the differences between the particle-jet and the recoil, applying it to the reference object's momentum allows for a transformation to the particle-jet momentum. This method is called the Direct Balance (DB), and the response is given by

$$R = \frac{p_t^{calojet}}{p_t^{ref} \cdot OOC} \tag{3.6}$$

The OOC correction can be quite significant (on the order of 5-10 %), and the method has shown dependence on pile-up conditions, making it potentially unstable.

The full recoiling system completely balances the reference object. This statement is true by definition, and the MPF is based on it. This is also the limitation of the MPF; it calculates the recoil response, not the jet response. The difference in response between the high-energy core of the jet and the lower-energy outer regions will affect the measured response, and necessitates corrections. These corrections need to account for particles crossing the boundary of the jets, showering of particles in the calorimeter that lead to energy depositions outside of the jet, energy contributions from the underlying event and pile-up, and gluon radiation from the parton showering. The showering correction accounts for the first two effects, and the topology correction accounts for the latter two. The combined correction was shown in the past to be of order 2 % [41], and is not derived here.

The derivation of the MPF response equation begins with the balance between the reference object and the recoil.

$$\vec{p_t}^{ref} + \vec{p_t}^{recoil} = 0 \tag{3.7}$$

The recoil here refers to every particle being produced from the quark/gluon (see figures 3.7 and 3.8 for Feynman diagrams). One can assume that the masses of the particles are small compared to the momenta involved so that $\vec{p} \approx E\hat{p}$. The previous equation can be written at calorimeter level as

$$R_{ref}\vec{E_T}^{ref} + R_{recoil}\vec{E_T}^{recoil} = -\vec{E_T}^{miss} \tag{3.8}$$

where R_{ref} and R_{recoil} are the responses of the detector to the reference object and the recoil respectively. The missing transverse energy originates from the fact that $R_{ref} \neq R_{recoil}$, which results in an imbalance in energy. It is assumed that the reference object is perfectly

measured so that its response is 1 because the calorimeter is calibrated to $\gamma/e^{\pm}$, and muons are well-measured in the Muon Spectrometer.

Projecting the equation along the direction of the reference object, and using $\vec{p_t}^{ref} + \vec{p_t}^{recoil} = 0$, the previous equation is written as

$$E_T^{ref} - R_{recoil} E_T^{ref} = -\vec{E_T}^{miss} \cdot \hat{p_t}^{ref} \tag{3.9}$$

Rearranging for the recoil response yields the MPF equation:

$$R_{recoil} = 1 + \frac{\vec{E_T}^{miss} \cdot \hat{p_t}^{ref}}{E_T^{ref}} \tag{3.10}$$

Note that this *is not* the response of the defined jet, but rather the response of the recoil system. The hadronic recoil includes particles radiated by the partons participating in the hard scattering (the jet also includes most, but not all, of these particles). Contributions from the underlying event and pile-up are superimposed on top of this, and are picked up when calculating the MPF response in an event. However, pile-up effects average to zero over a large number of events, and the underlying event is mostly ϕ-symmetric and cancels as well. These cancellations end up being a strength of the MPF, as the method is relatively unaffected by pile-up and UE effects. The combined showering and topology corrections (as detailed earlier) transform the recoil response to the desired jet response. The small uncertainty associated with the showering and topology correction as well as the significant pile-up dependence seen in DB motivate the use of MPF as the primary in-situ calibration method for small-R jets.

The MET (missing transverse energy) can be written as

$$\vec{E_T}^{miss} = -(\vec{E_T}^{ref} + \sum_n \vec{E_T}^{n}) \tag{3.11}$$

where n runs over all energy depositions in the calorimeter that are not related to the reference object. Substituting this expression back into the MPF equation yields

$$R_{recoil} = -\frac{\sum_n \vec{E_T}^{n} \cdot \hat{p_t}^{ref}}{E_T^{ref}} \tag{3.12}$$

This form shows more clearly that the recoiling system is being balanced against the reference object. However, with the inclusion of all particles in the event, the method opens itself to the response being affected by particles from the UE and pile-up. Looking at one particular event, the pile-up should balance to 0, but contributions from the UE must affect the balance and, therefore, the response calculation. Extra particles are introduced that were not part of the interaction of interest, and the event is potentially not balanced. On

average, the contributions skewing the balance in one direction are balanced out by another event where the balance is shifted in the opposite direction, and on average over a large number of events the UE effects cancel.

This on-average cancellation is robust to the point where the MPF method is essentially unaffected, making it an excellent calibration technique for ATLAS. In contrast, Direct Balance has pile-up included in the jet cone. This pile-up is always biased in the direction of the jet. A pile-up correction can be (and is) made to account for this effect, but the accuracy to which it can be done is less than the natural cancellation of pile-up effects that happens in MPF, which makes MPF a more robust technique against pile-up. DB also suffers from an added uncertainty coming from the out-of-cone correction, which has been shown to be larger than the showering and topology correction uncertainty.

3.3.2 Expected Outcome

It is instructive to anticipate the shape of the response curve as a function of jet p_t. As the particles in the jet arrive at the calorimeter, they interact and begin showering in the calorimeter material. Interactions produce more particles, which propagate and undergo subsequent collisions. This process continues until the product particles have low enough energy to be absorbed via ionization. During this showering process, there are two classes of interactions: electromagnetic and hadronic. Electromagnetic interactions produce well-measured energy depositions and yield a high response. Hadronic interactions proceed via nuclear collisions, which result in invisible energy due mostly to nuclear binding energy and neutrino production, yielding a relatively low response.

The characteristic shape of the jet energy response curve - as a function of the energy (or transverse momentum) of the jet - is due to the hadronic interactions of the π mesons because they dominate particle production in the nuclear interactions of the hadronic shower. Due to isospin symmetry, $\pi^{0,\pm}$ are produced in equal amounts. The charged $\pi^{\pm}$ predominantly deposit their energy through subsequent nuclear interactions, resulting in a poor response due to the aforementioned invisible energy [60]. The neutral π^0 decays almost immediately to two photons via $\pi^0 \to \gamma\gamma$, which then deposit their energy electromagnetically and have a high response. At each interaction point in the shower, there is an equal chance to create $\pi^{0,\pm}$. The higher the initial momentum, the more steps there are in the calorimeter shower, leading to more chances to create π^0s, which causes an increase in the overall response. At each step, there is always a 1/3 chance to create a π^0, but the number of opportunities increases. However, the increased number of steps means more nuclear interactions, which lowers the overall energy response. These two effects compete. The $\pi^0 \to \gamma\gamma$ outweighs the negative effects of the charged pions; the response increases with momentum. The presence of nuclear interactions means that the response is never 1, but a plateau is expected. The predicted response curve is shown in figure 3.9.

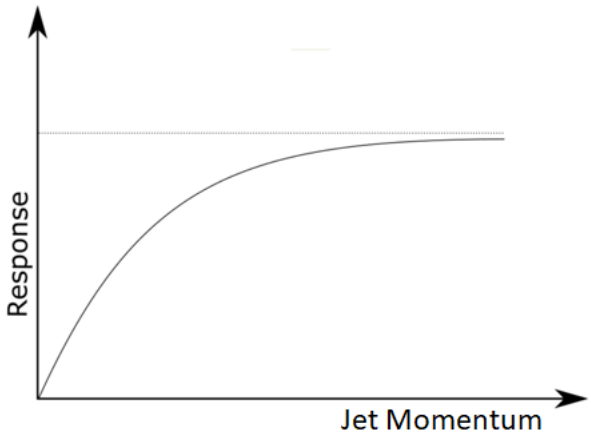

Figure 3.9: The expected response shape. At low energies, there are fewer chances to create π^0s due to less steps in the showering process before the resultant particles are absorbed. With higher initial momentum, there are more chances to do so. The charged $\pi^{\pm}$ deposit their energy hadronically so that the response is relatively low. The π^0 decays via $\pi^0 \rightarrow \gamma\gamma$, which deposit their energy electromagnetically, resulting in a higher response. So, with increased p_t, we expect an increase in response.

This trend would be the case if there were no other biases or effects, but many criteria are implemented in event and jet selection. These result in biases in the jet response. One such bias is the threshold effect. The jet reconstruction algorithm functions best above a certain jet p_t due to the expected background noise. This threshold is calculated in MC simulations, and jets that fall below this threshold are not reconstructed as jets but rather left as particles. This limitation causes a bias at low momentum. The energy response for a certain jet p_t is not a particular value; there is a distribution of responses due to the statistical nature of the calorimeter shower. Some jets may have a high response (for example, if all the nuclear interactions happen to produce π^0s), and conversely, some may have a very poor response.

Near the jet reconstruction threshold, fluctuations in the response can cause jets to cross the threshold and pass or fail the p_t cut. The cross-section of jet production falls very steeply with jet p_t, resulting in more jets that fluctuate over the threshold than those that fluctuate down below the threshold. This bias manifests as an upturn of the response curve near the threshold. The expected shape is shown in figure 3.10.

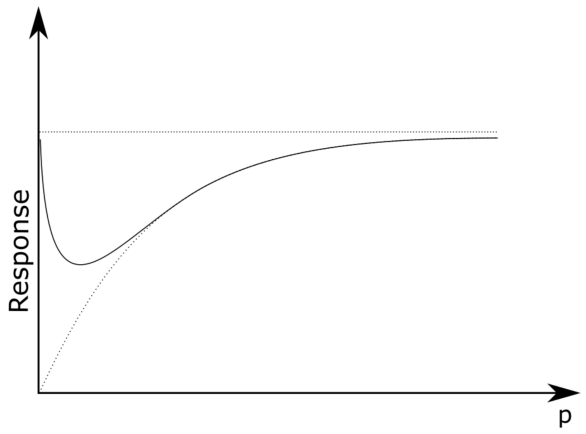

Figure 3.10: The expected response shape accounting for the threshold effect. Near the threshold, the recorded jets are biased towards higher response as lower response jets would fall below the threshold. The dashed curve shows the expected shape *without* any threshold.

Other factors cause an upturn at low momentum as well, such as the cuts used in the analysis (detailed later), and cluster reconstruction thresholds. These all cause the same upturn effect near the jet reconstruction threshold, and do not affect the response at higher p_t's. There is an extra feature expected for PFlow response curves. The response at low p_t is better due to tracking, but calorimetry is better at measuring energies at higher momenta. Therefore, PFlow switches from tracks to calorimeter clusters slowly, and the response curve should start dipping down to match the EMTopo curve at a certain jet momentum. The results presented in this thesis do not extend far enough to notice this effect.

3.3.3 Event Selection

Now that the goal is clear, the methods and criteria used to filter the large number of events is discussed. For the research presented here, the event of interest is one in which a Z boson is produced back-to-back in ϕ with a jet. The jet can be initiated by either a quark or a gluon. The Feynman diagrams of interest are shown in figures 3.7 and 3.8. In both diagrams, either a Z boson or a γ is present in the final state. The Z boson is studied via two of its decay channels:

1. $Z \rightarrow \mu^+\mu^-$
2. $Z \rightarrow e^+e^-$

These channels are chosen as the energies are well measured, yielding a good reference object. From here on out, both particle and anti-particle are referred to by their particle name (for example, the first process is written as $Z \rightarrow \mu\mu$). The topology of the required events has now been described; two leptons produced opposite a single jet. There is a possibility of extra jets in this type of event originating from radiation in the initial state (ISR) or the final state (FSR), and from the underlying event. For example, in figure 3.8, either quark in the initial state can spontaneously radiate a gluon, which results in a secondary jet. Similarly, the final state gluon can also emit a gluon, resulting in a secondary jet. These extra emissions will spoil the assumed p_t balance between the Z boson and the primary jet. Therefore, steps must be taken to avoid such events.

In order to search for these events, it saves time to take advantage of the DxAODs. These datasets have already been skimmed to find certain candidate events. The DxAOD collection used here is the JETM3 collection, which contains events with a $Z + jet$ structure, and further categorizes these into $Z \rightarrow \mu\mu$ or $Z \rightarrow ee$ subsets. The JETM3 collection contains events that pass either the single or di-lepton triggers for either electrons or muons, and requires that there be two leptons with $p_t > 20$ GeV. Further criteria (cuts) are applied in the analysis presented here in order to preferentially select events that do not have extra radiation.

The cuts relating to the Z boson done in the analysis are:

1. There must be exactly two leptons produced that are the same flavor (either electron or muon) and have opposite charges (must have both particle and anti-particle). The presence of fewer or more leptons hints at a different underlying process, and those events are removed.
2. The reconstructed Z mass must be in the range 66 GeV $<$ M $<$ 116 GeV. This requirement is loosely centered on the Z mass of 91.19 GeV.

The cuts relating to the electrons in the analysis are:

1. Electrons are identified by applying a cut on the output of a multivariate likelihood function analysis [5], which is based on measurements in different parts of the detector [30]. A list of these variables is shown in table 3.1. The Loose Selection Level is used.

2. Must pass lowest unprescaled triggers for two loose electrons.

   - Not all triggers need to or are able to run at the full rate dictated by the LHC; there are just too many events. Instead of saving all interesting events, a prescaled trigger chooses to save a certain fraction instead, and this fraction is the prescale factor. Events saved that rely on prescaled triggers have to correct for this reduced count.
   - The triggers used for this analysis are listed in Appendix B.

3. Must be in range of the tracking detectors: $|\eta| < 2.47$.

4. Must not be in the transition region between the barrel and endcap: NOT $(1.37 < |\eta| < 1.52)$.

5. Must have $p_t > 20$ GeV.

6. Loose isolation level, meaning the requirement that the electron object is isolated from any other object is not very strict, but it must still be reasonably isolated.

   - An isolation energy is defined by looking at a cone of $R = 0.2$ around the electron, and summing all the transverse energies as measured from topoclusters that fall within this cone. The electron energy is then estimated as the readings from a rectangle of cells (5x7 cells), and this energy is subtracted from the total energy of the cone. After compensating for electron energy leakage outside of the rectangle of cells and pile-up/UE corrections are implemented, the energy left is due to other activity in the event that was near the electron. The loose isolation level requires that $E_T^{isol}/p_T^{el} < 0.20$.

Type	Description	Name	Rejects			Usage
			LF	γ	HF	
Hadronic leakage	Ratio of $E_T$in the first layer of the hadronic calorimeter to $E_T$of the EM cluster (used over the range $\|\eta\| < 0.8$ or $\|\eta\| > 1.37$)	R_{had1}	x	x		LH
	Ratio of $E_T$in the hadronic calorimeter to $E_T$of the EM cluster (used over the range $0.8 < \|\eta\| < 1.37$)	R_{had}	x	x		LH
Third layer of EM calorimeter	Ratio of the energy in the third layer to the total energy in the EM calorimeter. This variable is only used for $E_T< 80$ GeV, due to inefficiencies at high E_T, and is also removed from the LH for $\|\eta\| > 2.37$, where it is poorly modelled by the simulation.	f_3	x			LH
Second layer of EM calorimeter	Lateral shower width, $\sqrt{(\Sigma E_i \eta_i^2)/(\Sigma E_i) - ((\Sigma E_i \eta_i)/(\Sigma E_i))^2}$, where E_i is the energy and η_i is the pseudorapidity of cell i and the sum is calculated within a window of 3×5 cells	$w_{\eta 2}$	x	x		LH
	Ratio of the energy in 3×3 cells over the energy in 3×7 cells centred at the electron cluster position	R_ϕ	x	x		LH
	Ratio of the energy in 3×7 cells over the energy in 7×7 cells centred at the electron cluster position	R_η	x	x	x	LH
First layer of EM calorimeter	Shower width, $\sqrt{(\Sigma E_i (i - i_{\max})^2)/(\Sigma E_i)}$, where i runs over all strips in a window of $\Delta\eta \times \Delta\phi \approx 0.0625 \times 0.2$, corresponding typically to 20 strips in η, and $i_{\max}$ is the index of the highest-energy strip, used for $E_T > 150$ GeV only	w_{stot}	x	x	x	C
	Ratio of the energy difference between the maximum energy deposit and the energy deposit in a secondary maximum in the cluster to the sum of these energies	E_{ratio}	x	x		LH
	Ratio of the energy in the first layer to the total energy in the EM calorimeter	f_1	x			LH
Track conditions	Number of hits in the innermost pixel layer	n_{Blayer}		x		C
	Number of hits in the pixel detector	n_{Pixel}		x		C
	Total number of hits in the pixel and SCT detectors	n_{Si}		x		C
	Transverse impact parameter relative to the beam-line	d_0		x	x	LH
	Significance of transverse impact parameter defined as the ratio of d_0 to its uncertainty	$\|d_0/\sigma(d_0)\|$		x	x	LH
	Momentum lost by the track between the perigee and the last measurement point divided by the momentum at perigee	$\Delta p/p$	x			LH
TRT	Likelihood probability based on transition radiation in the TRT	eProbabilityHT	x			LH
Track–cluster matching	$\Delta\eta$ between the cluster position in the first layer and the extrapolated track	$\Delta\eta_1$	x	x		LH
	$\Delta\phi$ between the cluster position in the second layer of the EM calorimeter and the momentum-rescaled track, extrapolated from the perigee, times the charge q	$\Delta\phi_{res}$	x	x		LH
	Ratio of the cluster energy to the track momentum, used for $E_T>$ 150 GeV only	E/p	x	x		C

Table 3.1: The many variables and cuts used when determining whether an object is an electron or not. LH stands for variables used in the likelihood function, and C refers to variables that are used as hard cuts [30].

The cuts relating to muons are:

1. Loose selection and isolation levels.

    - There are 4 different types of measured muons [25]:
        (a) Combined (CB) muon: track reconstruction is performed independently in the ID and the MS, and the tracks are combined with a global refit.
        (b) Segment-tagged (ST) muons: if a track in the ID, once extrapolated to the MS, can be associated with a track in the monitored drift tube or cathode strip chambers in the MS, that track is classified as a muon.
        (c) Calorimeter-tagged (CT) muons: if a track in the ID can be successfully matched to an energy deposition in the calorimeter that looks like a minimum-ionizing deposition, that track is classified as a muon.
        (d) Extrapolated (ME) muons: the muon is reconstructed using only the track in the MS, and a loose requirement on the track matching with the interaction point.
    - Overlap between the 4 types is fixed as follows [25]:
        – If two muon types have the same track, priority is given in the order CB, ST, and lastly CT muons.
        – Overlap with ME muons is settled by looking at the track hits, and picking the track with a better fit and more hits.
    - There are a few variables used in the identification of a muon [25]:
        – q/p significance: "defined as the absolute value of the difference between the ratio of the charge and momentum of the muons measured in the ID and MS divided by the sum in quadrature of the corresponding uncertainties." [25]
        – ρ': "defined as the absolute value of the difference between the transverse momentum measurements in the ID and MS divided by the p_T of the combined track."[25]
        – The normalized χ^2 of the combined track fit.
        – The number of hits in the ID and MS.
    - The loose selection level is defined as considering all 4 types of muons [25]:
        – All CB and ME muons satisfying the medium selection are used. The criteria are that CB muons must have ≥ 3 hits in two or more MDT layers; the ME muons must have ≥ 3 hits in separate MDT/CSC layers. The ME muons are only used for $2.5 < |\eta| < 2.7$.
        – The CT and ST muons are restricted to the $|\eta| < 0.1$ region.
        – For $|\eta| < 2.5$, the distribution of loose muons is: 97.5% CB, 1.5% CT, and 1% ST muons.

2. Must pass the lowest unprescaled triggers for two loose muons.
    - The exact triggers are listed in Appendix B.
3. Must be in the range of the tracking detectors: $|\eta| < 2.47$.
4. Must have $p_t > 20$ GeV.

Once the Z boson selection criteria are applied, a series of cuts is implemented to ensure the correct event topology:

1. The goal here is to measure the JES in the central region of the detector, so $|\eta_{jet}| < 0.8$
    - An η intercalibration (first step of the in-situ calibrations) uses p_t balance in dijet events to correct the energy scale of forward ($0.8 \leq |\eta| \leq 4.5$) jets to match the calibrated central region jets.
2. The leading jet must be back-to-back with the reference object, so $\Delta\phi(jet_{lead}, ref) > \pi - 0.25$
3. There must not be a significant sub-leading jet in the event, so $p_t^{subjet} < \min(12\,GeV, 0.3 \cdot p_t^{ref})$
4. $JVT > (0.59, 0.2)$, to reject pile-up jets for (EM,PFlow) scales [24, 4]:
    - The JVT stands for Jet Vertex Tagger, which is the output of a two-dimensional likelihood analysis using the corrJVF and R_{p_t} variables.
    - A jet has tracks associated to it via ghost association. The p_t of these tracks can be summed. The sum is done for all tracks in the jet, as well as all tracks that originate from a given primary vertex (PV). Taking the ratio of these sums yields the *jet vertex fraction* (JVF).

$$JVF(jet_i, PV_j) = \frac{\sum_{PV_j tracks} p_{t,i}^{track}}{\sum_{allPV} \sum_{PV_j tracks} p_{t,i}^{track}} \tag{3.13}$$

    - As pile-up increases, the number of scattering vertices increases, reducing the JVF. The JVF can be corrected for this effect, and is called the corrJVF.
    - Taking the p_t sum of the tracks in the jet that come from the hard-scatter vertex, and comparing it to the calibrated jet p_t defines a response. This response only relies on the hard scatter, and so is independent of N_{PV}.

$$R_{p_t} = \frac{\sum_{PV_{HS}} p_{t,i}^{track}}{p_t^{jet}} \tag{3.14}$$

- For each corrJVF and R_{p_t} point, the relative probability that a jet is signal-type is found by computing the ratio of the number of hard-scatter jets to the number of hard-scatter plus pile-up jets in simulated dijet events [24].
- For a jet, its corrJVF and R_{p_t} values are computed, and the JVT value is set by referring to the simulation-derived signal-type probability for those values [4].
- The JVT cut for PFlow is looser as PFlow has an inherent track-based cut that filters out bad events.

5. The calibrated leading jet must have $p_t > 12$ GeV.

The $\Delta\phi$ and the sub-leading jet cuts serve to reject events with radiation in the initial or final states (ISR and FSR). A sub-leading jet resulting from ISR/FSR would throw off the back-to-back balance of the leading jet and the reference object. The $\Delta\phi$ and sub-leading jet cuts may be correlated, but they were found to be essentially independent in earlier studies [10, 41]. It was found that the $\Delta\phi$ cut is sensitive predominantly to ISR, while the sub-leading jet cut deals with the FSR. The reason behind this is not yet understood.

One final requirement is placed on jets to ensure that good jets are used; the *BadLoose* requirement [6], which filters jets with criteria that:

- Reject jets due to sporadic noise bursts in the calorimeter.
- Reject jets due to large coherent noise or isolated pathological calorimeter cells.
- Reject jets due to hardware issues, beam-induced background, and cosmic muon showers.

3.3.4 Systematic Uncertainties

Determining the uncertainty on the calibration is just as important as the calibration itself. With a detector as complex as ATLAS, one must be careful and thorough in the treatment of uncertainties. Any calibration, correction, or cut may be a source of error known as a *systematic error* (called systematics for short). In the MPF method, everything other than the two leptons is studied via calorimeter clusters. These leptons must be calibrated after reconstruction to ensure that the assumption of a 'well-defined reference object' holds. At ATLAS, these calibrations are found by analyzing MC simulations and comparing the detector results to the truth, as well as test-beam data and measurements of the reconstructed Z invariant mass. The calibrations can correct for effects such as energy missed in the reconstruction, accounting for where the energy was deposited, corrections derived from the Z mass peak, and the energy resolution in MC being too good compared to data [7, 25].

The calculation of a systematic variation is done using three values: a nominal value, and two alternate values. These are either tight/loose values where the restrictions are more stringent/less strict, or by varying the systematic by $\pm 1\sigma$. By comparing the effect of varying the associated systematic through these values on the MPF response, the uncertainty can be inferred.

The systematics related to the leptons are:

1. EGamma Resolution: The electron resolution used in the MC is too good (it is known exactly). It is not possible to know the energy that well in data, so the energy must be smeared in MC to match the data. The smearing is Gaussian, and the loose/tight variations change the smearing by $\pm 1\sigma$ (typically a change of 0.001). This applies only to electrons.

2. EGamma Scale: The energy scale that is applied to electron objects to calibrate them. This also has a Gaussian distribution, and the scale is varied by $\pm 1\sigma$ (typically a change of 0.01).

3. Muon Inner Detector: The energy resolution of muons in MC, as derived from the Inner Detector, is too good compared to data, so it must be smeared to match the data. This smearing is Gaussian and is varied by $\pm 1\sigma$ (typically a change of 0.001). This systematic only applies to muons.

4. Muon Spectrometer: The energy resolution of muons in MC, as derived from the Muon Spectrometer, is too good compared to data, so it must be smeared to match the data. This smearing is Gaussian and is varied by $\pm 1\sigma$ (typically a change of 0.001). This systematic only applies to muons.

5. Muon Scale: The energy scale that is applied to muon objects to calibrate them. This is also Gaussian, and the scale is varied by $\pm 1\sigma$ (typically a change of 0.01).

The systematics related to jets are listed below (reported in the format loose-nominal-tight). These are motivated by the effect these cuts have on the suppression of events with initial and final state radiation. By varying these cuts, the effect that next-to-leading order Feynman diagrams have on the results is studied.

1. Sub-leading Jet p_t cut, absolute value: The sub-leading jet momentum cut that limits the presence of secondary jets is the minimum of an absolute cut and the relative cut. The absolute cut is varied through 15-12-10 GeV.

2. Sub-leading Jet p_t cut, relative value: The sub-leading jet momentum cut is the minimum of the absolute cut (listed above) and the relative cut (which is relative to the reference object). The relative cut is varied through (0.4-0.3-0.2)$\cdot p_t^{ref}$.

3. JVT: The JVT cut rejects pile-up jets and ensures that the jets used in the analysis come from the primary vertex. There are different cut values for EMTopo and PFlow scales. For EMTopo, the variance is 0.11-0.59-0.91, while for PFlow, the variance is 0-0.2-0.5. The discrimination power of the JVT can be seen in figure 3.11.

4. $\Delta\phi$: The cut that relates to the azimuthal separation of the jet and the reference object. In the ideal case, these objects are back-to-back, and the separation would be π. This cut is varied through 2.8-2.9-3.0.

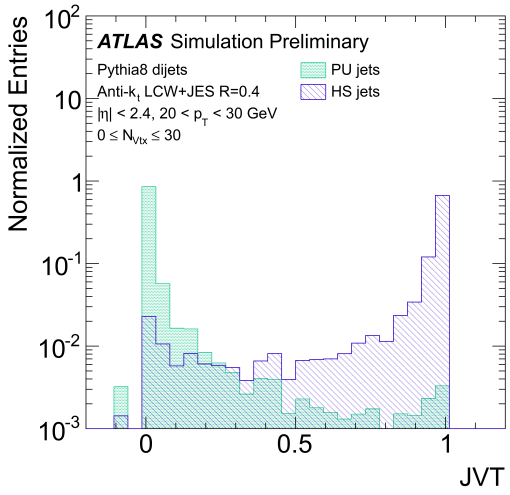

Figure 3.11: [4] The distribution of pile-up (PU) jets and hard scatter (HS) jets vs JVT for the LC scale. There is clear discrimination power here, and the JVT cuts are optimized to reject background.

In order to ensure that the results are statistically significant, a bootstrapping procedure is implemented [17]. In this procedure, for each event and for each uncertainty, 100 different copies of the event are made. In each copy, a set of systematic source values are generated by taking a random weight from a Poisson distribution and applying it to the nominal value. Each of these new systematic values are then used in the calculation of the MPF. The relative uncertainty for a pseudo-event can be found by

$$\delta S = \frac{varied - nominal}{nominal} \tag{3.15}$$

The result is a distribution of changes rather than one value. The mean of the distribution is taken as the overall effect. After this, a rebinning/smoothing procedure is applied that looks at each bin in the systematic uncertainty histogram and its surrounding bins. If a fluctuation has less than 2σ significance compared to neighbors, the bins are combined. This has the effect of smoothing out statistical fluctuations in the uncertainty while maintaining key features such as general trends and statistically significant bumps.

Two final uncertainties must be taken into account that are not event-by-event effects. These must be derived after all results have been combined and analyzed.

1. MC Modelling: two MC generators are chosen that are very different, and the ratio of the two MC response curves is taken as an uncertainty to cover all possible choices of generators in subsequent physics analyses. There are many options for generators, and it would require too many resources and time to produce a calibration for each generator. By producing calibrations based on MC generators that treat QCD very differently, any variation in a possible generator-dependent jet calibration should be taken into account. The generators differ in how they model the hadronization process (which occurs at the low-energy regime in which QCD cannot be treated perturbatively).

2. Statistical: this uncertainty comes from the width of the distributions that are fitted for each p_t bin and covers the statistical fluctuations inherent in the jet energy calculation (each jet is different).

There are other uncertainties that can be considered, but work from the respective muon and electron groups, as well as past MPF calculations, have shown that the systematics listed above are the important ones; the rest are negligible.

Chapter 4

Software

In this chapter, the analysis software developed and used will be detailed and discussed. Its location, structure, and usage will be outlined, as well as discussion of the studies that were made. This chapter can be skipped without loss of continuity.

The analysis framework has been rewritten using the general structure left by my predecessor Jamie Horton. The initial rewrite was needed in order to facilitate the change to ATLAS' new central compiling system; CMake. The previous twenty releases of the ATLAS compilation environment relied on the ATLAS-made RootCore. For the 21st release, the transition to CMake (a commercial and centralized compiler) was done, which required a large-scale overhaul of all code at ATLAS. This transition is an on-going effort to this day. Since the move to release 21 (R21), the MPF analysis framework has been rewritten once more in order to integrate large-R jet functionality. Setup and use of the code has been automated (unpacking, setup, and job submissions), and many different studies and outputs have been added to the framework. The analysis code works by reading in DAODs (as outlined in chapter 2.6), and provides as output a tree of histograms.

4.1 Where to Find the Framework

The latest version of the InSituJES analysis framework can be found at the following CERN software repository:

https://gitlab.cern.ch/atlas-jetetmiss-jesjer/Insitu/MPF/-/tree/R21

The master branch (as of the writing of this thesis) is an outdated version kept present for reference purposes. The branch entitled 'R21' contains the latest version of the framework, and is capable of producing both small-R and large-R jet results. It is written in the C++ language, using the CERN Root data analysis framework [18], compiled with CMake. Root is a library in C++ developed at CERN, which contains functions/features needed for particle

physics analyses (such as premade histogram objects, easy plotting, histogram combination functions, and more). Permission is required to access the repository.

The overall layout of the code is as follows:

- **functionSetup.sh**: a file of shell scripts that execute common strings of commands for easy setup and use.
- **getPckg.sh**: the shell file that downloads centralized packages needed to run the framework.
- **README.md**: a small text file that outlines the basic usage of the code
- **notes/**: some text files outlining information about the framework
- **build/**: the folder in which the project is compiled
  - **.gitkeep**: an empty hidden file
- **run/**: the folder in which the code should be executed
  - **.gitkeep**: an empty hidden file
- **source/**
  - **.gitignore**: an empty hidden file
  - **CMakeLists.txt**: a key file that tells CMake how to compile the project
  - **InSituJES/**: the main source code folder.
    - **InSituJES/**: folder containing header files. All of the function prototypes are defined here, as well as all of the global variables.
    - **Root/**: folder containing the .cxx source files that contain the analysis code. There are three files: JESAnalysis, EventFilter, and ObjectFilter. The JESAnalysis file contains all histogram initializations (as defined in section 4.3), the trigger check, MET calculations, saving of histograms, and the majority of the additional calculations. Two filters are reserved mainly for applying calibrations and cuts. EventFilter contains event-level cuts (such as topology cuts) and the application of some calibration tools (such as jet calibration). ObjectFilter contains object-level cuts (such as cuts related to the number of leptons and their charge), as well as calibrations of the photons/leptons.
    - **share/**: folder containing configuration files where all of the job options are defined (as listed in section 4.4). "configFile" contains the job options for one run, while all the batch files (normally beginning with the term "ZJet") encompass all multi-run options. Inside the **Selections/** folder are

configuration files related to the photon/leptons that sets the object-level cuts, as well as the triggers.

- **util/**: folder containing executables and steering macros. RunLocal runs the code using the settings found in configFile, RunGrid sends the same code to the GRID, and RunBatch reads the batch configuration files and submits all of the jobs to the GRID.
- **CMakeLists.txt** : a key folder telling CMake how to compile the source code in this folder.

The code hierarchy is structured into three main folders: build, run, and source. The source folder is where the code is contained, the build folder is where the code is compiled, and the run folder is meant to be the directory from which the code is executed. The build and run folders can be changed (for example, one might have a different folder entitled build2 from where users can compile code using a different version, or one can write/compile/run all from the same folder), but this directory structure is recommended.

The analysis code relies on a development framework called EventLoop. All data-reading, as well as the loop over files and the events contained therein are handled by EventLoop automatically. Wrapper functions are provided which run at specific points in the loop (such as once at the start, when changing files, or per-event), and the user has to fill in their code. The functions and their use is outlined in section 4.2.

4.2 How the Framework Works

The flow of the code is dictated by the EventLoop structure. EventLoop is a prewritten framework that acts as a wrapper for the user analysis code. The loop over every event is automatically handled, with empty functions provided that are run at specific instances in the loop. The user must fill these functions with the desired functionality. For example, in the EventLoop function that runs once for every event, the user can code their event-by-event calculations (such as the MET calculation and filling the related histograms). For the InSituJES framework, the EventLoop functions are defined in JESAnalysis.cxx. The given EventLoop functions are:

1. **JESAnalysis()**
    - The algorithm constructor. The trigger decision tool and the trigger configuration tools are initialized here.
2. **~JESAnalysis()**
    - The algorithm destructor. All tools and memory allocations are cleared throughout the code after use. However, the histograms that are saved need to be present at all times in order to save the information. In the destructor, these histograms are marked as complete and closed, saved to the output, and the associated pointers are deleted.
3. **setupJob()**
    - This function sets up running options, such as adding file readers or setting up multiple output files. The InSituJES framework only uses this to tell EventLoop that DAODs (as defined in section 2.6) are being used. The code uses the default output file that is automatically defined.
4. **histInitialize()**
    - This is where the code truly begins. All histograms are defined here, and the configuration files containing the job options are read in. The channel (electron, muon, or photon), running location (local or grid), lumicalc files, pileup reweighting files, all job configurations and flags (as defined in section 4.4), and the relevant p_t bins are set here.
    - The EventFilter is also initialized here, which further creates the ObjectFilter. By doing so other tools are made, cuts are read in, and trigger names are set. The tools initialized here are:
        - The Good Runs List processing tool.

  - The Jet Calibration Tools (with and without GSC for large- and small-R jets)
  - The Jet Cleaning Tool
  - The Muon Calibration and Smearing Tool
  - The EGamma Calibration and Smearing Tool
  - The MET Systematics Tool
  - The METMaker
- The cutflow is defined as well (which cuts are applied when and where will be detailed in this section).

5. **fileExecute()**
   - Here everything that needs to be done exactly once per file is coded. This function is not used for this analysis.

6. **changeInput()**
   - Everything that needs to be done every time input files are changed is coded here. The InSituJES framework reads in the pileup reweighting factors here for MC samples (MC events are weighted in order to reproduce the μ distribution seen in data, and these scales have to be considered). In the past this was done by consulting PyAMI (a dataset information website), and the reweighting factors were coded in manually, but this has now been changed to be automatic.

7. **initialize()**
   - This function is called after the first input file has been opened, but before the first event is processed. Many ATLAS tools are initialized here and configured. The tools configured here are:
     - The Pileup Reweighting Tool
     - The Trigger Configuration Tool
     - The Isolation Correction Tool
   - This is also where all the objects used for the study of systematic uncertainties are created.
   - Some basic information is saved here, such as: the channel (electron, muon, or photon), the jet collection (EMTopo, LCTopo, or PFlow), and which MC generator is being read in (Pythia or Sherpa).

8. **execute()**
   - This function defines what is done for every event, and is where almost the entirety of the analysis code is located.

- First, the pile-up reweighting weights are read in and set for use throughout the analysis. These weights are used when filling histograms, so they are globally set, and are referenced with each fill command.
- Following this, the EventFilter is called to determine whether the event passes the MPF selection criteria. This is done through the **PassVJet()** function.
  - After lepton cuts are applied, the reference selection criteria are applied.
  - If photons are being studied:
    (a) The requirement of having at least one photon is applied.
    (b) The EGamma Calibration and Smearing Tool is applied, and the event is rejected if the photons cannot be calibrated.
    (c) The leading (highest p_t) photon is then selected for analysis.
    (d) The ObjectFilter is then applied through the function **PassPhoton()**. The photon cuts this applies are (in order): loose ID selection, p_t cut, η cut, and the isolation selection cut.
  - If electrons are being studied:
    (a) The requirement of having at least one electron is applied.
    (b) The EGamma Calibration and Smearing Tool is applied, and the event is rejected if the electrons cannot be calibrated.
    (c) The ObjectFilter is then applied through the function **PassElectron()**. The electron cuts this applies are (in order): loose ID selection, p_t cut, η cut, and the isolation selection cut.
    (d) After the ObjectFilter has been applied, the selected electrons are passed through three more cuts: there must be *exactly* two electrons remaining, they must have opposite charge, and they must pass the reconstructed Z mass cut.
  - If muons are being studied:
    (a) The requirement of having at least one muon is applied.
    (b) The Muon Calibration and Smearing Tool is applied, and the event is rejected if the muons cannot be calibrated.
    (c) The ObjectFilter is then applied through the function **PassMuon()**. The muon cuts applied are (in order): loose ID selection, p_t cut, η cut, and the isolation selection cut.
    (d) After the ObjectFilter has been applied, the selected muons are passed through two more cuts: there must be *exactly* two muons remaining, they must have opposite charge, and they must pass the reconstructed Z mass cut.

- Following the cuts related to the reference object reconstruction, the METMaker tool is given the selected photon/leptons as well as the jet collection, and is run to yield the MET in the event (METMaker calculates its own soft term, only requiring the hard objects in the event).
- Then, the **CheckJets()** function is called, which applies the jet selection criteria, as well as the event topology criteria.
  (a) If there are no jets, the "number of good jets" cut is failed.
  (b) The jets are then calibrated using the Jet Calibration Tool.
  (c) If there is a jet above 20 GeV that cannot be calibrated, the "number of good jets" cut is failed.
  (d) The calibrated jets are then sorted in a descending p_t order. If there are no jets left after calibration, the "number of good jets" cut is failed.
  (e) The calibrated jets are then looped over, and the jet isolation cut is applied (overlap removal with photons/leptons), followed by the JVT cut and its associated η and p_t cuts.
  (f) If after these cuts are applied there are no jets left, the "jets after overlap removal" cut is failed.
  (g) Similar steps are then done for large-R jets. The large-R and small-R jet code converge after the large-R calibration and selection criteria are complete.
  (h) The highest p_t jet from the isolated calibrated jets list is selected for analysis and called the leading jet.
  (i) The second highest p_t jet from the isolated calibrated jets list is selected as the sub-leading jet.
  (j) The leading jet p_t and η cuts are applied, followed by the $\Delta\phi$(leading jet, reconstructed reference) and the sub-leading jet p_t cuts.

- After the selection criteria have been applied and met, the triggers are checked, and the trigger cut is applied.
- The MET is then calculated (using either the METMaker results or by custom methods that will be detailed in sections 5.2.2 and 5.3.2) in a function called **CalculateMET()** which contains all variations of the MET reconstruction. This is the MET calculator that is separate from the METMaker tool (although it can be set to just reading in the METMaker results).
- Following this, all information in the event needed for studies is saved and the histograms are filled. This complete list will be detailed in section 4.3.

9. **postExecute()**

    - Everything that needs to be done immediately after the event has finished processing but before the next event is called is done here. This function is left empty for this analysis.

10. **finalize()**

    - The function in which objects can be cleaned up and closed before they are written to disk. For this analysis, the instance of the pile-up tool is finalized and deleted as required, and final event selection information is displayed to the console (such as number of events entering and passing the trigger and total number of events passing selection) for confirmation when reading the logs.

11. **histFinalize()**

    - Here is where final touches to histograms are done before they are written to disk. The InSituJES framework simply labels the bins in the cutflow histograms, and deletes the event and object filters.

12. Following this, there are a large number of helper functions which do book-keeping tasks, and it is not informative to go over them in detail.

4.3 List of Studies/Outputs

There are a large number of studies that are run every time the code is executed. These studies are best summarized by writing what information is saved, and what it is used for. The output file is comprised of a large number of histograms, which can be analysed to create key plots. The histograms saved are:

1. histEventCount - the number of events, needed to reweight Sherpa samples properly.
2. MPF_CutInfo - contains the cutflow using the MPF selection criteria.
3. Bal_CutInfo - contains the cutflow using the DB selection criteria.
4. Isolation - contains the photon isolation energy.
5. Weights - contains the pile-up reweighting information.
6. SumWeights - contains summed pile-up reweighting information.
7. METx - the missing E_T distribution in the x-direction for whichever method of MET calculation was used in the analysis.

8. METy - the missing E_T distribution in the y-direction for whichever method of MET calculation was used in the analysis.

9. ResponseLoose - for photons, MPF response using LooseNotTight photons.

10. BalanceLoose - for photons, MPF response using LooseNotTight photons.

11. IsEMIsolCone - contains photon isolation information to be used for photon purity studies. Has multiple versions, one for each p_t bin.

12. IsEMIsolConeBal - same as above, but for DB instead of MPF.

13. JetPt - calibrated leading jet p_t distribution.

14. UncalJetPt - uncalibrated leading jet p_t distribution.

15. JetEta - calibrated leading jet η distribution.

16. LeptonPt - lepton p_t distribution.

17. RefPt - reconstructed Z p_t distribution.

18. RefEta - reconstructed Z η distribution.

19. RefMass - reconstructed Z mass distribution.

20. MuVsRho - average interactions per crossing vs pile-up energy density in the event.

21. AvInt - the average interactions per crossing distribution.

22. NPV - the number of primary vertices distribution.

23. AppliedJES - the applied MCJES distribution.

24. AppliedGSC - the applied GSC distribution.

25. Response - two-dimensional MPF response distribution which can be cut into p_t bins, projected, and fit to get the key response curves.

26. Balance - same as above, but for DB response.

27. ResponseNoGSC - the two-dimensional MPF response distribution, but using jets without the GSC applied.

28. BalanceMPFRatio - the DB/MPF ratio distribution.

29. Mapping - leading jet p_t vs reference p_t, can be used to map x-axes in plots.

30. MPF - all p_t inclusive one-dimensional MPF distribution.

31. JetPt_bal - DB leading jet p_t distributions
32. JetEta_bal - DB calibrated leading jet η distribution.
33. LeptonPt_bal - DB lepton p_t distribution.
34. RefPt_bal - DB reconstructed Z p_t distribution.
35. RefEta_bal - DB reconstructed Z η distribution.
36. RefMass_bal - DB reconstructed Z mass distribution.
37. AvInt_bal - the averave interactions per crossing distribution for the DB selection criteria
38. NPV_bal - the number of primary vertices distribution for the DB selection criteria.
39. Mapping_bal - leading jet p_t vs reference p_t for the DB selection criteria.
40. Balance_Truth - truth jet p_t / $|p_t^Z \times \cos(\Delta\phi(Z, leadingjet))|$
41. Balance_Truth - balance_truth but with photon scale factors applied.
42. RecoTrueRatio - leading jet p_t / ghost truth jet p_t
43. TrueResponse - pile-up scale leading jet p_t / ghost truth jet p_t
44. MPFTrueRatio - TrueResponse / calculated MPF response.
45. TrueMF - ghost truth association factor distribution.
46. ResponseVsPileup - MPF response in bins of μ, NPV, and p_t.
47. BalVsPileup - DB response in bins of μ, NPV, and p_t.
48. Channel - histogram with information regarding which of electrons/muons/photons are being analysed.
49. Collection - EMTopo, LCTopo, or PFlow.
50. Sample - Data, nominal MC, or alternate MC.
51. ClusOverEl - cluster energy compared to electron p_t.
52. ClusOverUncalEl - cluster energy compared to uncalibrated electron p_t.
53. CalClusOverEl - calibrated cluster energy compared to electron p_t.
54. CalCluseOverUncalEl - calibrated cluster energy compared to uncalibrated electron p_t.

55. CalElOverUncalEl - comparing calibrated and uncalibrated electron p_t.

56. RaxBalance - DB response without calibrations applied.

57. dPhiLep1Jet - $\Delta\phi$ between the leading lepton and the leading reconstructed jet.

58. dPhiLep2Jet - $\Delta\phi$ between the sub-leading lepton and the leading reconstructed jet.

59. PhiLep1 - the ϕ distribution of the leading lepton.

60. PhiLep2 - the ϕ distribution of the sub-leading lepton.

61. j2dphi variations - set of three-dimensional histograms that contain information about how the MPF response varies as the sub-leading jet cut and the $\Delta\phi$ cuts are varied simultaneously.

62. ResponseVsRad - set of two-dimensional histograms that contain information about how the MPF response varies as the sub-leading jet cut and the $\Delta\phi$ cuts are varied independently.

63. ResponseVsJetEta - MPF response as a function of leading jet η.

64. BalanceVsJetEta - DB response as a function of leading jet η.

65. ResponseVsJetDistances - MPF response vs $\Delta\phi$(leading jet, sub-leading jet).

66. EnergyRing - the energy density in rings around the leading jet axis.

67. ClusterVar_R - the MPF response distribution as the ClusterMET (the custom MET calculation outlined in section 5.2.2) lepton-associated cluster exclusion cone size is varied.

68. ClusterVar_dR - the MPF distribution if the ClusterMET method uses a small ring of size dR outside of the lepton-associated cluster exclusion cone to estimate the pile-up as opposed to the energy density in the event.

69. MuonEnergyRing - the energy density in rings around muons.

70. LeptonPhi - the lepton ϕ distributions in bins of p_t and η.

The associated histograms are saved every time the code is run given that they are useful; for example, photon purity studies will not be saved if photons are not being studied. A large collection of plotting scripts has been written, but the details of these are outside of the scope of this thesis.

4.4 How to Run the Analysis

The InSituJES framework has been largely automated in order to allow for easy and consistent application. The code hierarchy was outlined in section 4.1. In the **source/** folder are two folders called **util/** and **share/**. The former contains the steering macros, the most useful of which are RunLocal and RunBatch. The latter contains all the configuration files. The important ones here are "configFile" and "ZJet_(...)." The configFile is the configuration file for a single run (local or on the grid), while the ZJet files are batch configuration files that allow for multiple jobs/configurations to be submitted to the grid.

All the required parameters (e.g. cuts, event selection) are defined in configFile. For the jet calibration files, one should consult the latest recommendations from the JetETMiss group to get the names and versions correct. The parameters found in the configFile are:

- OutDir - the location where local output files should be saved.
- LocalInputDir - the directory that contains the local data files.
- GridInputDir - the name of the dataset to be analysed on the grid. Can be wildcarded.
- GridOutName - the name of the output files to be generated on the grid.
- doJER - flag that sets whether the Jet Energy Resolution (JER) calculations are to be run or not.
- selectionFile - Electron, Muon, or Photon.
- JetCollection - which jet collection to analyse. Can be "AntiKt4EMPFlowJets" or "AntiKt4EMTopoJets."
- METConfigVersion - the flag that determines which MET calculation to do. The options are:
    1. RawMETMaker - simply use the default METMaker results
    2. METMaker_rho - use the METMaker results, but add in a correction that accounts for the pile-up around the lepton.
    3. ClusterMET_replace - calculate the MET from clusters, and replace lepton clusters with leptons and add in the pile-up. This is the nominal configuration.
    4. ClusterMET_MuonOnly - the ClusterMET method, but do not remove the clusters, simply add in the muons. This is here for testing purposes.
    5. ClusterMET_Muon_EnergyLoss - same as ClusterMET_MuonOnly, but read in the muon energy loss correction from METMaker and add that in as well.

- LargeRJetCollection - which large-R jets to use. Set to "none" to do a small-R jet analysis.
- J2dPhiStudies - flag that turns on the MPF vs sub-leading jet and $\Delta\phi$ cuts variation studies. Turning this on will disable all other histograms in the analysis.
- j2Range - the range over which the sub-leading jet cut will be varied. In the format low-high,nBins.
- dPhiRange - the range over which the $\Delta\phi$ cut will be varied. In the format low-high,nBins.
- isMC - set this to "true" if the dataset being analysed is a MC simulation. Otherwise set to "false."
- grl - the location of the correct GoodRunsList.
- lumicalc - the run year for the correct luminosity file. Can be set to "data15," "data16," "data17," or "data18."
- prw - the name of the correct pile-up reweighting file. This file must be located in **share/Pileup/**.
- doSystsMPF - the flag that sets whether systematic uncertainties will be analysed for MPF or not.
- doSystsBal - the flag that sets whether systematic uncertainties will be analysed for DB or not.
- numPseudoExp - the number of pseudo-experiments to generate for the systematics.
- configName - the name of the EMTopo jet calibration file (contains options like applying the pile-up correction, which method to use to extrapolate the calibration below the minimum E_T and what that minimum is, etc).
- chainName_MC - the EMTopo jet calibration chain without the GSC or an older in-situ calibration.
- chainName_GSC - the EMTopo jet calibration chain with the GSC step included, but without an older in-situ calibration.
- chainName_Insitu - the complete EMTopo jet calibration chain.
- calibarea - the version of the EMTopo jet calibration files that is desired.
- AntiKt4EMPFlow_configName - the name of the PFlow jet calibration file

- AntiKt4EMPFlow_chainName_MC - the PFlow jet calibration chain without the GSC or an older in-situ calibration.
- AntiKt4EMPFlow_chainName_GSC - the PFlow jet calibration chain with the GSC step included, but without an older in-situ calibration.
- AntiKt4EMPFlow_chainName_Insitu - the complete PFlow jet calibration chain.
- AntiKt4EMPFlow_calibarea - the version of the PFlow jet calibration files that is desired.

The ZJet files provide a simple way to run a large number of jobs without needing to reconfigure all the parameters and monitor the submission process. The number of parameters needed to be set by the user is drastically reduced and the other relevant parameters are automatically tuned correctly by determining what they should be set to. For example, if the input dataset has a MC campaign tag, the flags designating the campaign run, whether the input is data or MC, the luminosity and pileup reweighting files, and the MC generator are set appropriately (these would have to be set individually otherwise). The basic entry in the ZJet batch configuration files is a row, with parameters separated by the delimiter "|." The entries per row are as follows:

1. n - the first entry in the row *must* be an integer value corresponding to the order of submission. The row marked as "1" will run first, followed by the row marked "2." The RunBatch script will start 1 and count up until it does not encounter the next number, and then will stop submitting jobs. This could be made to be simpler to use.
2. Scale - which jet collection to use is set here. This can be either "EM" for EMTopo or "EMP" for PFlow.
3. Systematics - which systematic studies to run. This can be set to either "sMPF" (which processes only MPF systematics), "sBal" (which processes only DB systematics), or "sBoth."
4. n Sys. - this sets how many pseudo-experiments need to be run for each systematic. Any integer value will do. Typically this is set to 100.
5. Input Dataset - this is where the dataset to be analysed is designated.
6. Output Names - the parameter that sets the name of the output file that is generated on the grid.
7. PRW Files - which pile-up reweighting file is correct to use for the input dataset.

In addition to these entries, there are also three universal parameters that can be set at the bottom of the batch file.

1. METConfigVersion
2. doLargeR
3. J2dPhiStudies

These are the same as the corresponding parameters defined above in the configFile parameters list, and have the same options here.

Once the configuration files have been set, running the code is as simple as one command. To run locally, execute the command "RunLocal." This will read the configurations in the configFile and run accordingly, displaying all information in the terminal window. To run on the grid, it is recommended to use the RunBatch steering macro and the ZJet batch configuration files even for a single job, as the reduced number of parameters allow for easy and consistent running. In order to do this, simply execute the command "RunBatch –batch [batch file]." The batch configuration file must be located in **source/share/** in order to be read correctly. If more flexibility is needed for grid jobs, the command "RunGrid" will read the configFile and submit to the grid.

Chapter 5

Results

5.1 Analysis Steps

Recall that the energy response of the recoil is given by:

$$R_{recoil} = 1 + \frac{\vec{E_T}^{miss} \cdot \hat{p_t}^{ref}}{E_T^{ref}} \tag{5.1}$$

Thus, in the calculation of the MPF response, there are two components:

1. The calculation of the p_t of the reference Z-boson by its decay to two leptons ($Z \rightarrow ee/\mu\mu$).
2. The calculation of the E_T^{miss}, also referred to as the MET.

The recoil response can be calculated from these two quantities. The steps taken in the analysis are as follows.

First, all objects in the event are calibrated in order to ascertain their properties as accurately as possible. Then the event is filtered by applying event selection cuts:

- The lepton related cuts are applied.
- The Z boson related cuts are applied.
- The event topology cuts are applied.

If the event fails any of these cuts, it is removed from consideration. The two leptons are calibrated using recommendations from the appropriate ATLAS Combined Performance (CP) group. The CP groups also provide the tools necessary to do the studies of the systematic uncertainties associated with that particle/quantity. The calibration of the jets is done via the jet calibration tool. The final correction in the calibration chain is being derived here, so only the previous steps in the chain are applied. Once the jets are calibrated, jet-related

cuts are applied to the leading and sub-leading jets in the event.

After the event has been deemed to be of interest, the MET is calculated. The recommended method for calculating the MET uses an official tool called METMaker (used in the same way as the lepton calibration tools). It is shown later that there are many issues with this tool, and the results are unreliable. As such, a simplified MET calculation that is *independent of METMaker* was also done, and shown to provide correct results.

The components needed for the final Jet Energy Scale result are:

1. Data MPF Response Curves in 2015, 2016, and 2017.
2. MC MPF Response Curves.
    - There are two different generators: Pythia and Sherpa. Comparing them covers the uncertainty in the choice of the MC generator in physics analyses.
    - There are two versions of each simulation. These versions model the pile-up conditions and detector status to be as close to specific yearly running conditions as possible. The versions are labeled mc16a (modeled as 2015 and 2016) and mc16d (modeled as 2017).
3. A full systematic uncertainty analysis with a breakdown of individual sources.

5.2 EMTopo Scale

5.2.1 Initial Results

Performing the steps outlined in the Analysis Steps section, results were derived using the recommended METMaker tool to calculate the MET. For each Z decay channel, the data from the three years were compared to check compatibility. These results are shown in figures 5.1 and 5.2. Detector and pile-up conditions change throughout the years, so it is not expected a priori that these curves should agree. Note that, for the electron decay channel, the results seem to agree much better than for the muon channel.

In a particular year, both decay channels should give identical response curves, as the underlying final state is Z+jet in both cases. If there is any disagreement between the two channels, it is likely due to a problem with the Z-boson reconstruction, as the jets are handled consistently in both cases. In order to check this assumption, the agreement between the two decay channels was checked for individual years. These comparisons are shown in figure 5.3. It is evident from the ratio plots that the points in the muon channel are systematically higher than for the electron channel.

After exhaustive testing, the problem was narrowed down to the calculation of the MET in the muon channel. These studies are described in the following pages. The problem with METMaker lies in the treatment of muons when using clusters. The fully calibrated lepton as provided by the muon group yields the best description of the muon. The contribution in the MET calculation arising from the clusters associated to the muon is removed, and replaced with the fully calibrated muon. In doing so, the pileup that is also present in the clusters is removed. Additionally, the method that is used to associate clusters to the muon is also sensitive to pileup. A combination of these two effects results in the incorrect handling of the cluster removal process. A solution to this problem in the form of an independent calculation is described in the next section.

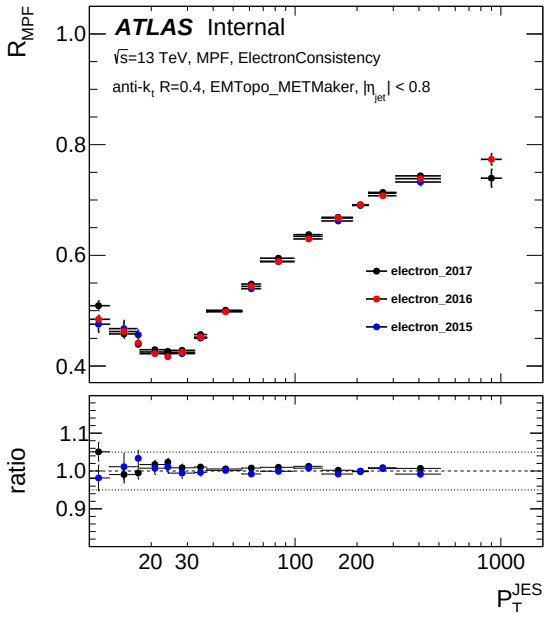

Figure 5.1: The response curves for 2015, 2016, and 2017 data for the $Z \to ee$ channel, using METMaker to construct the MET. The bottom panel shows the ratio of the curves with respect to the 2016 data.

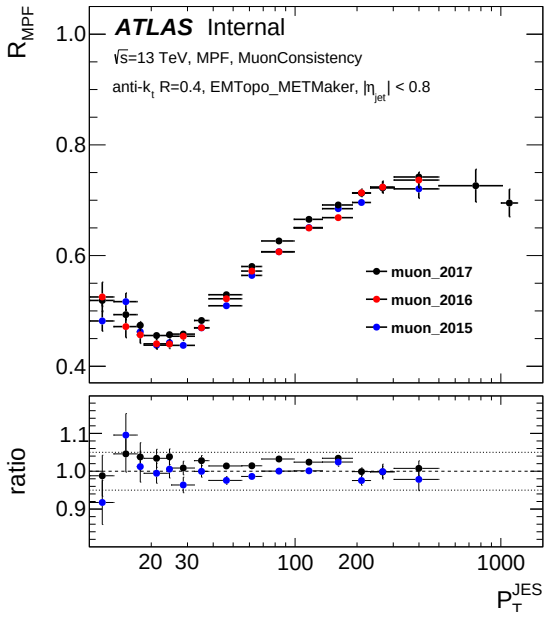

Figure 5.2: The response curves for 2015, 2016, and 2017 data for the $Z \to \mu\mu$ channel, using METMaker to construct the MET. The bottom panel shows the ratio of the curves with respect to the 2016 data.

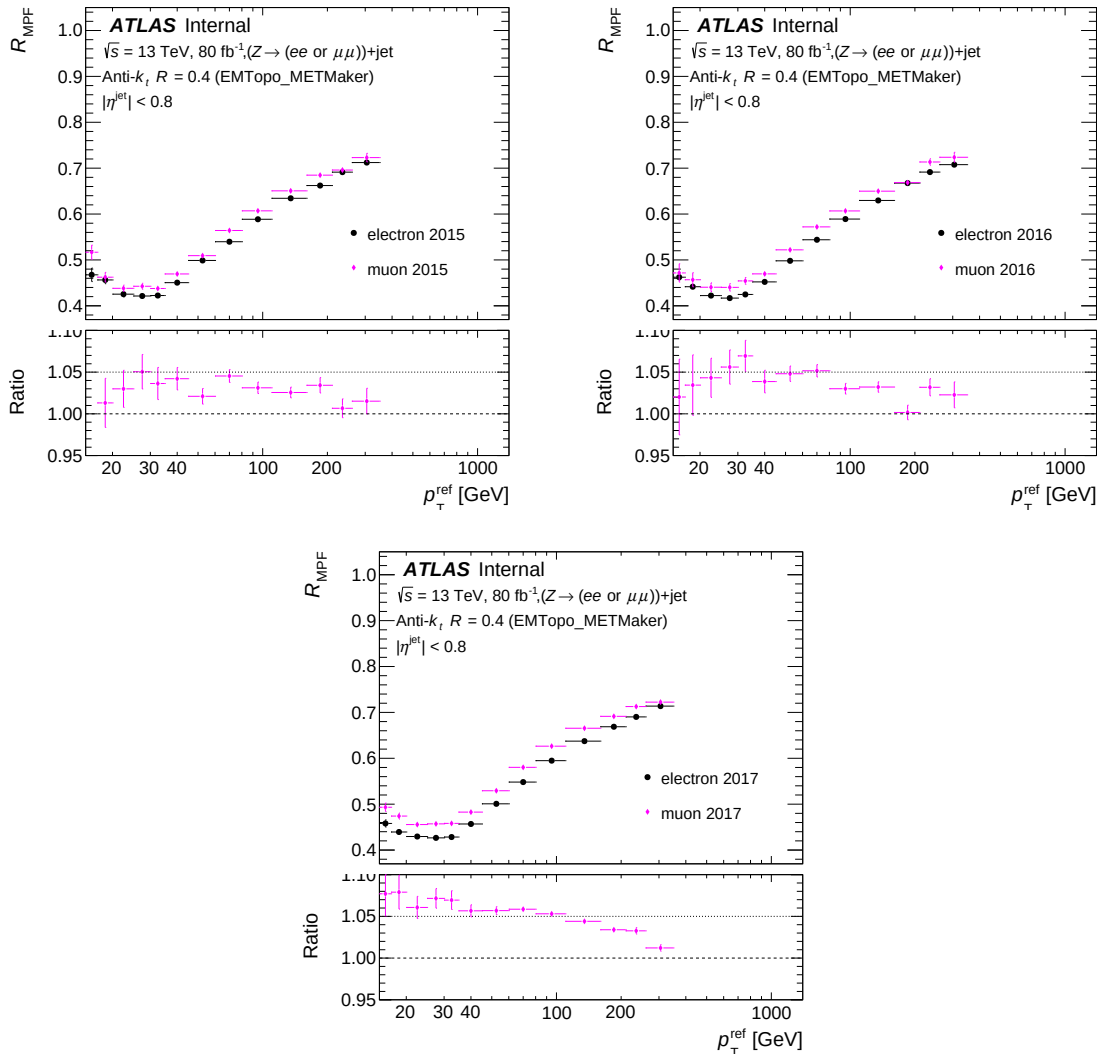

Figure 5.3: Overlaying the muon and electron response curves from 2015-2017 (top to bottom), as calculated using METMaker. There is a systematic shift up in the response of the muon channel.

5.2.2 Cluster MET

In ATLAS, experts provide software tools for completing common tasks, ensuring a standardized treatment of the data. However, the applicability of these tools needs to be tested by every physics analysis. In this case, there is clear evidence that the MET tool is causing problematic results. The MET is calculated here using a simple algorithm in order to cross-check the METMaker results. One can construct the MET as

$$\vec{E}_T^{miss} = -\sum \vec{p}_t^{\,clusters} \tag{5.2}$$

However, the algorithm can be improved in two ways. First, the fact that leptons are calibrated means taking the cluster readings is not sufficient to accurately describe the Z boson. Second, muons are minimum ionizing particles [39] and deposit very little energy in the calorimeter. If one used only the calorimeter clusters, the muon energies would be largely missed. Therefore, the calibrated leptons can be used instead of the clusters. The idea then is to take clusters associated with the leptons, remove them from the simple MET in equation 5.2, and add in the calibrated leptons. All clusters within a cone of 0.2 in $\eta - \phi$ space are treated as associated with the lepton:

$$\vec{p}_{EM}^{\,i} = \sum^{dR_i<0.2} \vec{p}_t^{\,clusters} \tag{5.3}$$

where i is the index corresponding to the lepton number (either 1 or 2). One can modify the simple MET calculation by replacing clusters with the associated calibrated leptons.

$$\vec{E}_T^{miss} = -\sum \vec{p}_t^{\,clusters} + \sum_i (\vec{p}_{EM}^{\,i} - \vec{P}_t^{\,l_i}) \tag{5.4}$$

where l_i is the i^{th} lepton. However, the removal of clusters within a radial separation of 0.2 of a lepton also removes pile-up, which should be kept so that the total vector sum of the pile-up is zero. This over-subtraction must be corrected. The average energy density of the event is taken and multiplied by the area of the clusters that were removed from the MET. This quantity is then projected along the direction of the lepton, which serves as an estimate of the pile-up removed, and is added back into the MET calculation.

$$\vec{E}_T^{miss} = -\sum \vec{p}_t^{\,clusters} + \sum_i (\vec{p}_{EM}^{\,i} - \vec{P}_t^{\,l_i} - \frac{\vec{P}_t^{\,l_i}}{\hat{P}_t^{\,l_i}} \cdot \rho \cdot \pi(0.2)^2) \tag{5.5}$$

This differs from METMaker in how the clusters are associated to the lepton (a cone of $r = 0.2$ instead of ghost association of clusters), and the treatment of pileup in associated clusters (ClusterMET adds back in an estimate of the removed pileup while METMaker does not). The MPF response curves using this method are shown in figure 5.4.

As can be seen from the figure, the response curves for muons and electrons are now in agreement. This behavior is expected due to the fact that the jet side of the event does not depend on the decay channel of the Z boson. This simple yet intuitively sound method of calculating the MET yields the correct response curves, while using METMaker does not. Therefore, the jet-energy-scale recommendations for ATLAS were provided using this alternative method, which is designated as *ClusterMET*. After exploring METMaker, it was found that the primary difference between the two methods is how clusters are associated with the leptons. It was shown that the METMaker and ClusterMET methods produce identical results for the electron decay channel, suggesting that the problem is with how calorimeter clusters are associated to muons, and the manner in which those clusters are treated. This information has been communicated to the groups that are responsible for muons and METMaker.

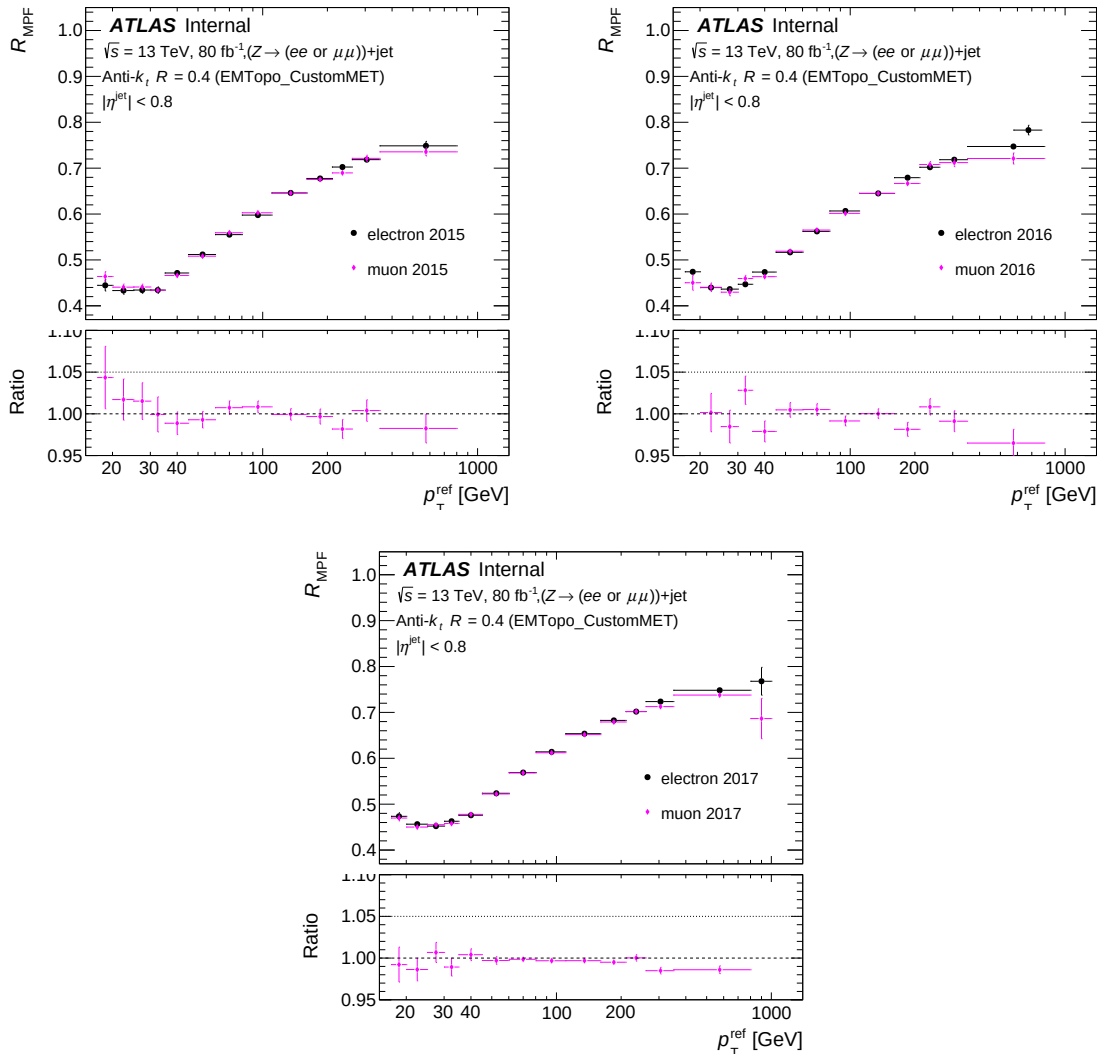

Figure 5.4: Overlaying the muon and electron response curves from 2015-2017 (top to bottom), calculated using the alternative ClusterMET method. The systematic shift in the ratio points from the METMaker results has disappeared, and the two channels now *do* agree with each other.

5.2.3 Final Results

Individual Years

After the resolution of the disagreement between channels, the ClusterMET method was accepted and approved for use in the official ATLAS recommendations for jet calibration. The next step in completing the recommendations is to derive the MC response curves, and the ratio of data to MC to provide the most accurate jet-energy calibration for ATLAS physics analyses.

The muon response curves for the individual years are shown in figure 5.5. A common trend appears here: the MC response curves are always 3-5 % higher than data. MC *does not* agree with data. The Pythia generator, in general, shows better performance and is the nominal choice. The behavior of the MC/Data ratio is noisy but stable between the years. This ratio is the in-situ correction needed to provide the correct jet-energy at ATLAS. The stability over years shown in figure 5.6, which shows a *double ratio*. The top panel shows two MC/Data ratios (with respect to the nominal Pythia response curves) from different years, and the bottom panel is the ratio of the ratios. The double ratios are quite consistent with each other.

The same plots, but for the electron decay channel, are shown in figures 5.7 (response curves) and 5.8 (double ratio plots). The conclusions here are similar to the muon case: the MC disagrees by about 3-5 %, Pythia shows better agreement than Sherpa, and the double ratios are consistent over the three years.

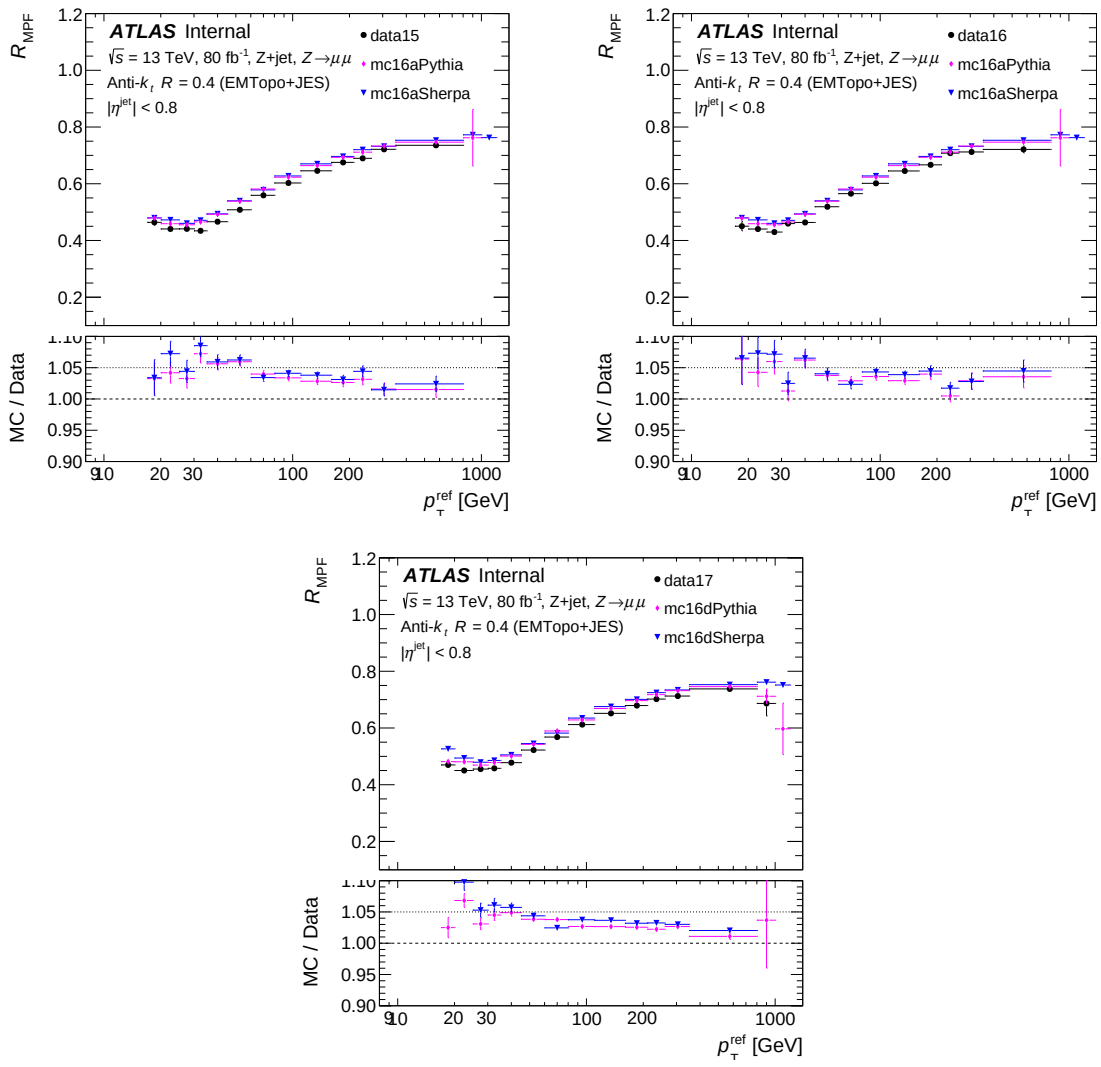

Figure 5.5: The data and MC (Pythia and Sherpa) response curves overlaid for 2015, 2016, and 2017 for the $Z \rightarrow \mu\mu$ channel. The bottom panel shows how well the MC and data agree. Generally, it is seen that the MC response curves are higher by about 5% at low p_t.

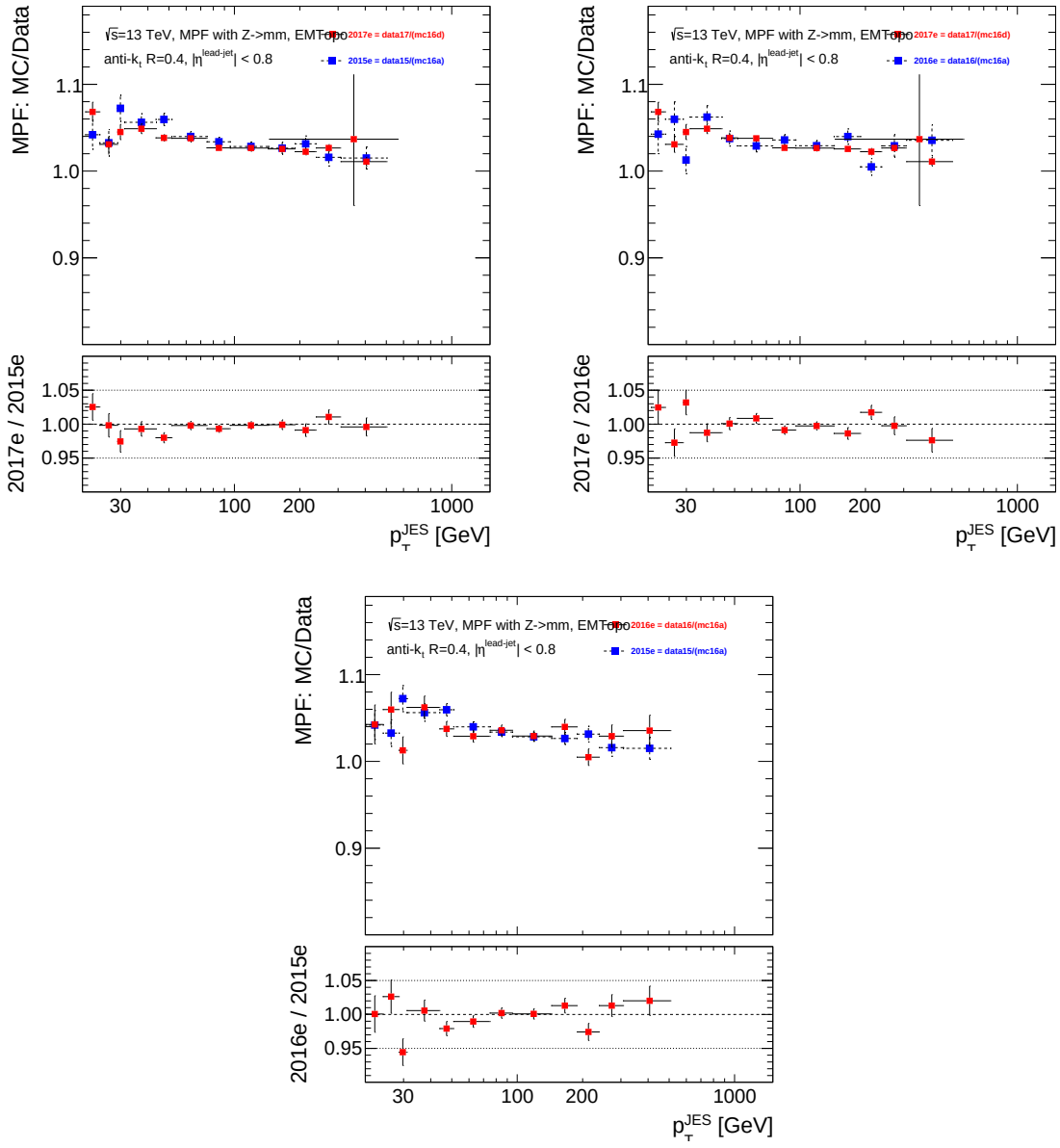

Figure 5.6: The double ratios for 2015, 2016, and 2017 for the $Z \to \mu\mu$ channel. The top panels are the ratios show in figure 5.5, and the bottom panels are the ratio of the ratios.

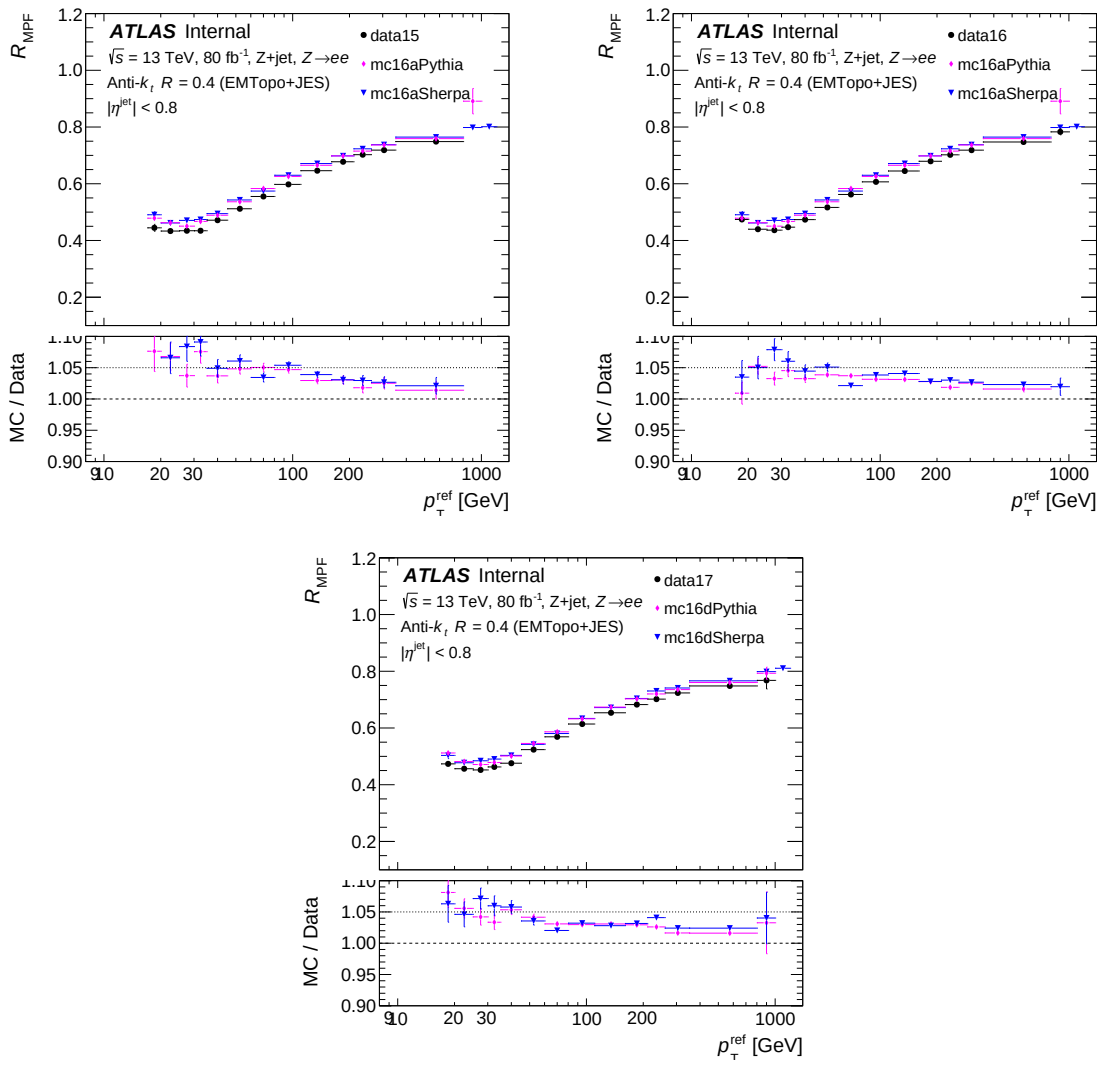

Figure 5.7: The data and MC (Pythia and Sherpa) response curves overlaid for 2015, 2016, and 2017 for the $Z \rightarrow ee$ channel. The bottom panel shows how well the MC and data agree. Generally, it is seen that the MC response curves are higher by about 5% at low p_t.

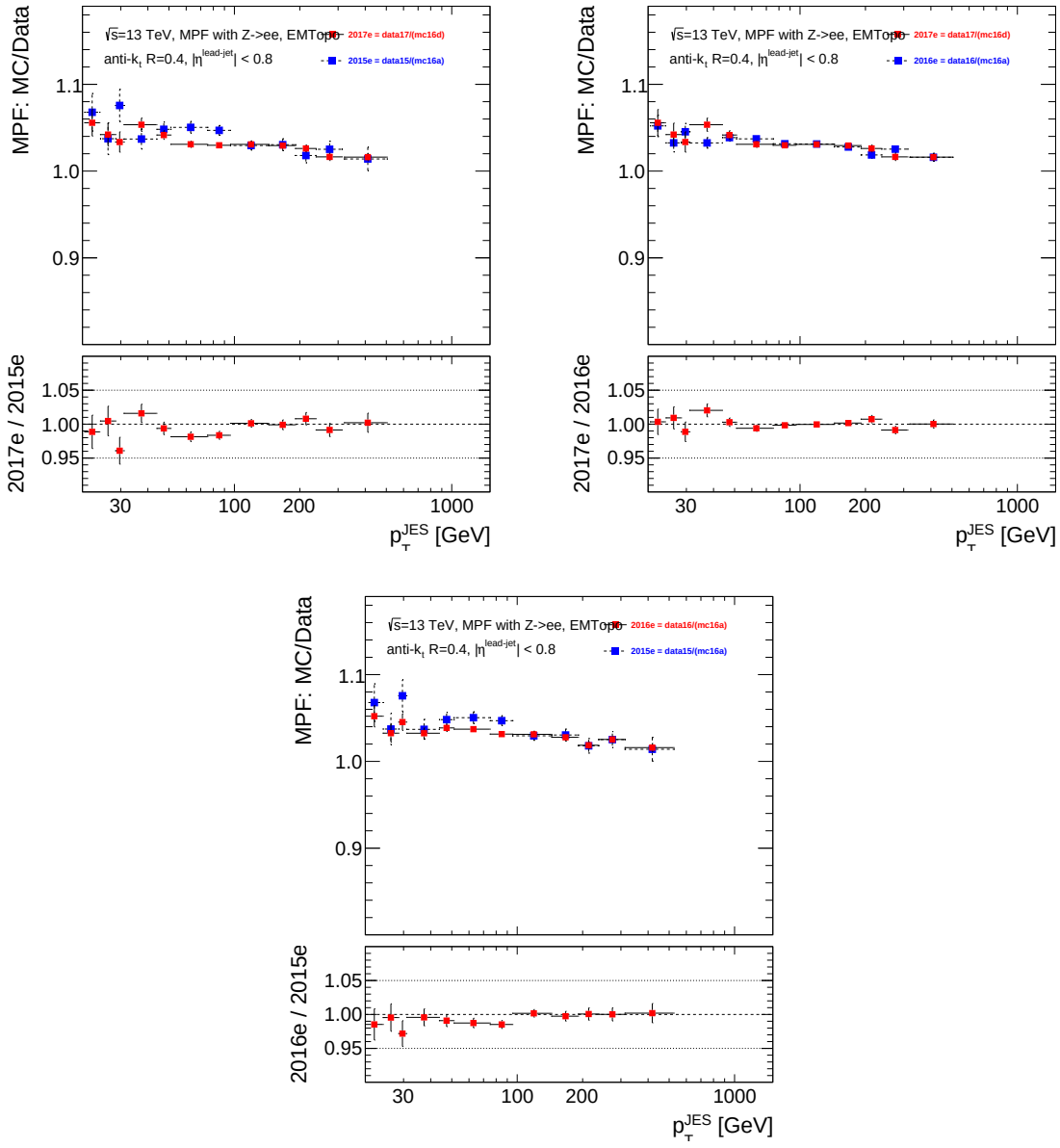

Figure 5.8: The double ratios for 2015, 2016, and 2017 for the $Z \rightarrow ee$ channel. The top panel is the ratios show in figure 5.7, and the bottom panel is the ratio of the ratios.

Combination

It has now been shown that the response measurements are consistent from year to year and in the two decay channels if the modified, simpler MET calculation is used. The JetETMiss group decided to combine the different years for each decay channel, resulting in one calibration for the $Z \to ee$ channel, and another for the $Z \to \mu\mu$ channel. In the past, the two channels were also combined and all systematic variations were applied to both, but they were kept separate for these recommendations. This is due to concerns about double peaked distributions in the combination when it comes to the systematic variations (varying the muon energy scale for example would affect the muon results, but not the electrons). The combined response curves for the $Z \to \mu\mu$ channel are shown in figure 5.9. The behavior is as expected, but with the increased statistics, the difference between Pythia and Sherpa at low-p_t is shown more clearly. The associated systematic uncertainty plots (which are called systematics for the results chapter) can be seen in figure 5.10, where both smoothed and unsmoothed plots are shown. The MC Modelling uncertainty dominates, with the Statistical uncertainty being the sub-leading contribution. Note that the significant spike at high-p_t is not important, as these results are combined with other studies done, and the Z+jet results are not used past around 500 GeV. The uncertainty settles to around 1% in the mid-p_t range, and the large low-p_t spike is due to the statistical fluctuation of the Sherpa results.

The same plots for the $Z \to ee$ channel are shown in figures 5.11 (response curves) and 5.12 (systematics). Similar behavior to the muon case is seen with a few marked differences. Most clear is the lack of a significant rise in the uncertainty at low-p_t. This difference can be traced to a statistical fluctuation in the Sherpa MC results at low-p_t in the muon channel. The second difference is that the electron energy scale uncertainty is significant, whereas the muon energy scale uncertainty is not. It is important to note this, as the EGamma energy scale applies to photons as well, and ends up being one of the leading uncertainties when the combination with the γ + jet channel is done.

As discussed previously, the inclusion of the entire hadronic recoil of the system introduces possibilities of pile-up effects. However, due to the ϕ symmetry of the pileup and the (near) hermetic geometry of ATLAS, these effects are expected to cancel on average and to result in a pile-up independent calibration. This is shown in figures 5.13 and 5.14, which plot the response vs μ (average number of interactions per beam-bunch crossing). Little to no dependence is seen, thus proving that the MPF method is not sensitive to pile-up. It is important to note that there is *no pile-up correction applied* (aside from the small effect when matching leptons to the calorimeter clusters). This insensitivity to pile-up is an inherent strength of the MPF. However, a small pile-up dependence is starting to be visible

in figure 5.14, and is something to monitor in the future.

These results were provided for combination with other channels that cover different p_t regions, and are currently being used in the official ATLAS JES recommendations, providing every analysis at ATLAS with increased precision. The combination procedure combines the different in-situ JES methods to cover a large p_t range. The Z+jet results shown here are combined with $\gamma + jet$ results (similar studies, but the event topology studied looks at photons as the reference object instead of a Z boson) and the multijet balance (MJB) balance results. The MJB looks at events where one large-p_t jet is balanced by many small-p_t jets. The in-situ calibration from Z and γ channels is applied to the smaller-energy jets, and then momentum balance gives a calibration for the larger jet. By combining these three methods, a large p_t range can be covered by the calibration. The weighting of the methods is shown in figure 5.15. The combined calibration that is provided for analysis is shown in figure 5.16, with the associated uncertainty shown in figure 5.17. The "Absolute *in-situ* JES" component is derived in part from the work shown in this thesis. At low-p_t, the Z+Jet results are used exclusively, for which the uncertainty is on the order of 5%. A statistical method involving splines is used to reduce the uncertainty at low-p_t by extrapolating the effects of higher-p_t regions.

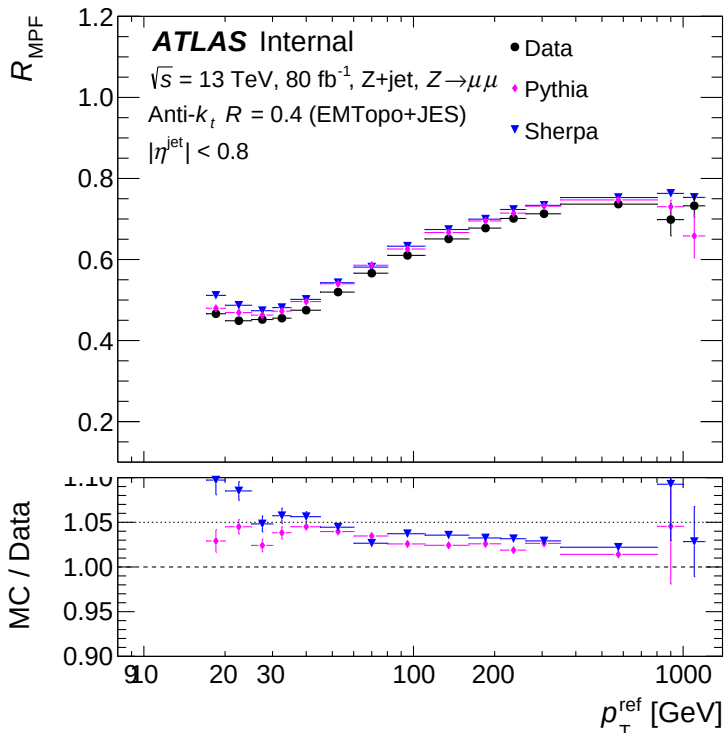

Figure 5.9: The data and MC (Pythia and Sherpa) response curves with all three years combined into one curve for the $Z \to \mu\mu$ channel. The top panel shows the response curves, and the bottom panel shows the ratio between data and MC.

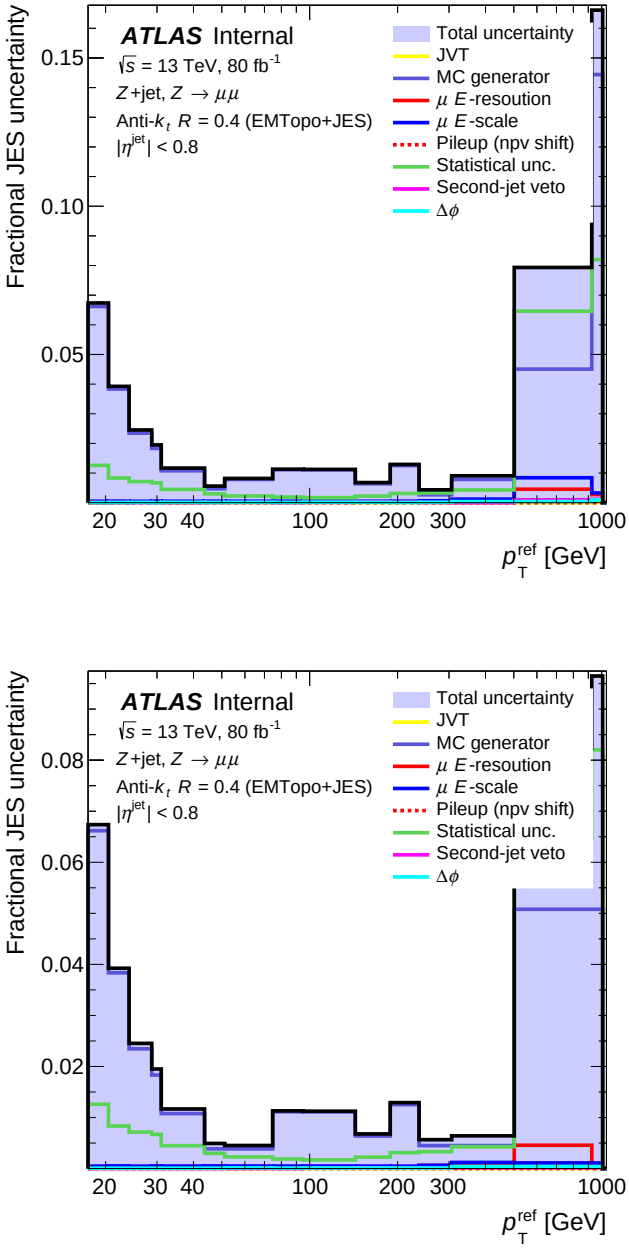

Figure 5.10: The full systematic analysis for the combined muon channel. On the top is the original systematic plot, and the bottom is after rebinning with 2σ significance smoothing is applied. Note that the large uncertainty at high-p_t is not important, as these results are not used in that region (see figure 5.15). The MC Modelling uncertainty dominates, with the statistical uncertainty being the next largest.

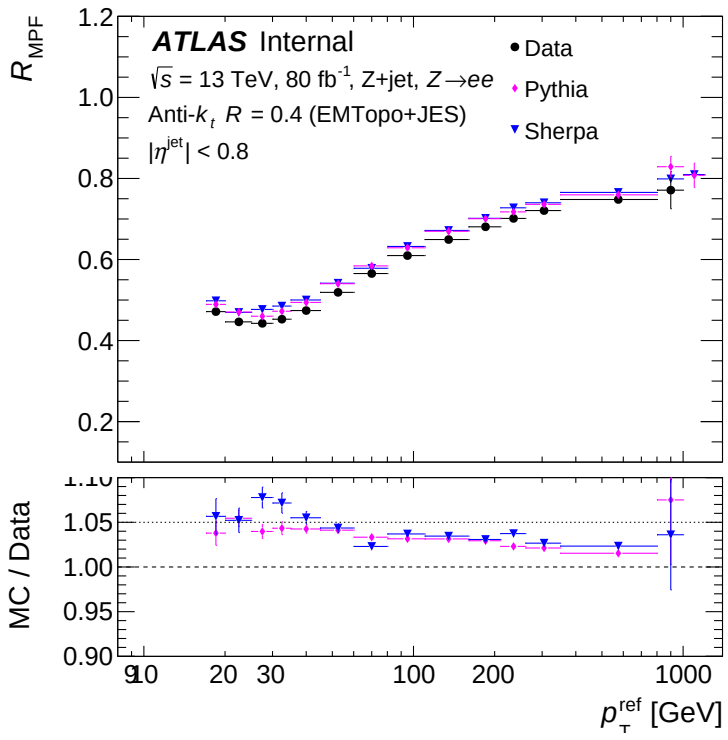

Figure 5.11: The data and MC (Pythia and Sherpa) response curves with all three years combined into one curve for the $Z \to ee$ channel. The top panel shows the response curves, and the bottom panel shows the ratio between data and MC.

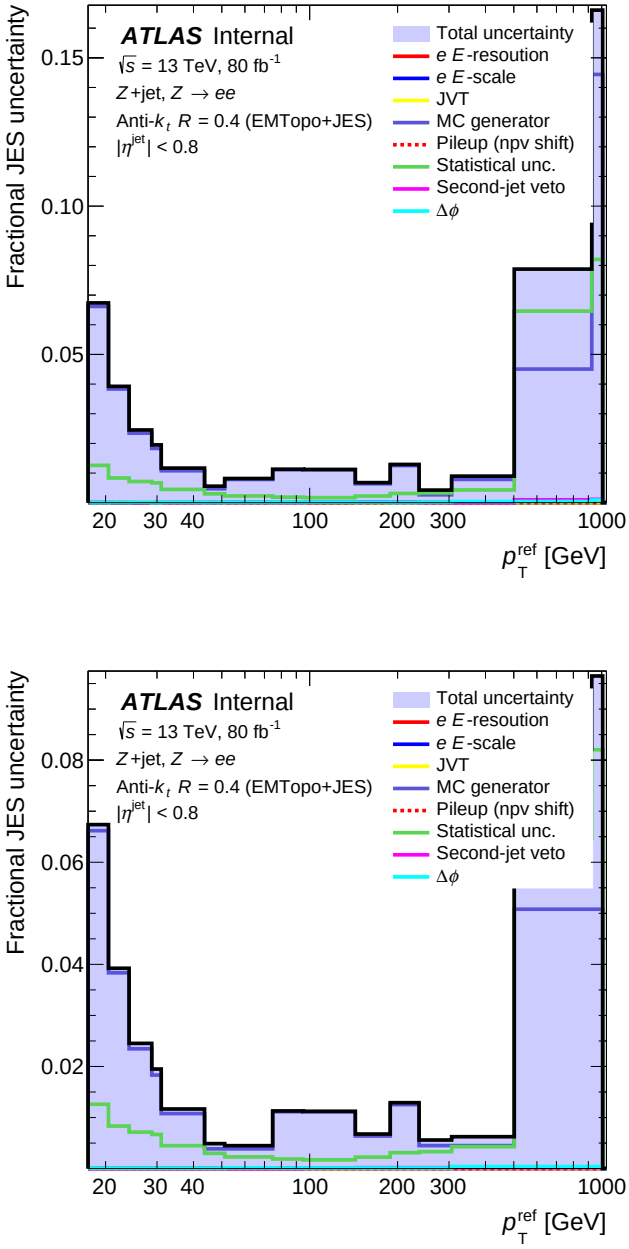

Figure 5.12: The full systematic analysis for the combined electron channel. On the top is the original systematic plot, and the bottom is after rebinning with 2σ significance smoothing is applied. Note that the large uncertainty at high-p_t is not important, as these results are not used in that region (see figure 5.15). The MC Modelling uncertainty dominates, with the statistical uncertainty being the next largest.

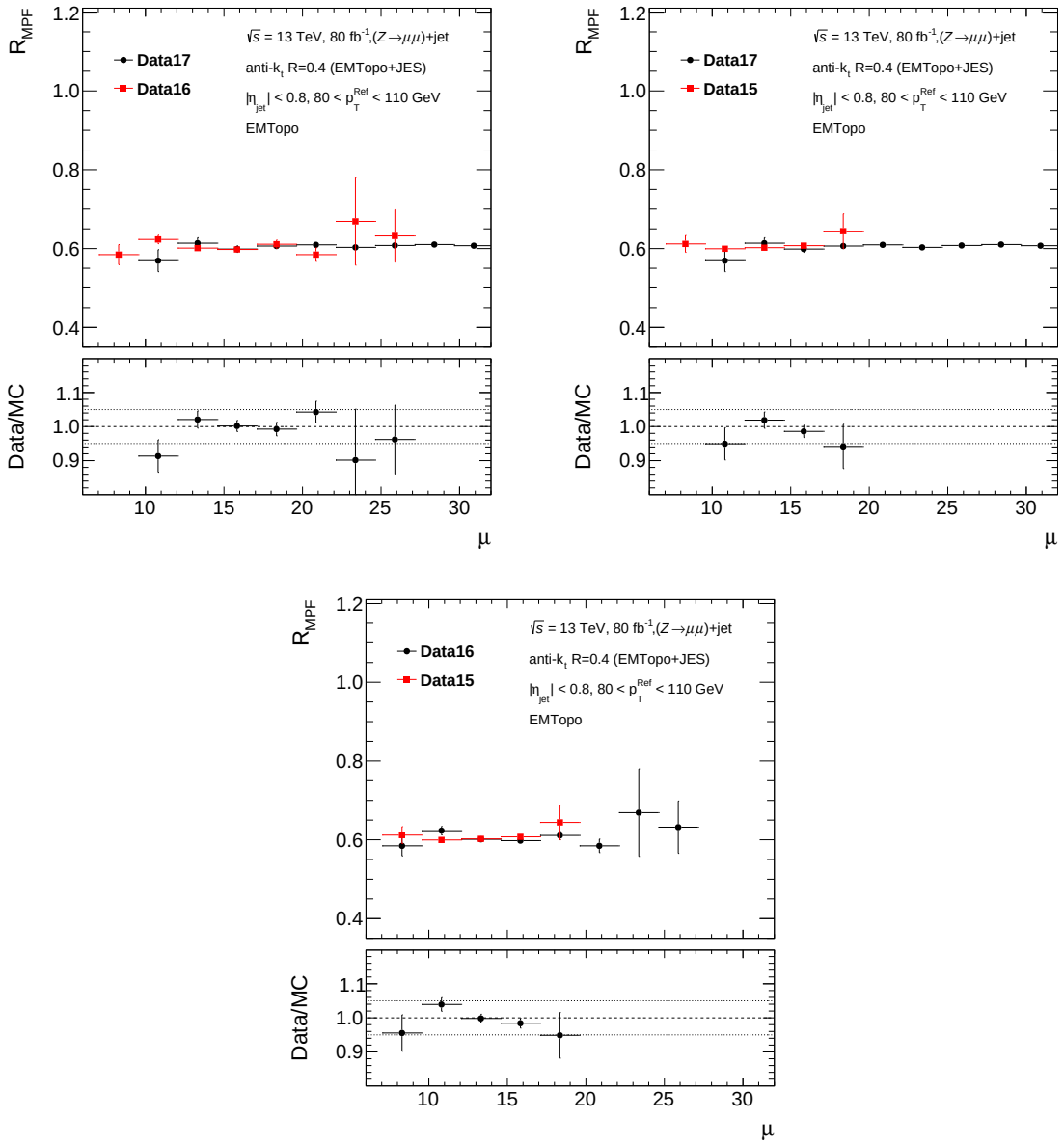

Figure 5.13: The response vs average number of interactions per beam-bunch crossing for the $Z \to \mu\mu$ decay channel for the three different years. The data are shown in one of the lower p_t bins where pile-up is likely to have a larger effect. Little to no dependence on pile-up is seen here, showing that the MPF technique is indeed not sensitive to even significant levels of pile-up.

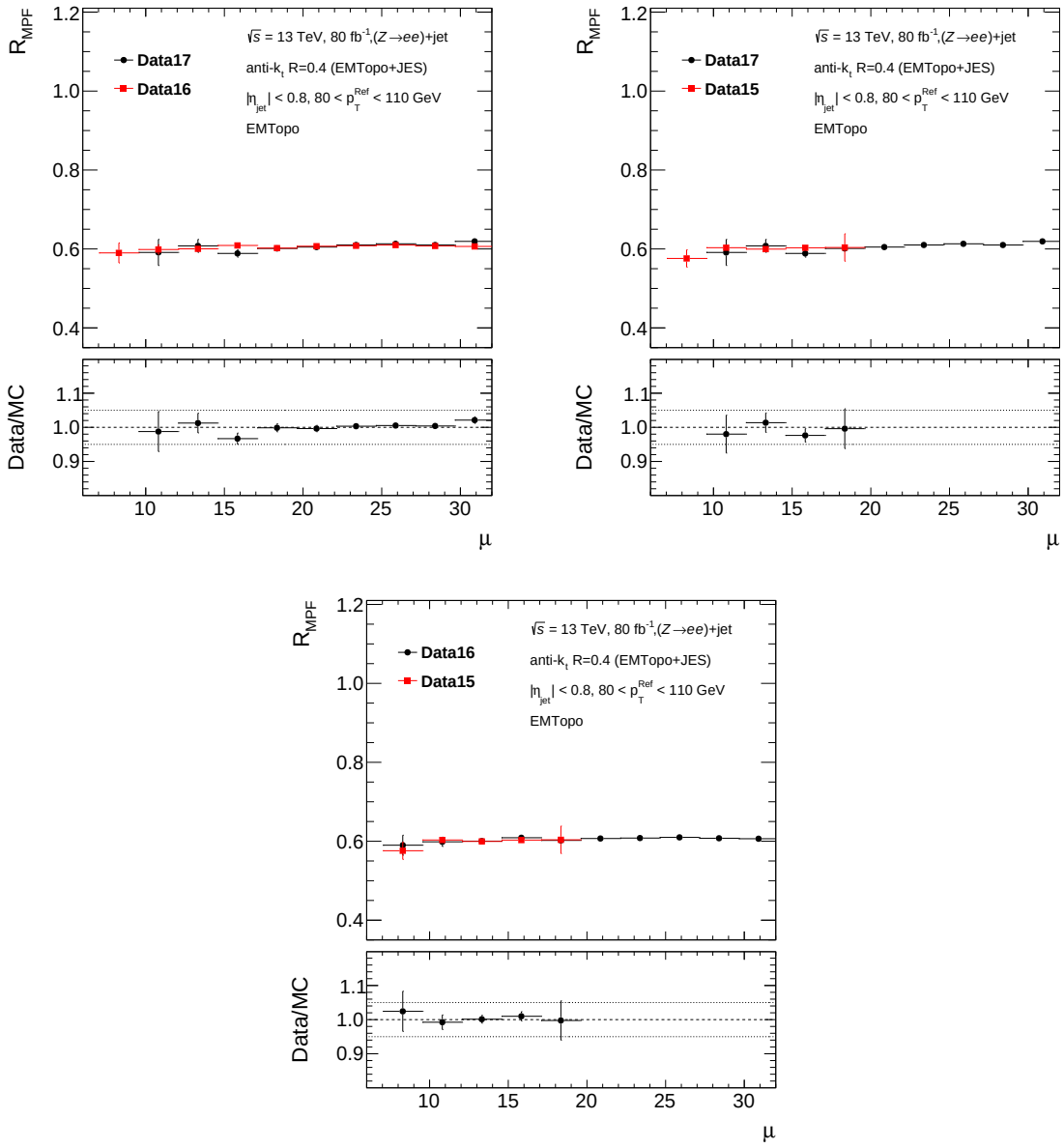

Figure 5.14: The response vs average number of interactions per beam-bunch crossing for the $Z \rightarrow ee$ decay channel for the three different years. The data are shown in one of the lower p_t bins where pile-up is likely to have a larger effect. Little to no dependence on pile-up is seen here, showing that the MPF technique is indeed not sensitive to even significant levels of pile-up.

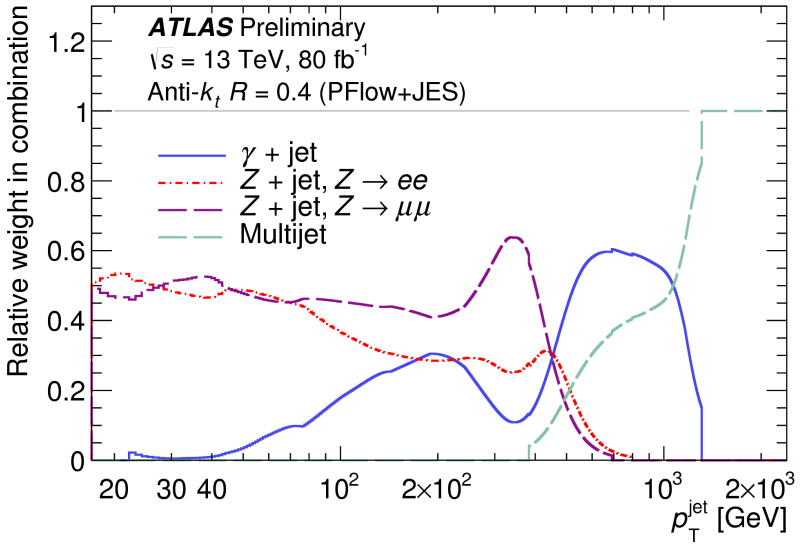

Figure 5.15: The weighting of the different in-situ calibration methods in the combination. The results here are shown for PFlow, but EMTopo has a similar distribution. The Z+jet results are used up to about 500 GeV, after which the other two channels take over. The two Z decay channels are weighted by their uncertainties. Fluctuation in the uncertainty of a channel can lead to unequal weighting.

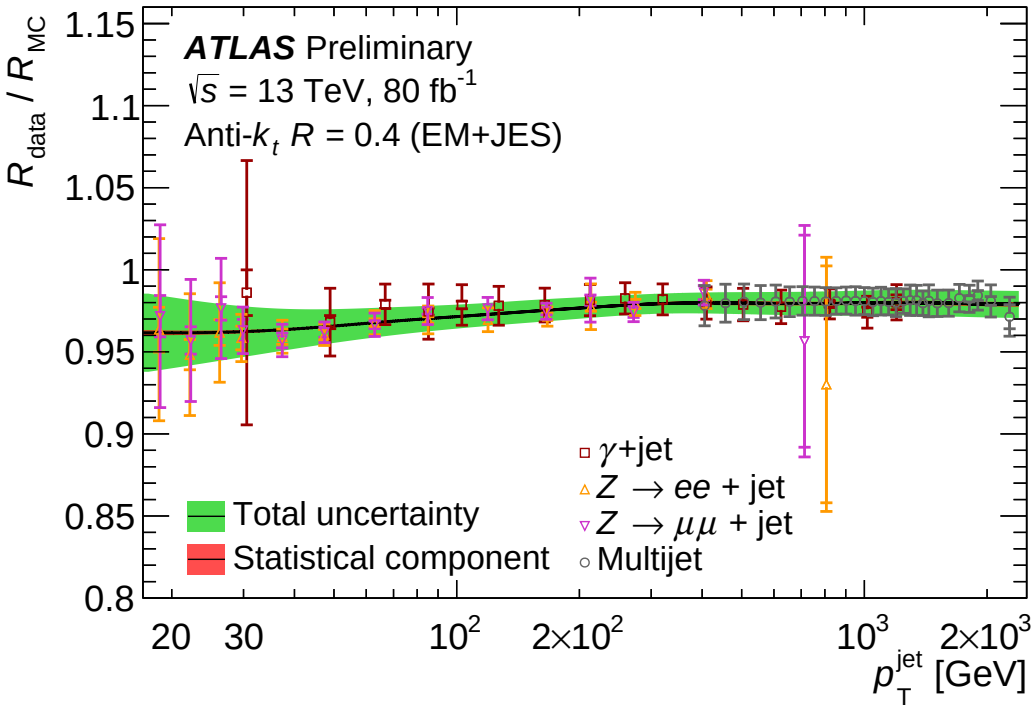

Figure 5.16: The final data/MC calibration for PFlow jets that is provided to the rest of the ATLAS collaboration after the Z+jet results of this thesis are combined with the γ+jet channel and the multi-jet balance results from other studies.

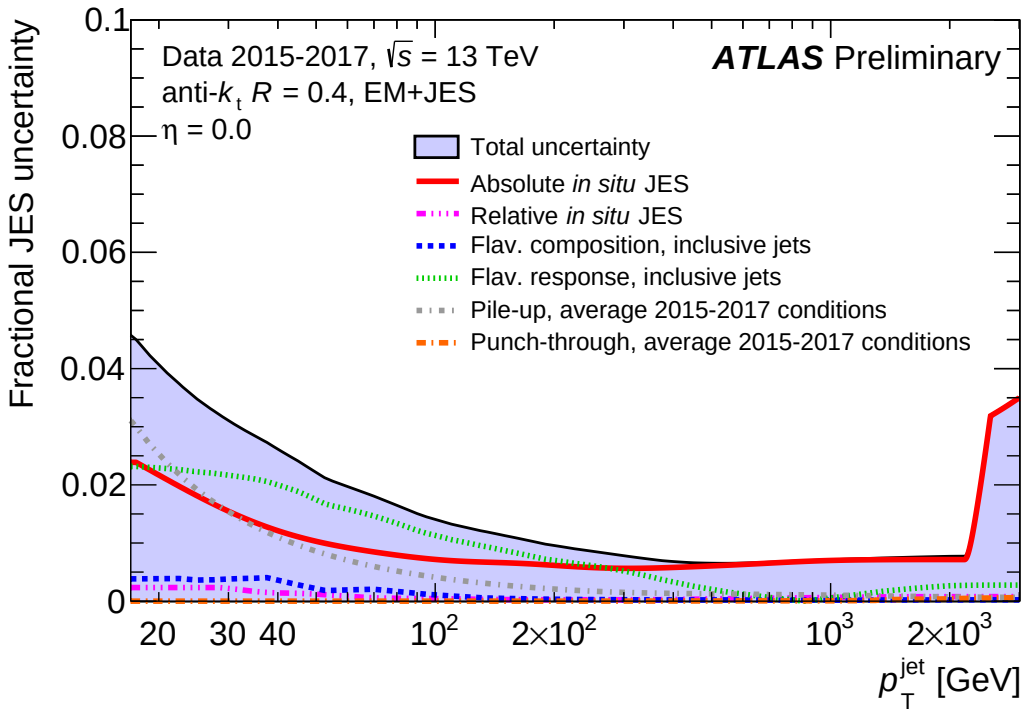

Figure 5.17: The uncertainty on the combined JES for EMTopo jets that is provided to the rest of the ATLAS collaboration after the Z+jet results of this thesis are combined with the γ+jet channel and the multi-jet balance results from other studies. The large spike in the uncertainty at around 2.4 TeV comes from the single-particle simulations response studies [8].

5.3 Particle Flow Scale

5.3.1 Initial Results

Recall that the PFlow jet collection uses PFlow (particle flow) objects as inputs to the jet reconstruction algorithm. PFlow objects are combinations of tracks and calorimeter clusters, which is done due to tracks having better energy resolution at low-p_t.

Performing the steps outlined in the Analysis Steps section, results were derived using the recommended METMaker tool to calculate the MET. Motivated by what was seen for the EMTopo case, preliminary checks were done on the data response curves to gauge compatibility between the electron and muon channels in individual years. The results of these studies are shown in figure 5.18. The behavior differs from what was seen for the EMTopo case. The two decay channels are indeed different, but not by a constant shift. Instead, the difference is characterized by a slope in the ratio panel, which increases with year. The response in the muon channel is above the electron channel at low p_t, but below it over most of the p_t range. The response curves should be identical and independent of the method used to reconstruct the Z.

An alternative calculation of the MET for PFlow was developed, but it was not completed quickly enough to make the official recommendations. It is nevertheless described in this thesis.

5.3.2 PFO PFlow

An alternative MET calculation similar to ClusterMET (equation 5.5) was developed for the PFlow scale. PFlow calculations use PFlow objects (PFOs). Neutral PFOs use only the calorimeter information, but charged PFOs combine information from the tracker and the calorimeter to get a better measurement.

For the neutral PFOs, one sums over all the PFO objects, excluding those that are within a cone of 0.2 in $\eta - \phi$ space around a lepton. Therefore, the first component of the calculation is

$$(E_T^{miss})_{nPFO} = -\sum^{dR_l \geq 0.2} nPFO_i \tag{5.6}$$

where dR_l is the radial distance between a PFO and the lepton nearest it.

For the charged PFO, the first major difference is that they come with summation weights. These weights are calculated using the distance of a cluster to the track. The clusters that are closer are more likely to contain energy from the particle, and so are weighted more than clusters that are further away [27]. The second difference is that a vertex cut is imposed

to exclude pile-up PFOs in a manner consistent with the pile-up density calculation. It is required that charged PFO tracks be within 3 mm of the hard scatter vertex (which can be calculated as $|z_0 sin\theta|$). Thus, the charged PFO component of the MET calculation can be written as

$$(E_T^{miss})_{cPFO} = -\sum^{(dR_l \geq 0.2)\ \&\&\ (|z_0 \sin\theta| < 3mm)} cPFO_i \cdot w_i \tag{5.7}$$

Because the vertex cut is included, the standard PFlow pile-up density for the event can be used. This density needs to be extrapolated into the lepton-exclusion cones to compensate for the pile-up activity that is removed.

The total PFlow MET can be written as

$$E_T^{miss} = (E_T^{miss})_{nPFO} + (E_T^{miss})_{cPFO} - \vec{p_t^{l_1}} - \vec{p_t^{l_2}} - \rho_{PFlow} \cdot \pi(0.2)^2 \cdot (\hat{p_t^{l_1}} + \hat{p_t^{l_2}}) \tag{5.8}$$

The first two terms are the sum over the neutral and charged PFOs, but with an exclusion cone around the leptons. The next two terms add in the momentum of the leptons. However, by removing the PFOs around the lepton, the pile-up contributions have been removed as well. The final term takes the average energy density in the event as calculated using PFOs, and adds back in a cone of pile-up on top of the leptons.

Results from this method are shown in figure 5.19. Using this custom PFO based PFlow calculation solves the problems seen earlier when using METMaker. However, these results were not produced in time to be validated and, unfortunately, were not included in the official recommendations.

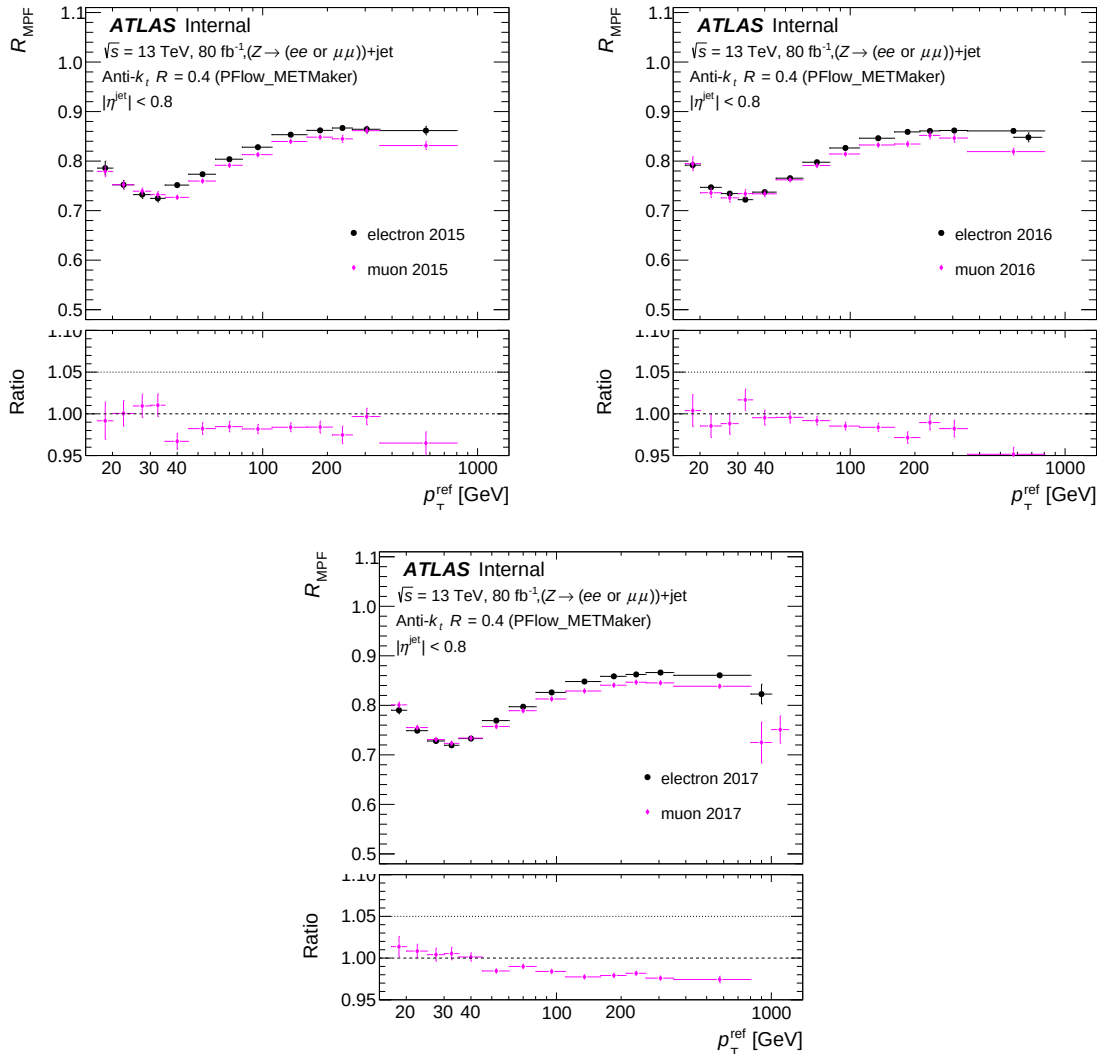

Figure 5.18: Overlaying the muon and electron response curves from 2015-2017, calculated using METMaker. There is a shape difference between the two channels. There is no reason to expect this difference, and this hints at something being incorrect.

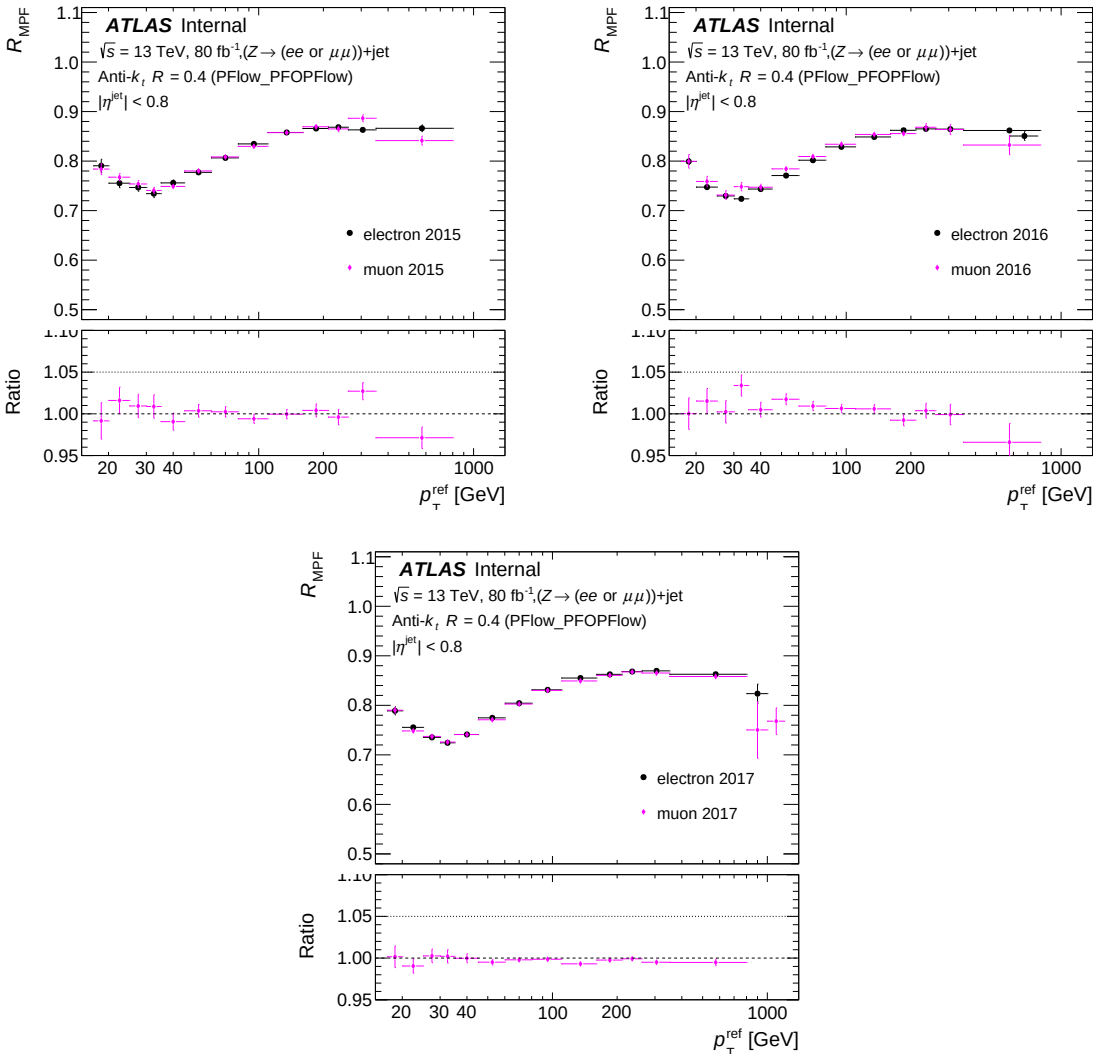

Figure 5.19: Overlaying the muon and electron response curves from 2015-2017 (top to bottom), as calculated by the custom PFOPFlow method for calculating the MET. The ratio plots show that all discrepancies have been solved and the two decay channels are in excellent agreement.

5.3.3 Final Results

Individual Years

The disagreement between the electron and muon decay channels of the Z-boson for PFlow when METMaker was used was considered to be small enough that the results were used as input to the official ATLAS recommendations. The PFOPFlow results as derived in the previous section are more reliable, but the studies were incomplete at the time of the combination. As for the EMTopo case, the next step in completing the recommendations is to derive the MC response curves and generate the MC/Data ratios.

The muon response curves for the individual years are shown in figure 5.20. The behavior is the same as for the EMTopo plots in that the MC disagrees with Data by around 3-5 %. Unlike EMTopo, however, the MC/Data ratio does not appear to be stable between years. This discrepancy is shown in figure 5.21, which shows the double ratio plots (similar to the corresponding EMTopo plots). The first two plots show comparisons of the MC/Data ratios for 2017 with 2015 and 2016 respectively, and the final plot compares 2015/16. The last plot shows excellent agreement, while the first two show a systematic shift in the double ratio, which indicates a difference in the 2017 calibration. This is likely due to the previously shown issues with the METMaker results.

The same plots for the electron decay channel are shown in figures 5.22 (response curves) and 5.23 (double ratio plots). For these plots, better agreement in the double ratio plots is seen, and everything is well behaved. MC still disagrees with Data by around 3-5%, Pythia is in better agreement than Sherpa, and the MC/Data ratios match across the years. This consistency hints that the problems seen earlier originate from the treatment of muons in the 2017 data.

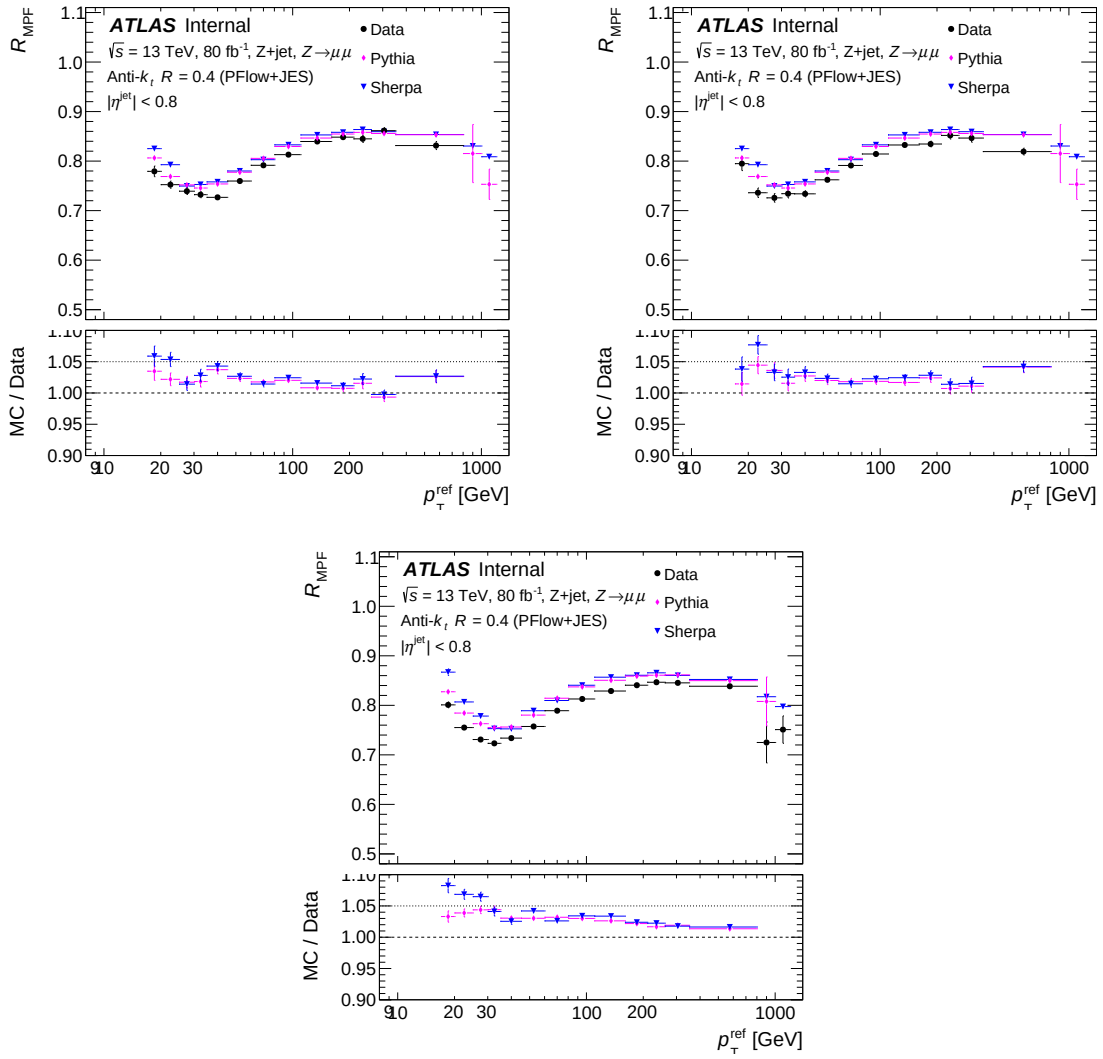

Figure 5.20: The data and MC (Pythia and Sherpa) response curves overlaid for 2015, 2016, and 2017 for the $Z \rightarrow \mu\mu$ channel. The bottom panels show how well the MC and data agree. Generally, it is seen that the MC response curves are higher by about 5% at low p_t, and 1-2% elsewhere.

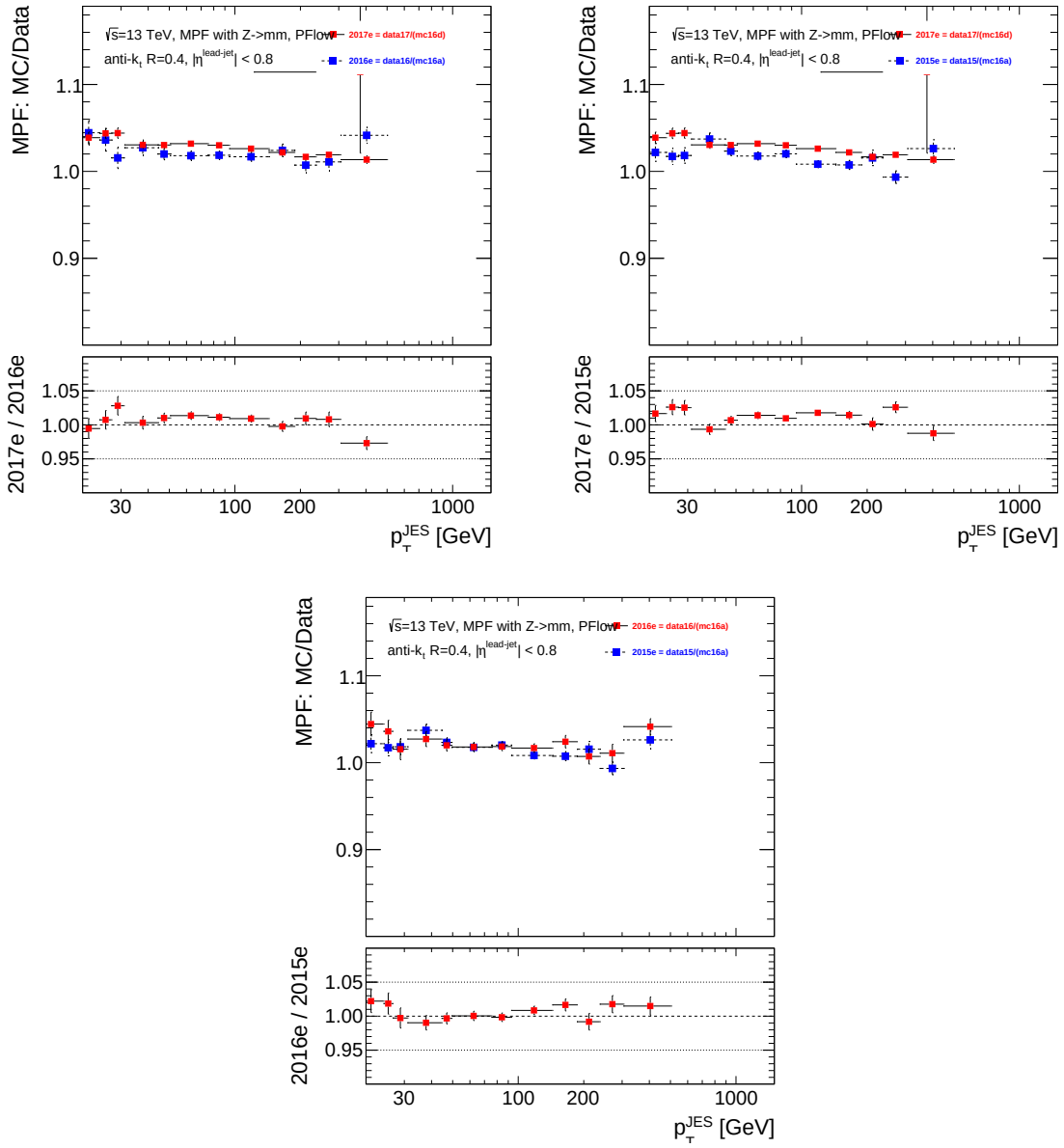

Figure 5.21: The double ratios for 2015, 2016, and 2017 for the $Z \to \mu\mu$ channel. The top panels show the ratios from figure 5.20, and the bottom panel is the ratio of the ratios. The first two plots show inconsistency, while the last plot agrees. This suggests that there is a problem in the 2017 results.

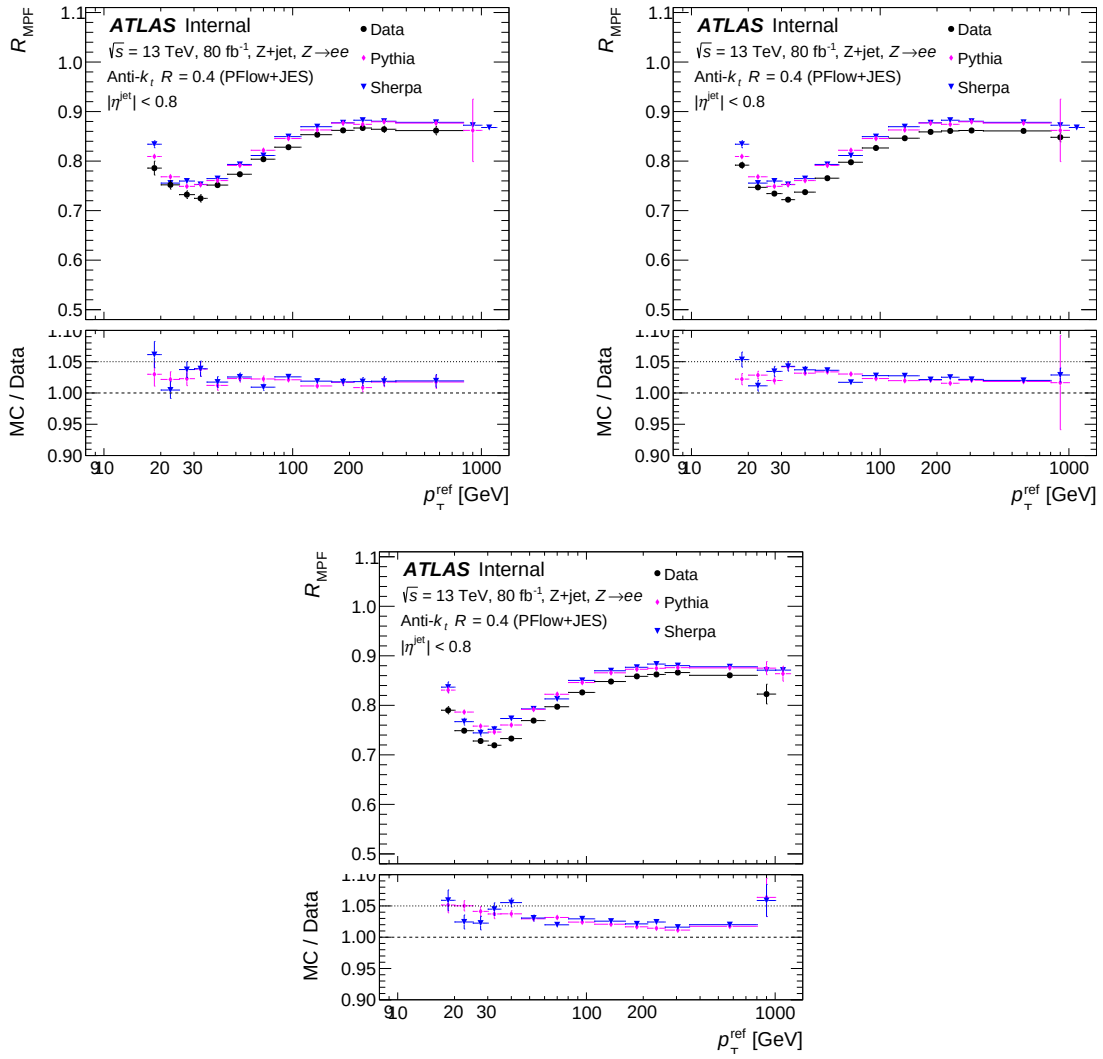

Figure 5.22: The data and MC (Pythia and Sherpa) response curves overlaid for 2015, 2016, and 2017 for the $Z \rightarrow ee$ channel. The bottom panels show how well the MC and data agree. Generally, it is seen that the MC response curves are higher by about 5% at low p_t, and 1-2% elsewhere.

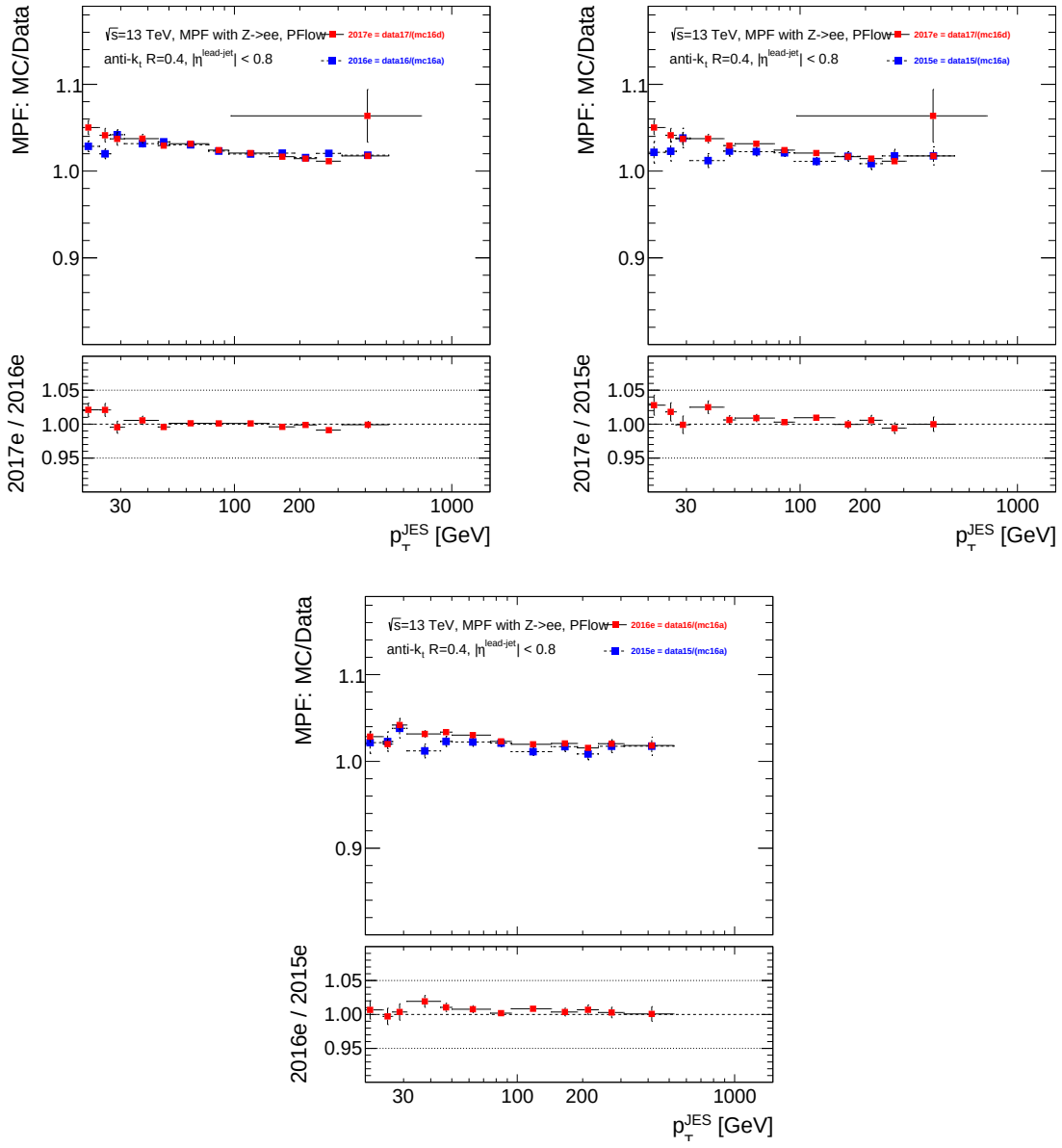

Figure 5.23: The double ratios for 2015, 2016, and 2017 for the $Z \rightarrow ee$ channel. The top panels show the ratios from figure 5.22, and the bottom panels are the ratio of the ratios. These are in agreement.

Combination

The inconsistencies in the muon decay channel are considered small enough that the different years for each decay channel are combined. The combined response curves for the $Z \rightarrow \mu\mu$ channel are shown in figure 5.24. The behavior is as expected with the same low-p_t disagreement between Pythia and Sherpa, with Pythia agreeing better with the data. The associated systematics plots are shown in figure 5.25, where both smoothed and unsmoothed systematic results are shown. As in the EMTopo case, the MC Modelling uncertainty dominates, with the Statistical uncertainty being the second largest. Note that the systematics are sub-1% over the majority of the range. Also note that the response values are higher for PFlow than for the EMTopo case. This is because tracks are used, which provide a better measure of particle energy at low-p_t.

The same plots for the $Z \rightarrow ee$ channel are shown in figures 5.26 (response curves) and 5.27 (systematics). The trends are similar to the EMTopo case. The MC Modelling uncertainty is the dominant uncertainty, with the Statistical uncertainty being the second largest in some regions of p_t. Note that the uncertainty on the EGamma Energy Scale is quite significant at higher p_t. The uncertainty here is also sub-1% for a large range.

For PFlow, MPF is still expected to be insensitive to pile-up due to the pile-up effects canceling on average over a large number of events. This is shown in figures 5.28 and 5.29, verifying the pile-up insensitivity of the MPF method once more.

These results were provided for combination with other channels and are currently being used in the official ATLAS JES recommendations, providing every analysis at ATLAS with increased precision and decreased uncertainty.

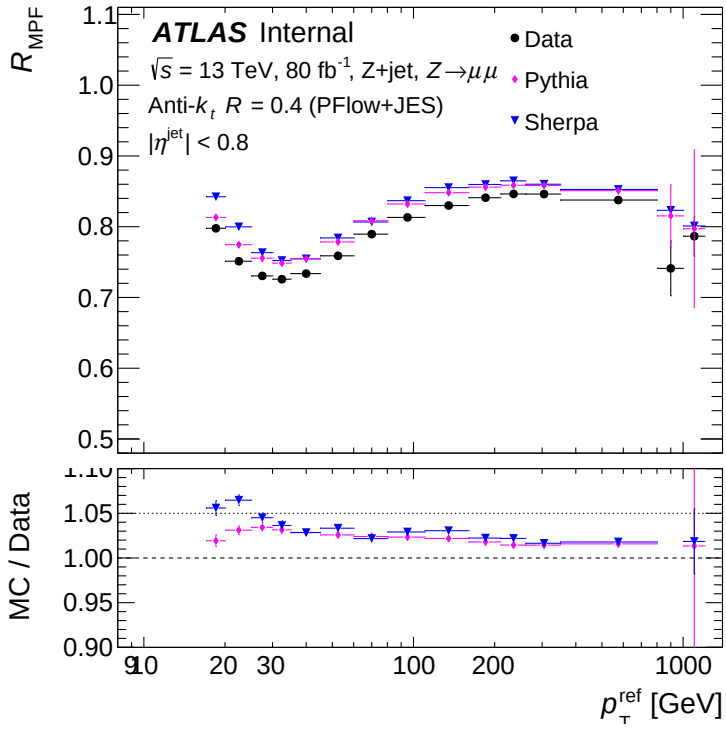

Figure 5.24: The data and MC (Pythia and Sherpa) response curves with all three years combined into one curve for the $Z \to \mu\mu$ channel. The top panel shows the response curves, and the bottom panel the ratio between data and MC.

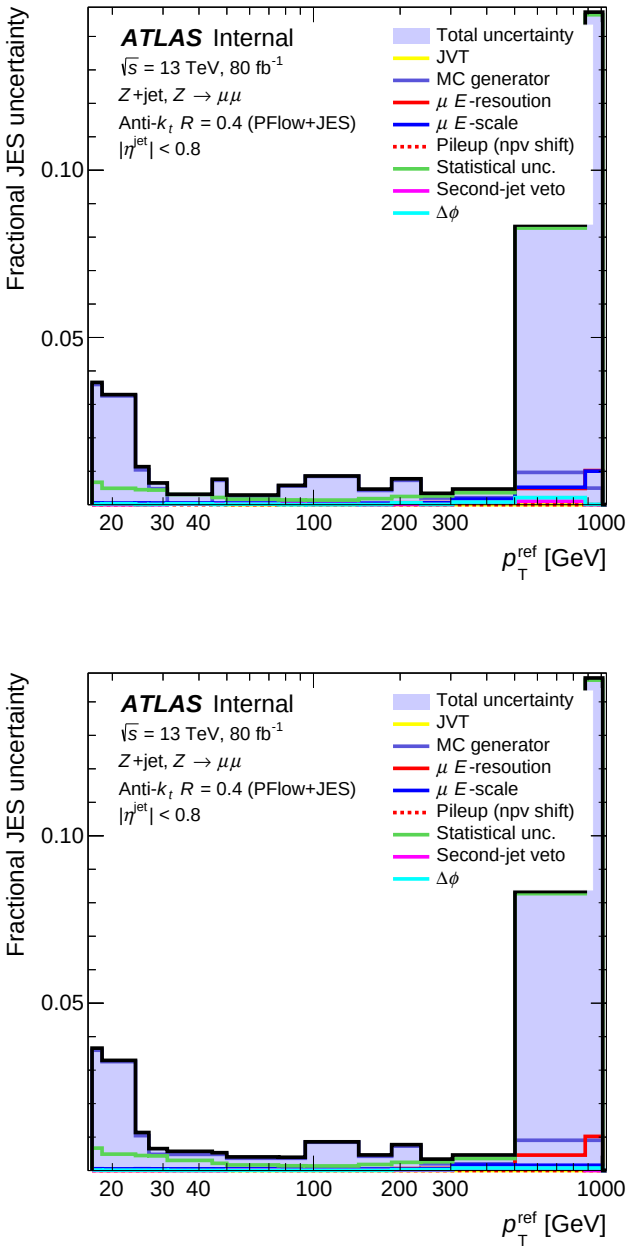

Figure 5.25: The full systematic analysis for the combined muon channel. On the top is the original systematic plot, and the bottom is after rebinning with 2σ significance is applied. Note that the large uncertainty at high-p_t is not important, as these results are not used in that region (see figure 5.15). The MC Modelling uncertainty dominates, with the statistical uncertainty being the next largest.

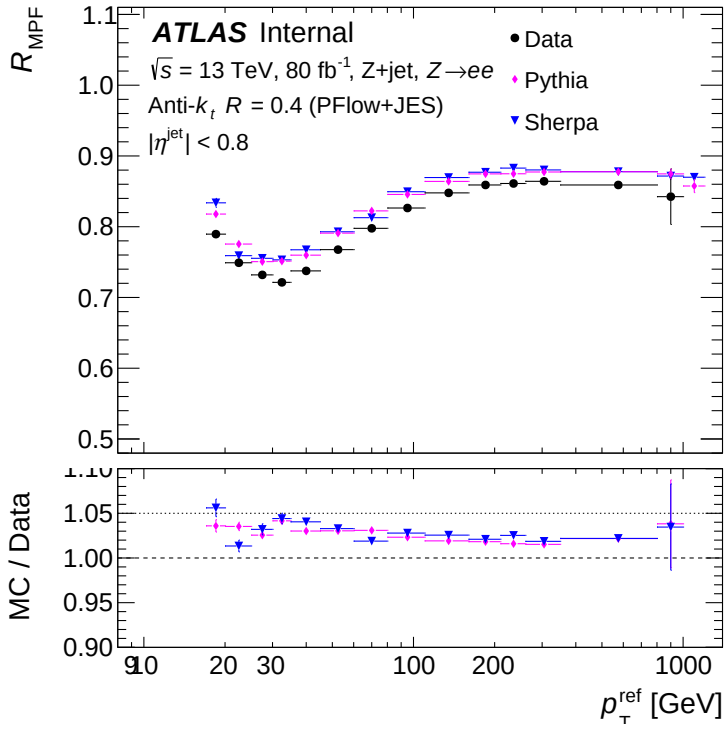

Figure 5.26: The data and MC (Pythia and Sherpa) response curves with all three years combined into one curve for the $Z \to ee$ channel. The top panel shows the response curves, and the bottom panel the ratio between data and MC.

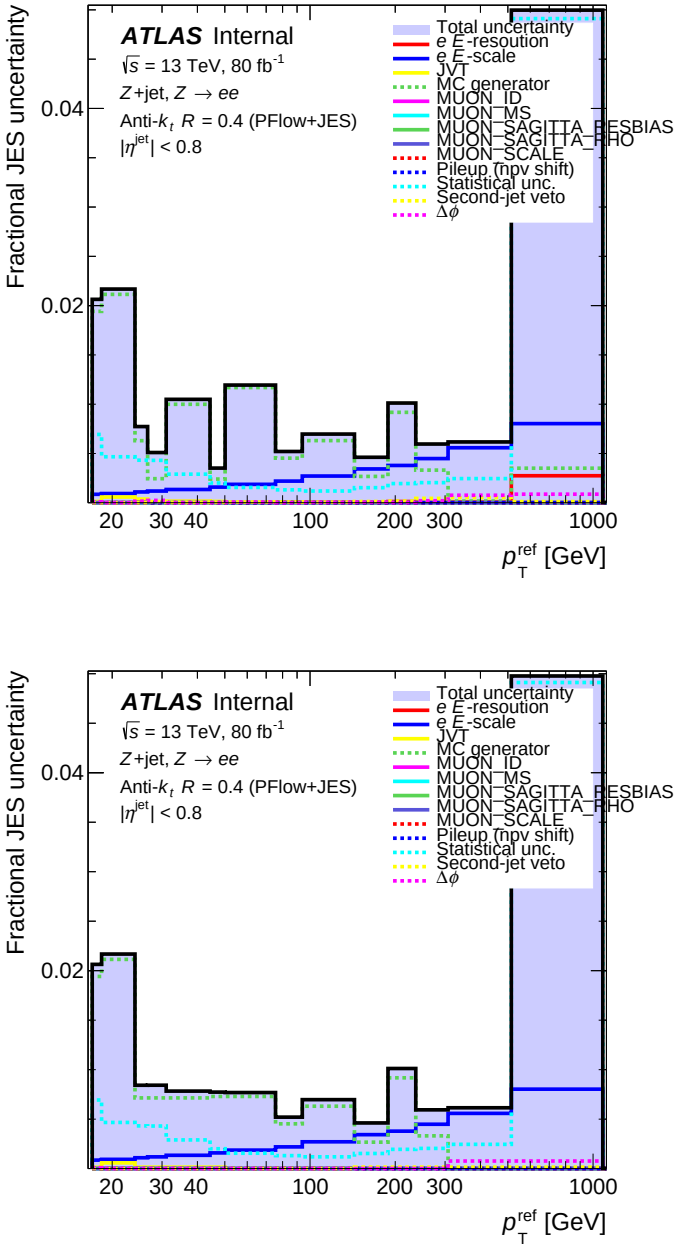

Figure 5.27: The full systematic analysis for the combined electron channel. On the top is the original systematic plot, and the bottom is after rebinning with 2σ significance is applied. Note that the large uncertainty at high-p_t is not important, as these results are not used in that region. The MC Modelling uncertainty dominates, with the statistical uncertainty being the next largest.

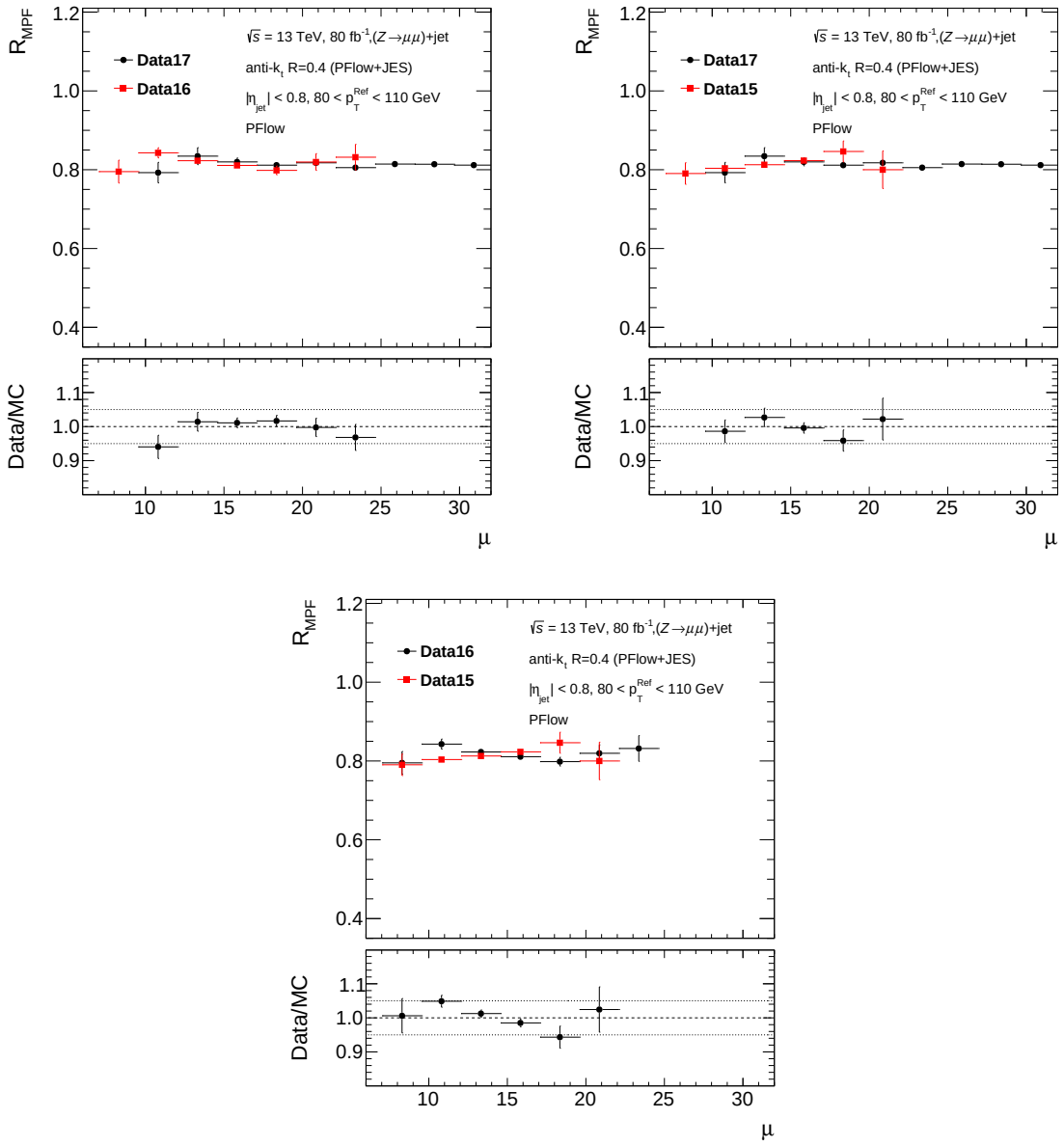

Figure 5.28: Response vs average number of interactions per beam-bunch crossing for the $Z \to \mu\mu$ decay channel for the three different years. The data are shown in one of the lower p_t bins where pile-up is likely to have a larger effect. Little to no dependence on pile-up is seen here, showing that the MPF technique is indeed not sensitive to even significant levels of pile-up.

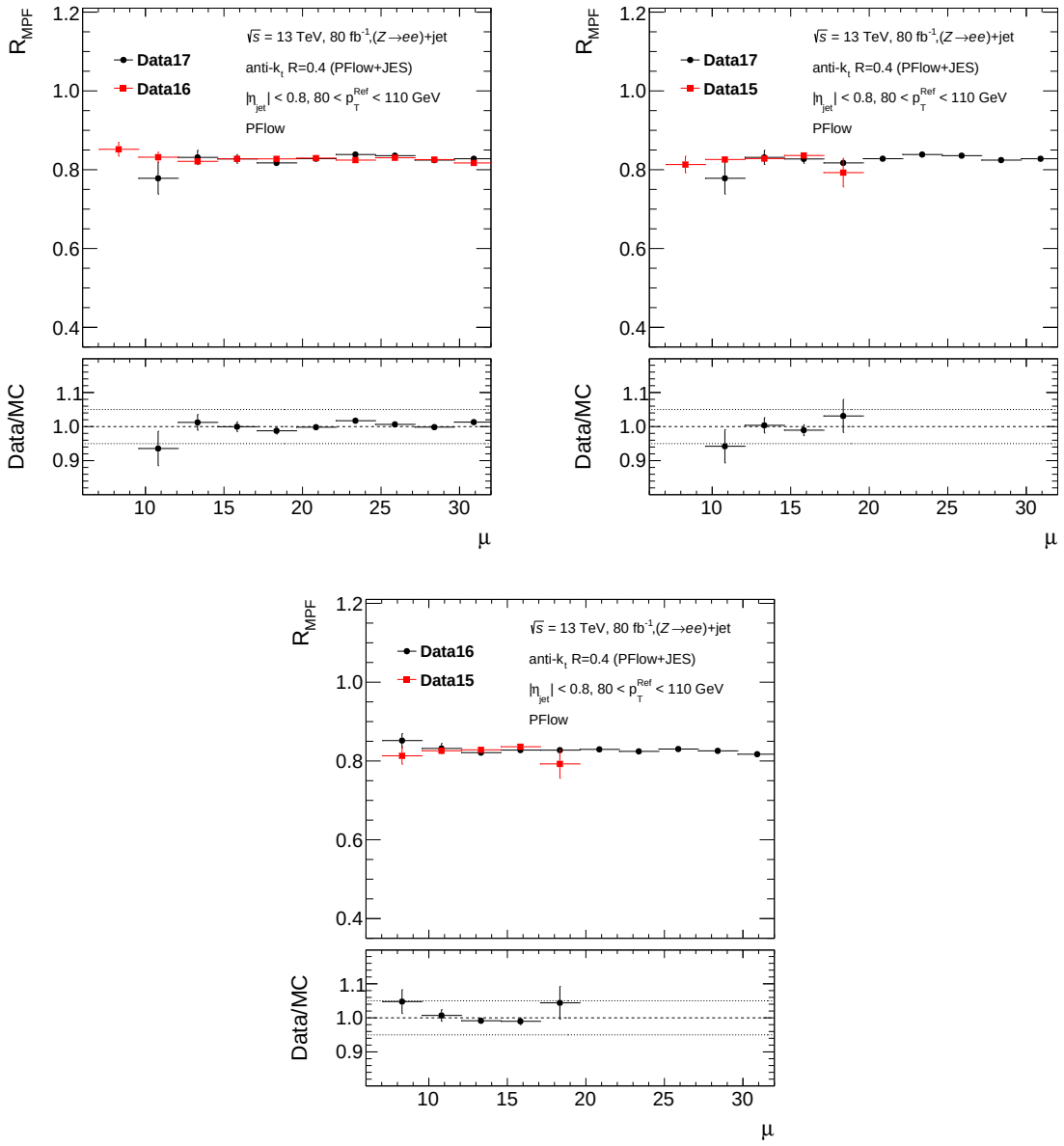

Figure 5.29: Response vs average number of interactions per beam-bunch crossing for the $Z \to ee$ decay channel for the three different years. The data are shown in one of the lower p_t bins where pile-up is likely to have a larger effect. Little to no dependence on pile-up is seen here, showing that the MPF technique is indeed not sensitive to even significant levels of pile-up.

5.4 Consolidated JES Combination

The Z+jet cross-section drops sharply as a function of p_t, such that there are not enough events to be useful beyond about 500 GeV. Other channels, such as γ+jet and multijet production are used at higher p_t.

For the γ+jet channel, all the analysis steps and considerations are similar to the presented Z+jet studies. The final state has a jet back-to-back with a photon. The photon deposits its energy electromagnetically and is therefore well measured. The only things that change in the analysis are the lepton related cuts, systematics, and the photon calibration. The γ+jet channel cannot be used to calibrate low-p_t jets, where the dijet contamination is particularly large because a jet can be misinterpreted as a photon. This jet is not well calibrated and can therefore not provide a good reference object. The distribution of jet energies at low-p_t is wider, resulting in more jets that can fluctuate high enough to fake being a photon, making dijet contamination much more significant. The Z+jet channel is not affected by the large dijet production (as it has a completely different signature of two leptons as opposed to one photon) so it can be used at low-p_t. The benefit of γ+jet is that the cross-section for its production is larger than Z+jet at higher p_t.

Eventually (at around 1 TeV), the γ+jet channel cross-section also falls to a point where there are not enough events for analysis. At this point, the multi-jet balance technique is used. At high p_t, there is an abundance of events in which there are multiple low-energy and one high-energy jet. The calibrations derived from the previous two steps can be applied to the low-energy jets, after which they can be used as reference objects. The whole system of jets must balance, and the low-energy calibrated jets can be used to calibrate the single high-energy jet. This method can be employed for a broad range of p_t, and is limited only around 2.4 TeV, where the production of multi-jet events also falls too low to provide good statistics. After this point, single-particle simulation is the only way of calculating the JES, but it is quite unreliable with significant uncertainties.

The recommended jet collection for ATLAS studies is anti-k_t $R = 0.4$ PFlow jets. For these jets, the consolidated Data/MC ratio can be seen in figure 5.30 and the associated uncertainty plot is shown in figure 5.31. This calibration is the final recommendation that analyzers apply to their Data jets after the previous jet calibration steps.

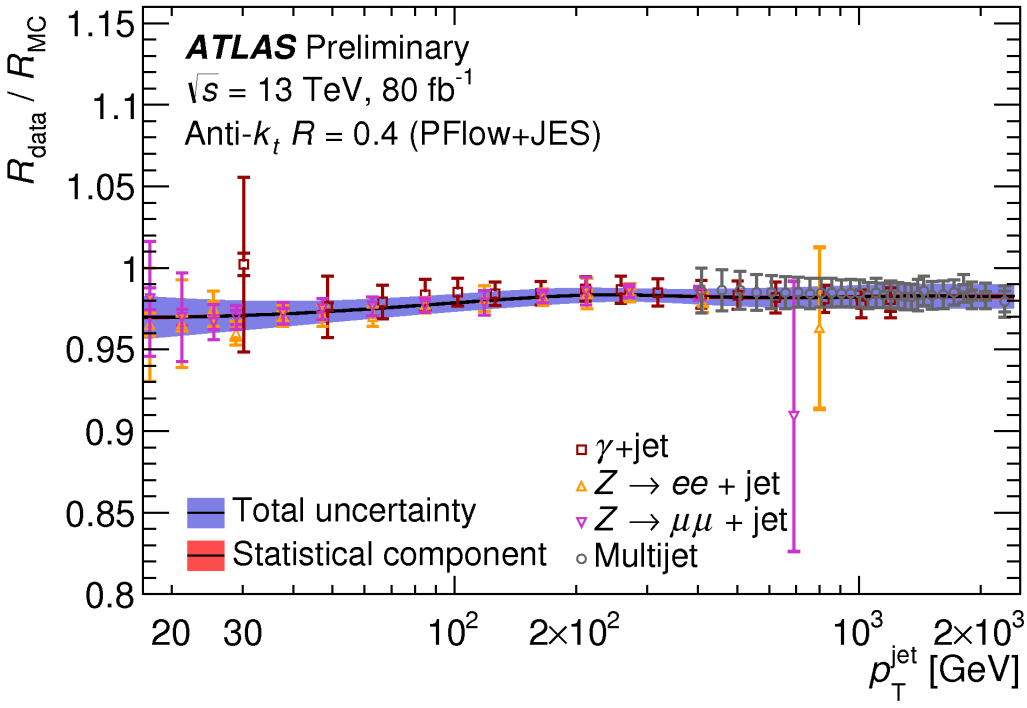

Figure 5.30: The final data/MC calibration for PFlow jets that is provided to the rest of the ATLAS collaboration after the Z+jet results of this paper are combined with the γ+jet channel and the multi-jet balance results.

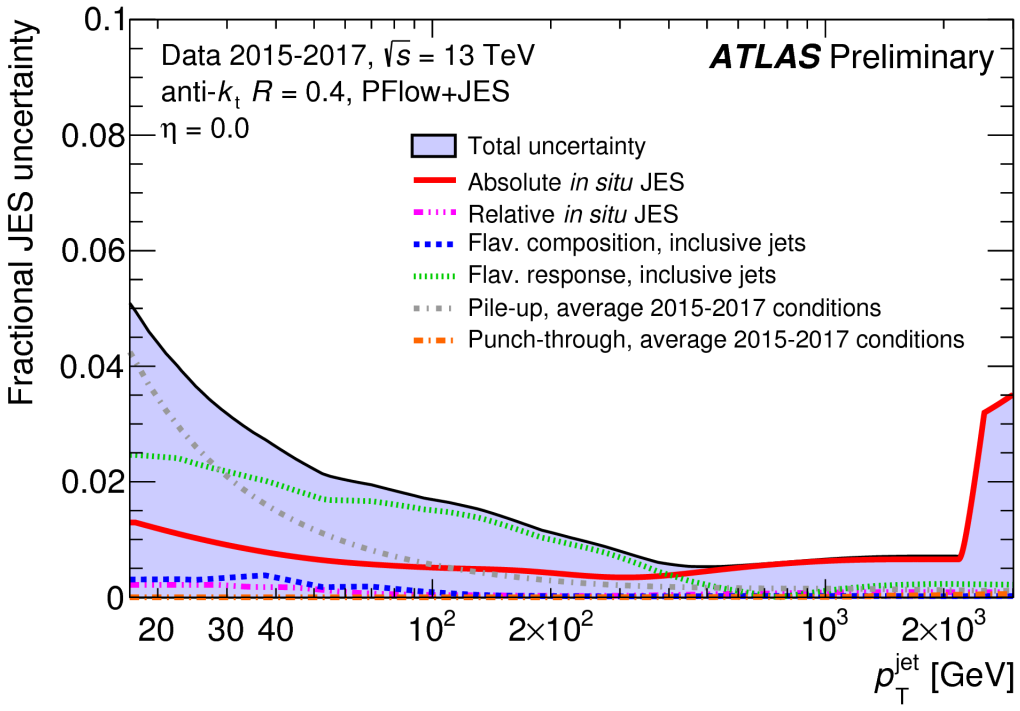

Figure 5.31: The uncertainty on the combined JES for PFlow jets that is provided to the rest of the ATLAS collaboration after the Z+jet results of this paper are combined with the γ+jet channel and the multi-jet balance results. The large spike in the uncertainty at around 2.4 TeV comes from the single-particle simulations response studies [8].

Chapter 6

Conclusion

The main goals of the research presented in this thesis were:

- To provide a jet energy calibration using the 2015-2017 data and the new MC samples.
- To improve on past uncertainties.

Each of these goals has been addressed successfully. The in-situ jet calibration for $R = 0.4$ jets for low-p_t was provided for use by the entire ATLAS community using the 2015-2017 data and the updated MC samples. This step serves as the final step in the jet calibration chain, and accounts for the observed differences in data and MC simulation. For the majority of the p_t range in which the results presented here are most significant, the uncertainties on the Z+jet and the consolidated in-situ recommendations have been lowered to sub-2%. The MPF technique is now used exclusively for the Jet Energy Scale of $R = 0.4$ jets because it has been shown to be insensitive to pile-up effects.

However, there is still work to be done. The numerous problems found in METMaker must be resolved, and the results must converge with the custom methods implemented in this thesis. The Out-of-Cone uncertainties associated with the Direct Balance method and the Showering and Topology corrections for the MPF method must be redone in the new CMAKE software framework of ATLAS and with the updated tools/recommendations. Different radii jets must be checked to ensure that the calibration is stable for different sizes, and the 2018 calibration has to be run through the combination (they have already been produced and submitted for Z+jet, waiting on other analyses to finish their calibrations before the combination).

Through the work presented in this thesis, the uncertainties for the Jet Energy Scale have been lowered, and work can begin to prepare for run 3 of the LHC.

Bibliography

[1] The grid: A system of tiers. https://home.cern/science/computing/grid-system-tiers. Accessed: 2019-08-12.

[2] ATLAS: letter of intent for a general-purpose pp experiment at the large hadron collider at CERN. 1992.

[3] ATLAS inner detector: Technical Design Report, 1. Technical Design Report ATLAS. CERN, Geneva, 1997.

[4] Tagging and suppression of pileup jets with the ATLAS detector. Technical Report ATLAS-CONF-2014-018, CERN, Geneva, May 2014.

[5] Electron identification measurements in ATLAS using $\sqrt{s} = 13$ TeV data with 50 ns bunch spacing. Technical Report ATL-PHYS-PUB-2015-041, CERN, Geneva, Sep 2015.

[6] Selection of jets produced in 13TeV proton-proton collisions with the ATLAS detector. Technical Report ATLAS-CONF-2015-029, CERN, Geneva, Jul 2015.

[7] Electron and photon energy calibration with the ATLAS detector using data collected in 2015 at $\sqrt{s} = 13$ TeV. Technical Report ATL-PHYS-PUB-2016-015, CERN, Geneva, Aug 2016.

[8] Morad Aaboud et al. A measurement of the calorimeter response to single hadrons and determination of the jet energy scale uncertainty using LHC Run-1 *pp*-collision data with the ATLAS detector. Eur. Phys. J., C77(1):26, 2017.

[9] G. Aad, B. Abbott, J. Abdallah, S. Abdel Khalek, O. Abdinov, R. Aben, B. Abi, M. Abolins, O. S. AbouZeid, and et al. Measurement of the z/gamma * boson transverse momentum distribution in pp collisions at s = 7

$$\sqrt{s} = 7$$

tev with the atlas detector. Journal of High Energy Physics, 2014(9), Sep 2014.

[10] Georges Aad et al. Jet energy measurement with the ATLAS detector in proton-proton collisions at $\sqrt{s} = 7$ TeV. Eur. Phys. J., C73(3):2304, 2013.

[11] F. Abe et al. Dijet angular distributions from $\bar{p}p$ collisions at $\sqrt{s} = 1.8$ TeV. Phys. Rev. Lett., 62:3020–3023, 1989.

[12] S. Agostinelli et al. GEANT4: A Simulation toolkit. Nucl. Instrum. Meth., A506:250–303, 2003.

[13] A. Airapetian et al. ATLAS detector and physics performance: Technical Design Report, 1. Technical Design Report ATLAS. CERN, Geneva, 1999.

[14] A. Airapetian et al. ATLAS detector and physics performance: Technical Design Report, 2. Technical Design Report ATLAS. CERN, Geneva, 1999.

[15] Richard D. Ball, Valerio Bertone, Stefano Carrazza, Christopher S. Deans, Luigi Del Debbio, Stefano Forte, Alberto Guffanti, Nathan P. Hartland, José I. Latorre, and et al. Parton distributions for the lhc run ii. Journal of High Energy Physics, 2015(4), Apr 2015.

[16] G.C. Blazey. Run i i jet physics: Proceedings of the run i i qcd and weak boson physics workshop.

[17] Gerhard Bohm and Günter Zech. Introduction to statistics and data analysis for physicists. 01 2010.

[18] Rene Brun and Fons Rademakers. Root — an object oriented data analysis framework. Nuclear Instruments and Methods in Physics Research Section A: Accelerators, Spectrometers, Detectors and Associated Equipment, 389(1):81 – 86, 1997. New Computing Techniques in Physics Research V.

[19] Matteo Cacciari, Gavin P Salam, and Gregory Soyez. The catchment area of jets. Journal of High Energy Physics, 2008(04):005–005, Apr 2008.

[20] Matteo Cacciari, Gavin P. Salam, and Gregory Soyez. FastJet User Manual. Eur. Phys. J., C72:1896, 2012.

[21] Matteo et al Cacciari. The anti-k_t jet clustering algorithm. JHEP 0804:063, 2008.

[22] ATLAS Collaboration. The atlas experiment at the cern large hadron collider. Journal of Instrumentation, 2008.

[23] ATLAS Collaboration. Jet energy measurement with the atlas detector in proton-proton collisions at sqrt(s) = 7 tev. Eur. Phys. J. C, 73 3 2304, 2013.

[24] ATLAS Collaboration. Performance of pile-up mitigation techniques for jets in pp collisions at $\sqrt{s}$=8 tev using the atlas detector, 2015.

[25] ATLAS Collaboration. Muon reconstruction performance of the atlas detector in proton–proton collision data at $\sqrt{s}$=13 tev. Eur. Phys. J. C 76:292, 2016.

[26] ATLAS Collaboration. Jet energy scale measurements and their systematic uncertainties in proton-proton collisions at $\sqrt{s}$ = 13 tev with the atlas detector. Phys. Rev. D 96, 072002, 2017.

[27] ATLAS Collaboration. Jet reconstruction and performance using particle flow with the atlas detector. Eur. Phys. J. C 77 466, 2017.

[28] ATLAS Collaboration. Performance of the atlas trigger system in 2015. Eur. Phys. J. C 77 317, 2017.

[29] ATLAS Collaboration. Topological cell clustering in the atlas calorimeters and its performance in lhc run 1. Eur. Phys. J. C 77 490, 2017.

[30] ATLAS Collaboration. Electron reconstruction and identification in the atlas experiment using the 2015 and 2016 lhc proton-proton collision data at $\sqrt{s}$=13 tev, 2019.

[31] Geant4 Collaboration. Geant4: Physics Reference Manual Release 10.5. CERN, CERN, 2019.

[32] The ATLAS collaboration. Pile-up subtraction and suppression for jets in ATLAS. 2013.

[33] The ATLAS collaboration. Jet global sequential corrections with the ATLAS detector in proton-proton collisions at sqrt(s) = 8 TeV. 2015.

[34] Csaba Csaki. The Minimal supersymmetric standard model (MSSM). Mod. Phys. Lett., A11:599, 1996.

[35] David d'Enterria. Forward jets physics in atlas, cms and lhcb, 2009.

[36] A. Djouadi and R. M. Godbole. Ewsb at LHC. (arXiv:0901.2030):47–74. 27 p, Jan 2009. Comments: 27 pages, 45 figures, uses LaTeX (insa.sty). Invited review for volume on LHC physics to celebrate the Platinum Jubilee of the Indian National Science Academy, edited by Amitava Datta, Biswarup Mukhopadhyaya and Amitava Raychaudhuri.

[37] Nataliia Cherkashyna et al. Overcoming high energy backgrounds at pulsed spallation sources, 2015.

[38] T. et al Gleisberg. Event generation with sherpa 1.1. JHEP 0902:007, 2009.

[39] C. Grupen and B. Shwartz. Particle Detectors. Cambridge University Press, Cambridge, UK, 2008.

[40] Peter W. Higgs. Broken symmetries and the masses of gauge bosons. Phys. Rev. Lett., 13:508–509, Oct 1964.

[41] Arthur James Horton. IN-SITU MEASUREMENT OF THE JET ENERGY SCALE AND STUDIES OF JET STRUCTURE AT ATLAS. Simon Fraser University, Burnaby, BC, 2017.

[42] Andrew Milder. Dijet angular distributions at square root of s = 1800 gev using the d0 detector. 01 1993.

[43] Bartosz Mindur. ATLAS Transition Radiation Tracker (TRT): Straw tubes for tracking and particle identification at the Large Hadron Collider. Technical Report ATL-INDET-PROC-2016-001, CERN, Geneva, Mar 2016.

[44] Vasiliki A. Mitsou. The ATLAS Transition Radiation Tracker. The ATLAS Transition Radiation Tracker. Technical Report ATL-CONF-2003-012, CERN, Geneva, Nov 2003.

[45] Pavel M. Nadolsky, Hung-Liang Lai, Qing-Hong Cao, Joey Huston, Jon Pumplin, Daniel Stump, Wu-Ki Tung, and C.-P. Yuan. Implications of cteq global analysis for collider observables. Physical Review D, 78(1), Jul 2008.

[46] K. A. Olive et al. Review of Particle Physics. Chin. Phys., C38:090001, 2014.

[47] Joao Pequenao. Computer Generated image of the ATLAS calorimeter. Mar 2008.

[48] Joao Pequenao. Computer generated image of the ATLAS inner detector. Mar 2008.

[49] Joao Pequenao. Computer generated image of the ATLAS Muons subsystem. Mar 2008.

[50] Joao Pequenao. Computer generated image of the whole ATLAS detector. Mar 2008.

[51] Joao Pequenao. Event Cross Section in a computer generated image of the ATLAS detector. Mar 2008.

[52] Estel Perez Codina. Small-Strip Thin Gap Chambers for the Muon Spectrometer Upgrade of the ATLAS Experiment. Technical Report ATL-MUON-PROC-2015-004, CERN, Geneva, Jun 2015.

[53] Matthias Schott and Monica Dunford. Review of single vector boson production in pp collisions at $\sqrt{s} = 7$ TeV. Eur. Phys. J. C, 74(arXiv:1405.1160):60 p, May 2014.

[54] Douglas William Schouten. Jet Energy Scale Calibration in ATLAS. Simon Fraser University, Burnaby, BC, 2007.

[55] Douglas William Schouten. Determination of the QCD Jet Energy Scale and Measurement of the Single Top Quark Cross Section at ATLAS. Simon Fraser University, Burnaby, BC, 2011.

[56] T. et al Sjöstrand. A brief introduction to pythia 8.1. Comput.Phys.Commun.178:852-867, 2008.

[57] Yosuke Takubo. ATLAS IBL operational experience. Technical Report ATL-INDET-PROC-2016-012, CERN, Geneva, Nov 2016.

[58] M. Thomson. Modern Particle Physics. Cambridge University Press, Cambridge, 2013.

[59] Stefan Weinzierl. The siscone jet algorithm optimised for low particle multiplicities. Computer Physics Communications, 183(3):813–820, Mar 2012.

[60] R. Wigmans. Calorimetry: Energy Measurement in Particle Physics. Oxford, 198 Madison Avenue, New York, United States of America, 2017.

Appendix A

Personal Contributions

The ATLAS collaboration is a global team of thousands of people contributing to hundreds of tasks. It may not be clear which work can be attributed to which person. To address this, I provide a list of all my personal contributions.

- Migrated the existing InSitu analysis framework from the deprecated 20.7 rootcore architecture to the CMAKE based release 21.
- Rewrote the code to make it more legible and efficient.
- Implemented many new features into the code such as different MET options, automatic pileup reweighting, systematics handling, automatic implementation of new studies, simultaneous running of multiple studies, automated batch submissions, automated plotting scripts, fixed numerous errors and bugs, made the code widely available on gitlab, implemented the pileup reweighting scripts to work on the outputs produced by the code.
- Implemented and merged the large-R analysis code into the InSitu framework. Small-R refers to jets of size $R = 0.4$, and large-R refers to $R = 1.0$. Large-R jets have to be handled differently, resulting in many new studies and methods. I did not write these studies, but I did merge them into the small-R code to make one standing V+Jet InSitu framework.
- Maintained plotting scripts.
- Produced $Z + Jet$ results for the run 2 calibration using 2015-2017 data for both EMTopo and PFlow scales.
- Produced an estimate on the showering and topology correction using previously obtained results (now shown in this thesis).
- Lowered the uncertainties on the jet energy scale.
- Produced pileup dependence studies to show pileup hardness.
- Proved the merits of MPF over DB to the point that the calibration is now entirely MPF based.

- Identified an issue with METMaker and provided a simple alternative.
- Conducted studies to check the dependence of the calibration on the $\Delta\phi$ and sub-leading jet cuts.
- Conducted low-p_t studies.

Appendix B

Configurations

Here I list the various data and configurations files used to derive the results presented in this thesis.

The code framework is written in EventLoop, and the AnalysisBase release 21.2.39 was used for these results.

The data sets used for the 2015 and 2016 results are:

- Data:
  - 2015: data15_13TeV.*physics_Main.deriv.DAOD_JETM3*p3372
  - 2016: data16_13TeV.*physics_Main.deriv.DAOD_JETM3*p3372
- MC16a:
  - $Z \to \mu\mu$ Pythia: mc16_13TeV.*Pythia*Zmumu*JETM3*s3126*r9364*p3371
  - $Z \to ee$ Pythia : mc16_13TeV.*Pythia*Zee*JETM3*s3126*r9364*p3371
  - $Z \to \mu\mu$ Sherpa: mc16_13TeV.*Sherpa*Zmumu*JETM3*s3126*r9364*p3371
  - $Z \to ee$ Sherpa : mc16_13TeV.*Sherpa*Zee*JETM3*s3126*r9364*p3371

The data sets used for the 2017 results are:

- Data:
  - 2017 Set 1: data17_13TeV.*physics_Main.deriv.DAOD_JETM3*p3372
  - 2017 Set 2: data17_13TeV.*physics_Main.deriv.DAOD_JETM3*p3402
- MC16d:
  - $Z \to \mu\mu$ Pythia:
    mc16_13TeV.*Pythia*Zm*JETM3*s3126*r10201*r10210*

- $Z \to ee$ Pythia :
  mc16_13TeV.*PowhegPythia*Zee*JETM3*s3126*r10201*r10210*
- $Z \to \mu\mu$ Sherpa:
  mc16_13TeV.*Sherpa*Zm*JETM3*s3126*r10201*r10210*
- $Z \to ee$ Sherpa :
  mc16_13TeV.*Sherpa*Zee*JETM3*s3126*r10201*r10210*

The GoodRunsLists used were:

- 2015: data15_13TeV.periodAllYear_DetStatus-v89-pro21-02...
  ... _Unknown_PHYS_StandardGRL_All_Good_25ns.xml
- 2016: data16_13TeV.periodAllYear_DetStatus-v88-pro20-21...
  ... _DQDefects-00-02-04_PHYS_StandardGRL_All_Good_25ns.xml
- 2017: data17_13TeV.periodAllYear_DetStatus-v97-pro21-13...
  ... _Unknown_PHYS_StandardGRL_All_Good_25ns_Triggerno17e33prim.xml

The jet calibration configuration files used were:

- EM 2017: JES_2017data_PFlow_EtaInterCalibrationOnly_ ...
  ...08Feb2018.config
- EM 2015/16: JES_MC16Recommendation_EtaInterCalibrationOnly_ ...
  ... 20Dec2017.config
- PFlow 2017: JES_2017data_PFlow_EtaInterCalibrationOnly_ ...
  ... 08Feb2018.config
- PFlow 2015/16: JES_MC16Recommendation_PFlow_ ...
  ... EtaInterCalibrationOnly_20Dec2017.config

The muon triggers used were:

- 2015: HLT_2mu10
- 2016: HLT_2mu10
- 2017: HLT_2mu14

The electron triggers used were:

- 2015: HLT_2e12_lhloose_L12EM10VH
- 2016: HLT_2e15_lhvloose_nod0_L12EM13VH
- 2017: HLT_2e17_lhvloose_nod0_L12EM15VHI

Appendix C

Auxiliary Plots

C.1 Response p_t Bins and Fits - EMTopo

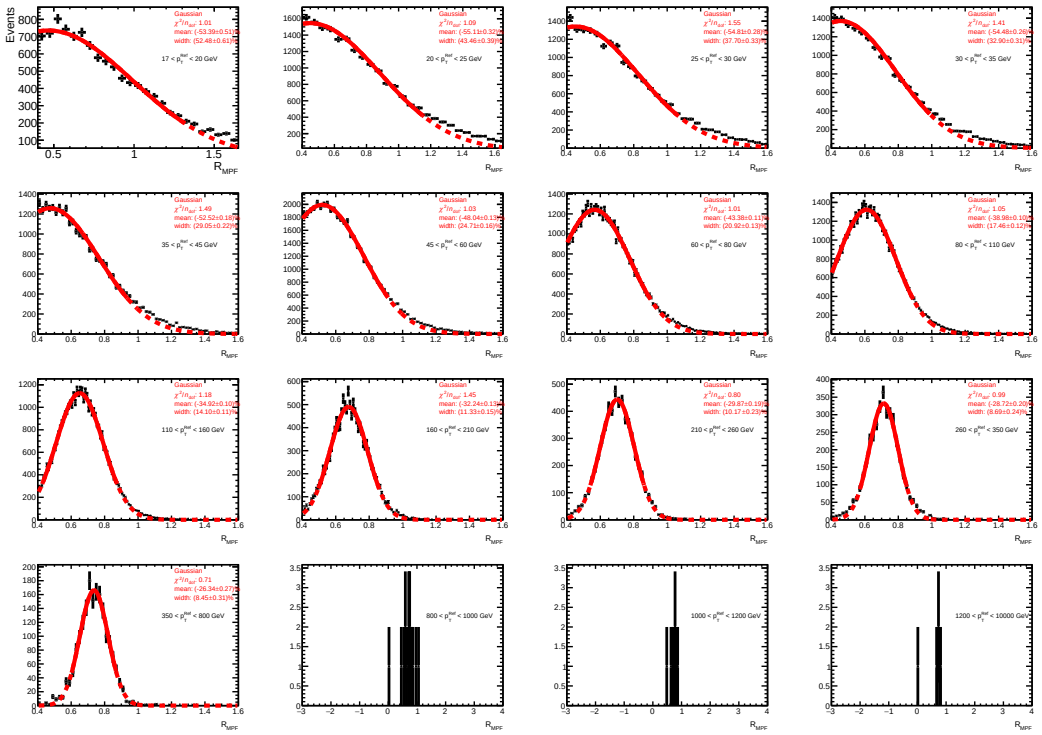

Figure C.1: The p_t bins and corresponding response distributions/fits for EMTopo in the Z$\rightarrow \mu\mu$ decay channel, for all data years. The x-axis cutoff is purely an artefact of plotting, and does not reflect the actual fit range.

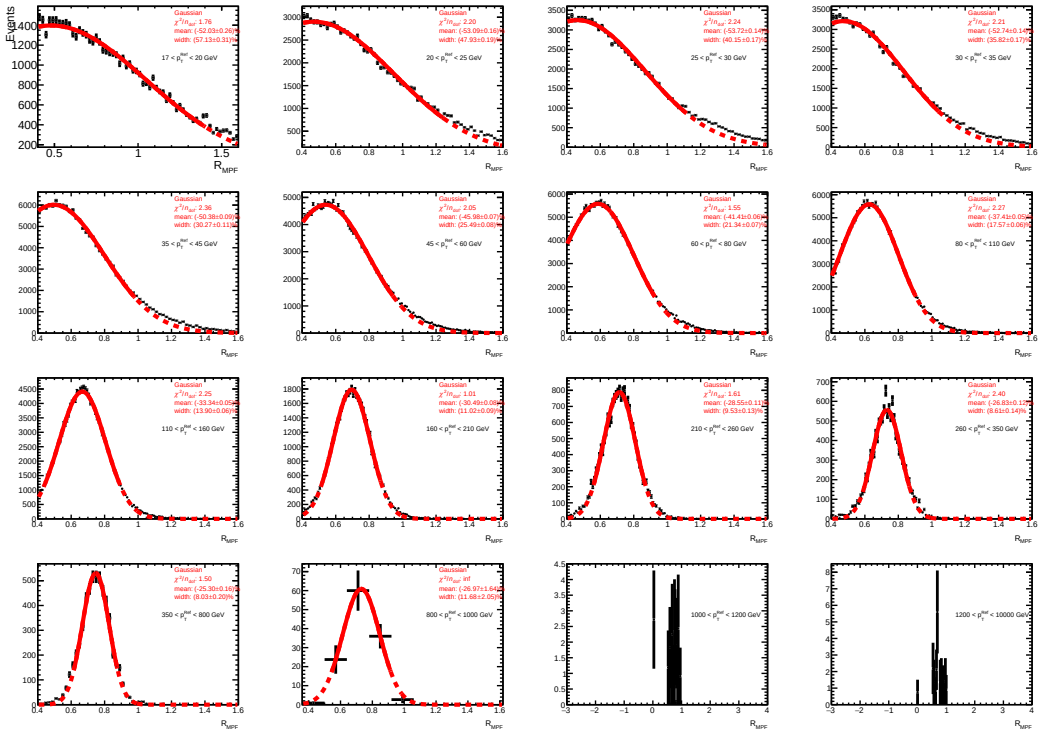

Figure C.2: The p_t bins and corresponding response distributions/fits for EMTopo in the Z$\rightarrow \mu\mu$ decay channel, for Pythia. The x-axis cutoff is purely an artefact of plotting, and does not reflect the actual fit range.

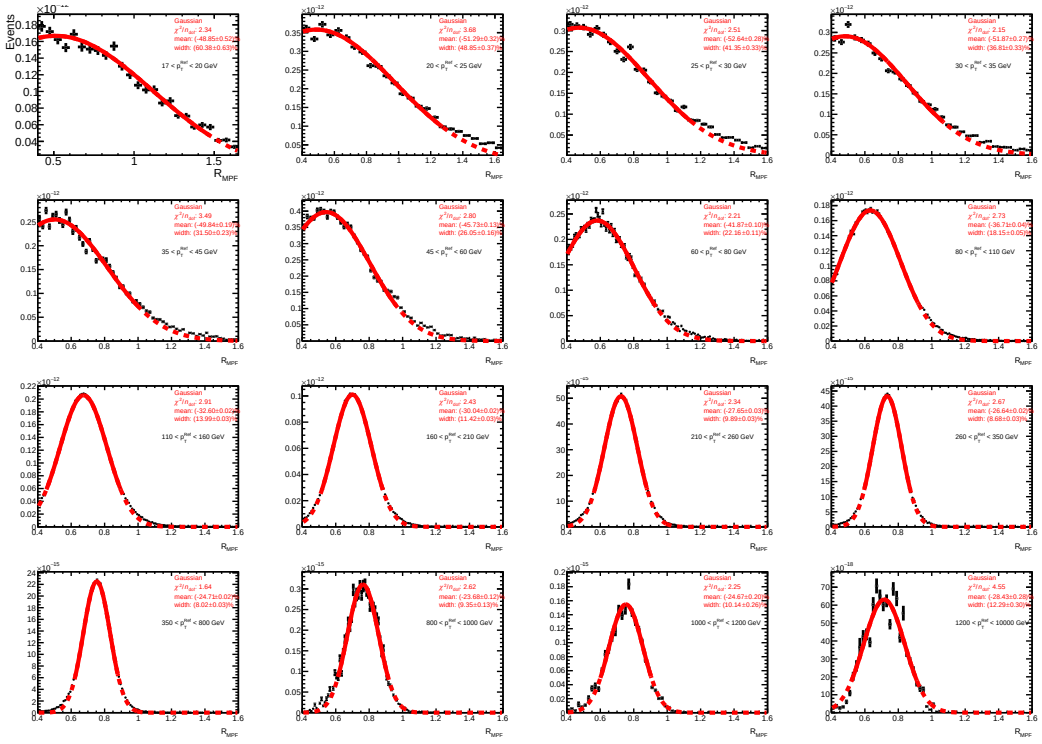

Figure C.3: The p_t bins and corresponding response distributions/fits for EMTopo in the Z$\rightarrow \mu\mu$ decay channel, for Sherpa. The x-axis cutoff is purely an artefact of plotting, and does not reflect the actual fit range.

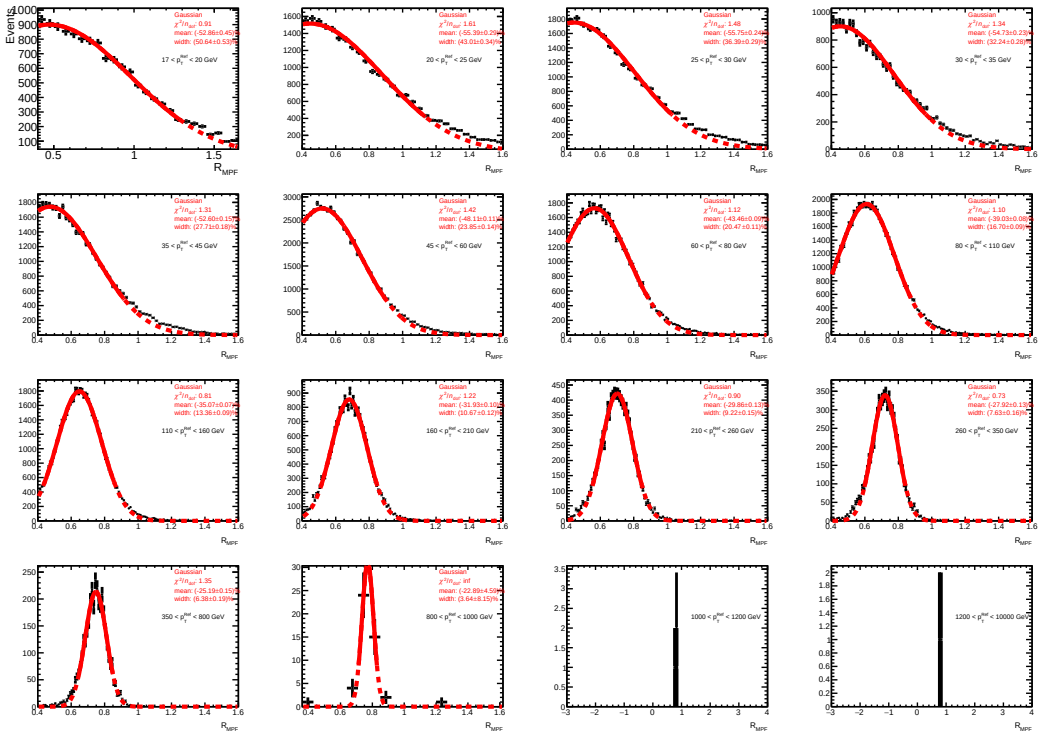

Figure C.4: The p_t bins and corresponding response distributions/fits for EMTopo in the Z$\rightarrow$ *ee* decay channel, for all data years. The x-axis cutoff is purely an artefact of plotting, and does not reflect the actual fit range.

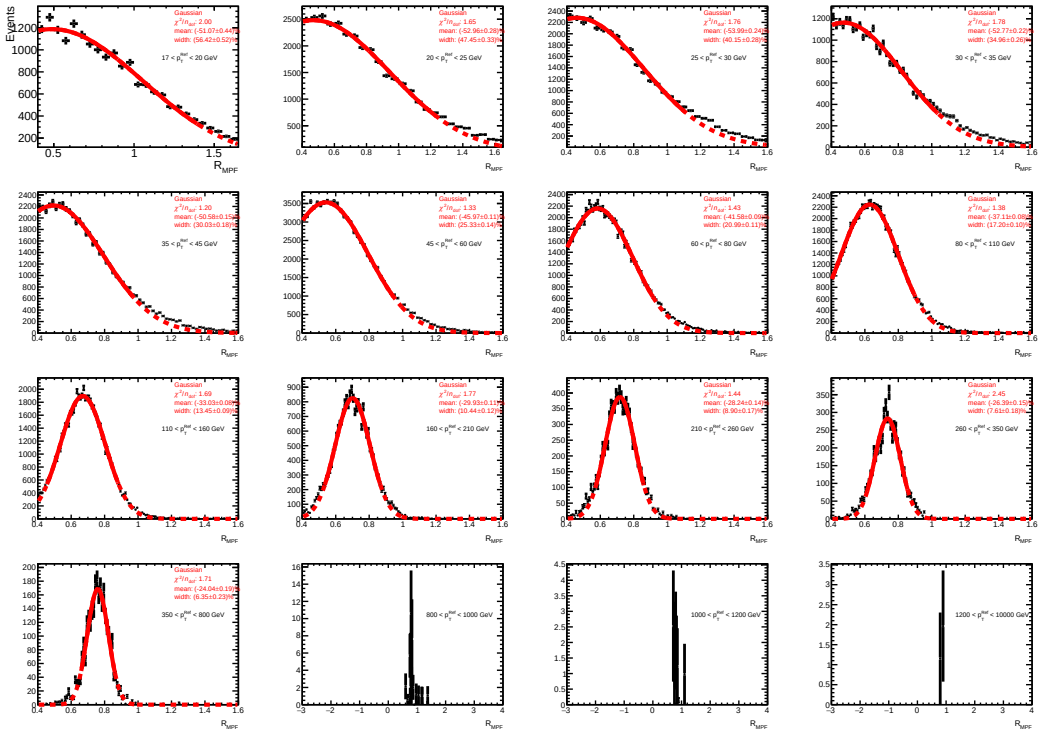

Figure C.5: The p_t bins and corresponding response distributions/fits for EMTopo in the Z$\rightarrow$ *ee* decay channel, for Pythia. The x-axis cutoff is purely an artefact of plotting, and does not reflect the actual fit range.

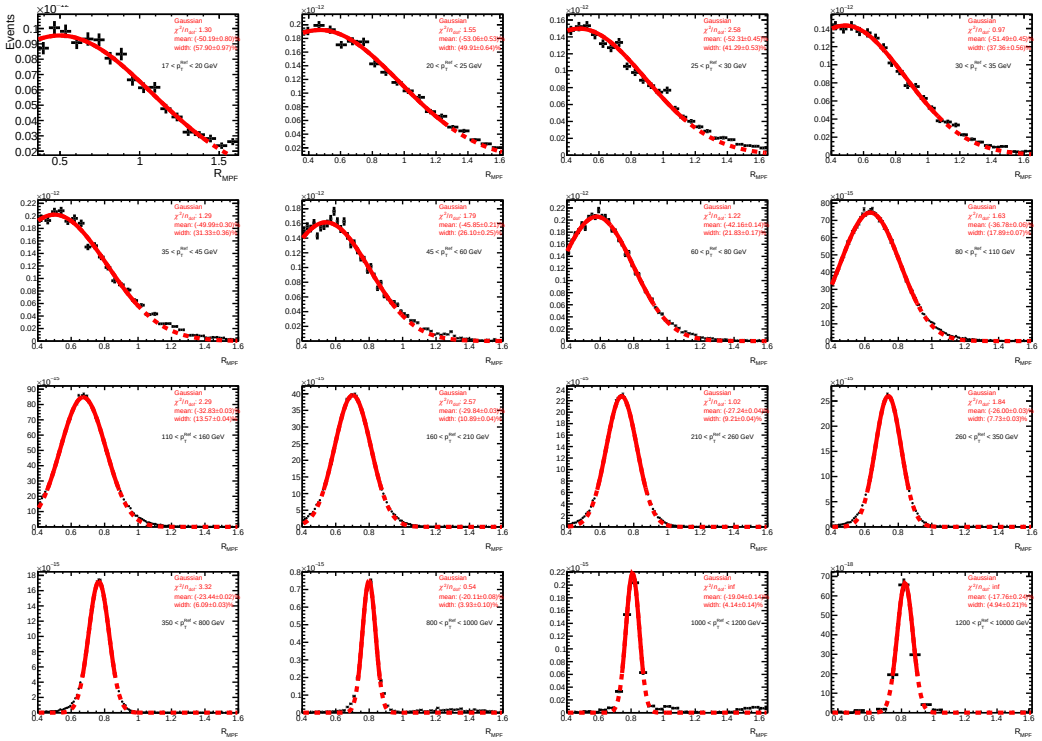

Figure C.6: The p_t bins and corresponding response distributions/fits for EMTopo in the Z→ *ee* decay channel, for Sherpa. The x-axis cutoff is purely an artefact of plotting, and does not reflect the actual fit range.

C.2 Response p_t Bins and Fits - PFlow

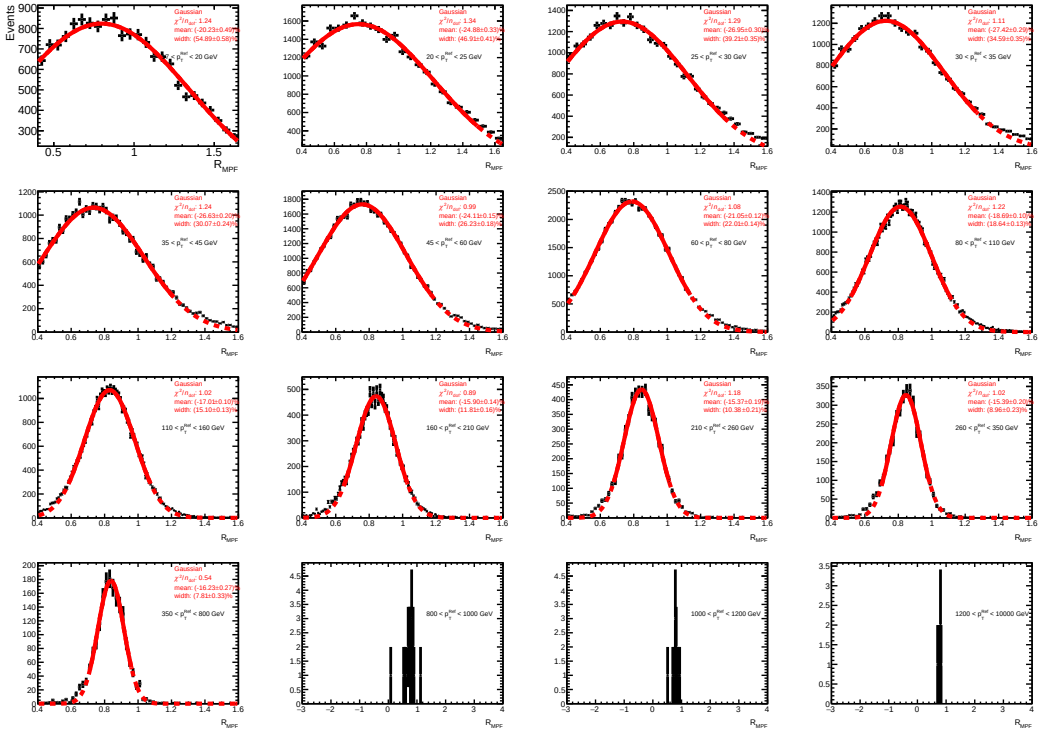

Figure C.7: The p_t bins and corresponding response distributions/fits for PFlow in the Z$\rightarrow \mu\mu$ decay channel, for all data years. The x-axis cutoff is purely an artefact of plotting, and does not reflect the actual fit range.

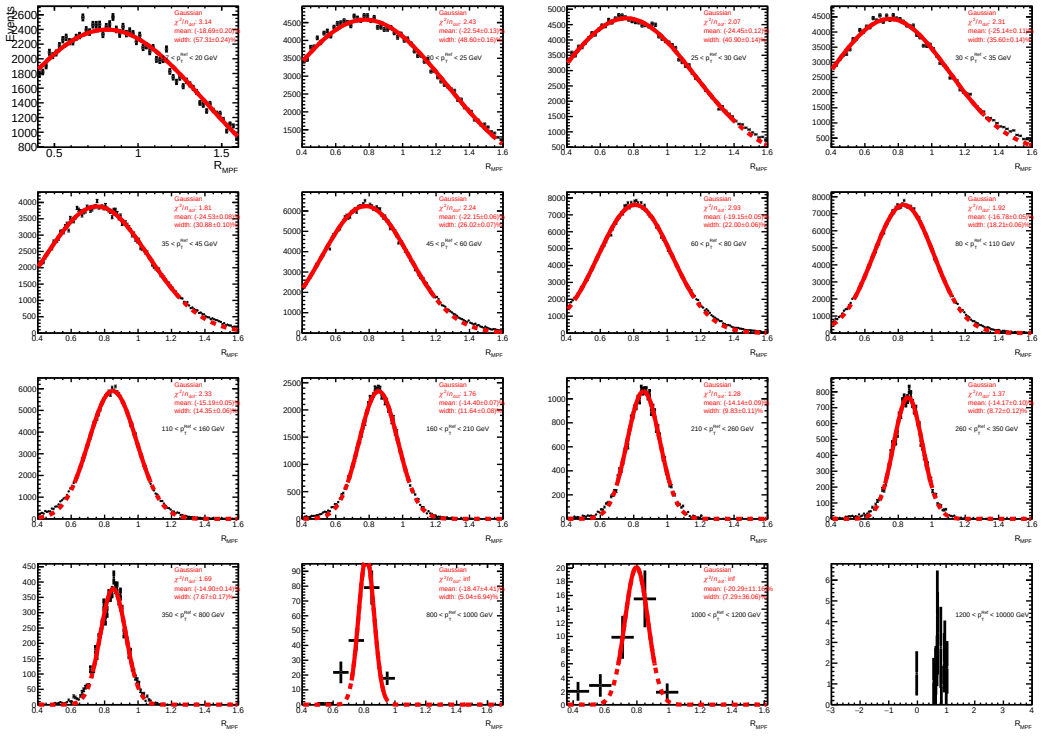

Figure C.8: The p_t bins and corresponding response distributions/fits for PFlow in the Z$\rightarrow \mu\mu$ decay channel, for Pythia. The x-axis cutoff is purely an artefact of plotting, and does not reflect the actual fit range.

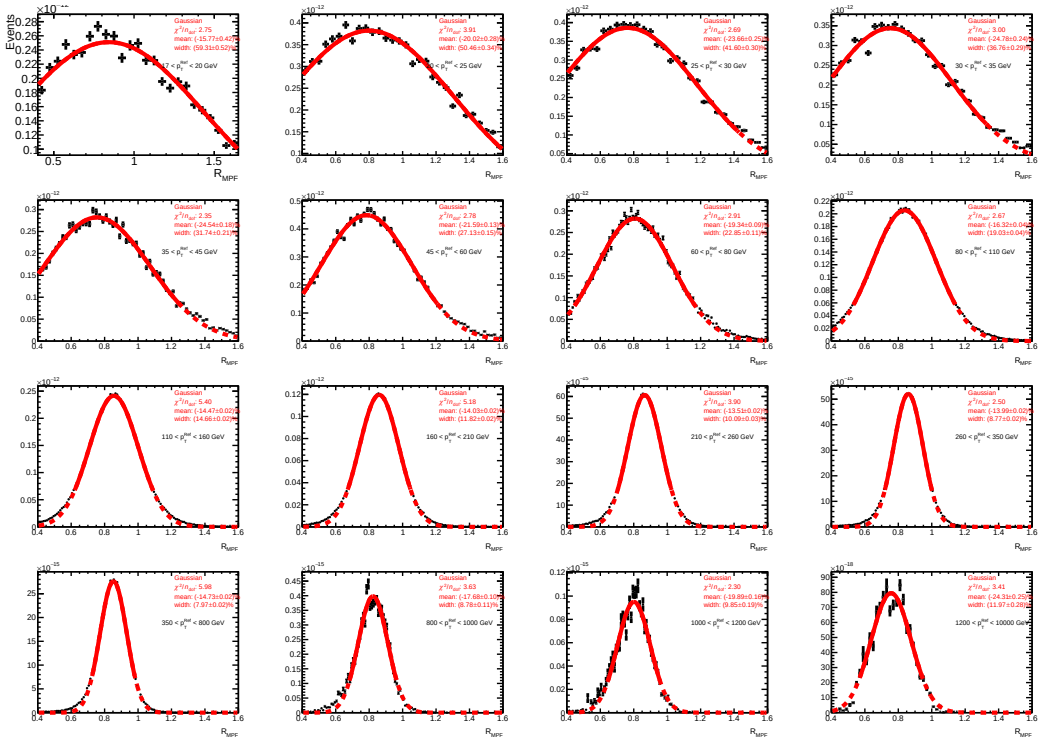

Figure C.9: The p_t bins and corresponding response distributions/fits for PFlow in the Z$\rightarrow \mu\mu$ decay channel, for Sherpa. The x-axis cutoff is purely an artefact of plotting, and does not reflect the actual fit range.

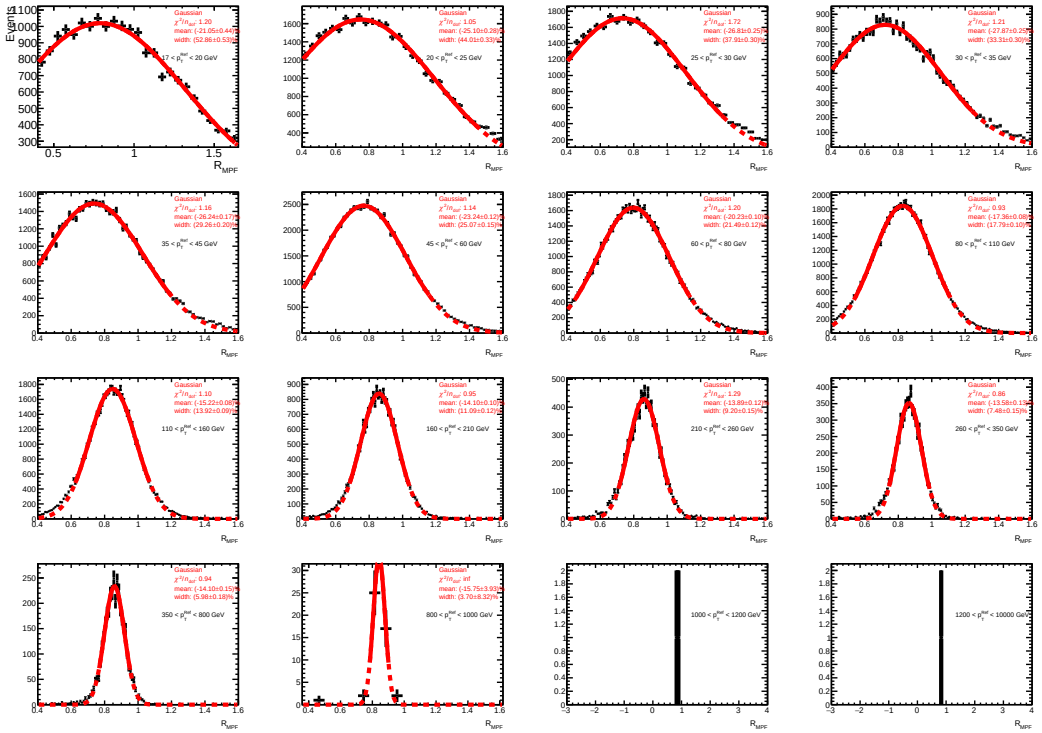

Figure C.10: The p_t bins and corresponding response distributions/fits for PFlow in the Z→ *ee* decay channel, for all data years. The x-axis cutoff is purely an artefact of plotting, and does not reflect the actual fit range.

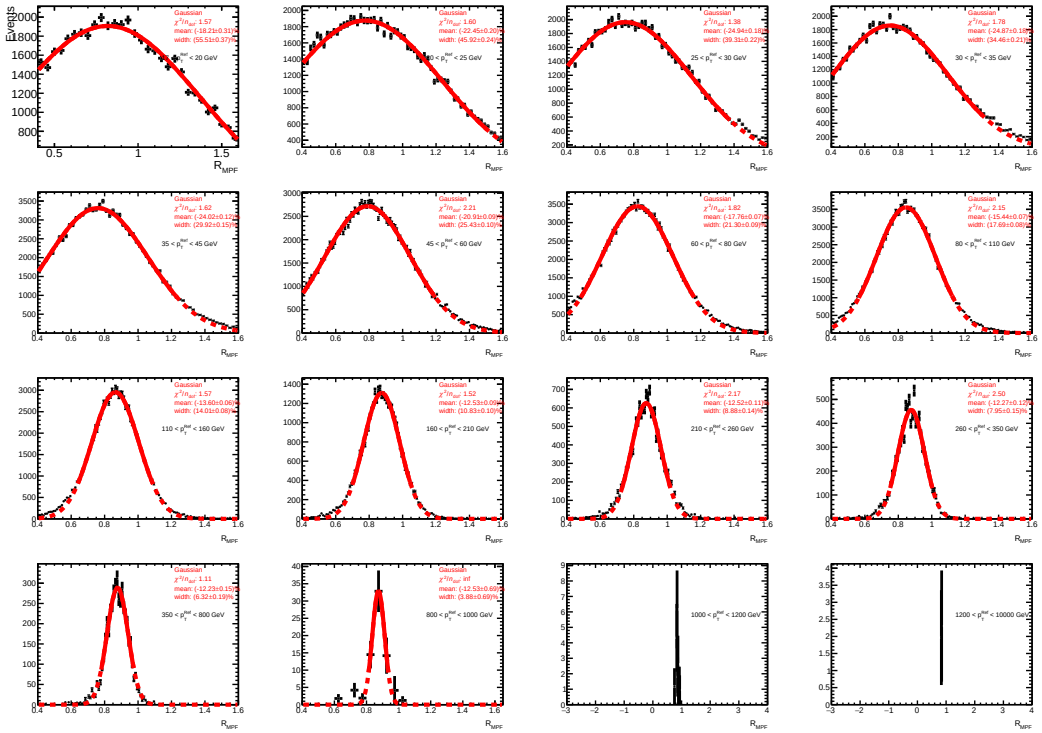

Figure C.11: The p_t bins and corresponding response distributions/fits for PFlow in the Z$\rightarrow$ *ee* decay channel, for Pythia. The x-axis cutoff is purely an artefact of plotting, and does not reflect the actual fit range.

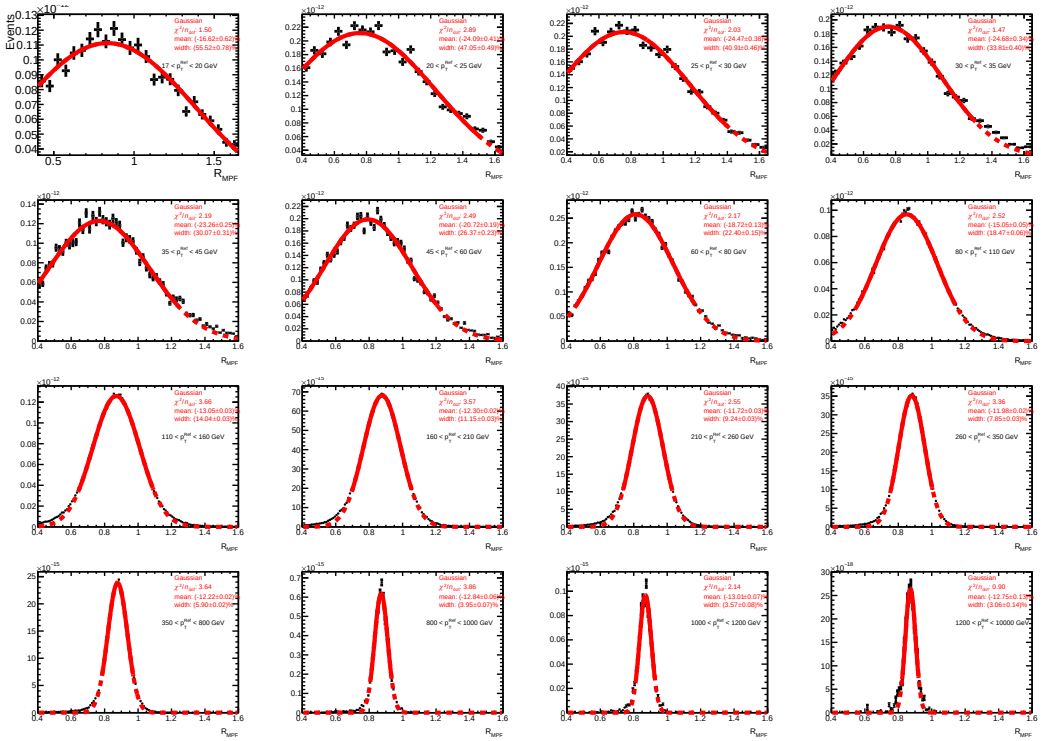

Figure C.12: The p_t bins and corresponding response distributions/fits for PFlow in the Z→ *ee* decay channel, for Sherpa. The x-axis cutoff is purely an artefact of plotting, and does not reflect the actual fit range.

C.3 Cutflow - EMTopo

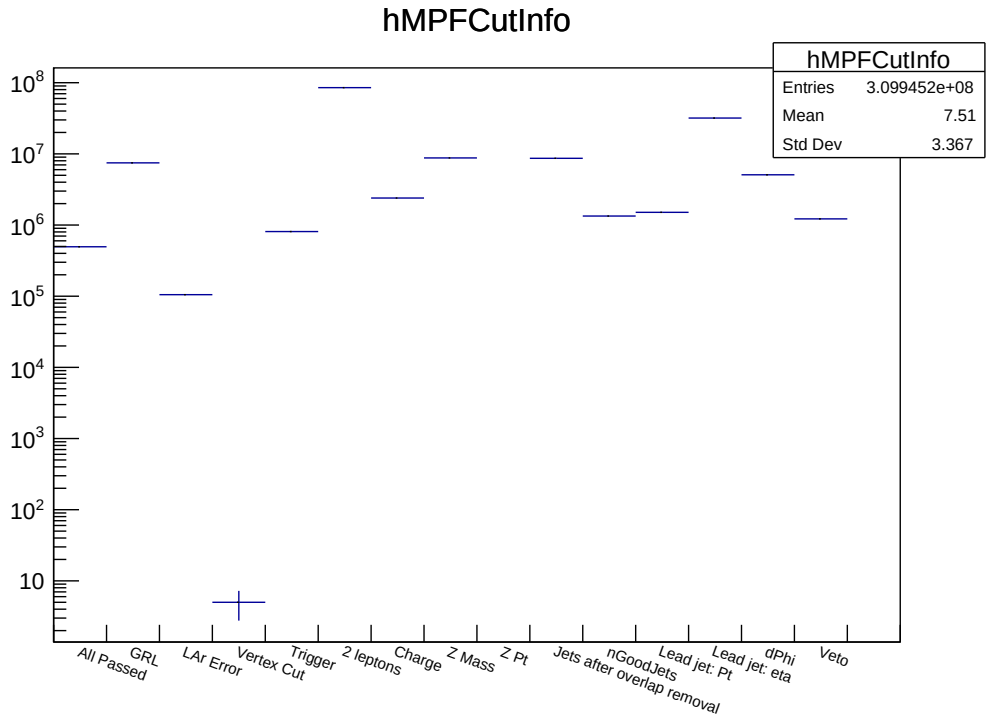

Figure C.13: The cutflow (each bin shows number of events that failed the corresponding cut) for EMTopo in the Z$\rightarrow \mu\mu$ decay channel, for all data years.

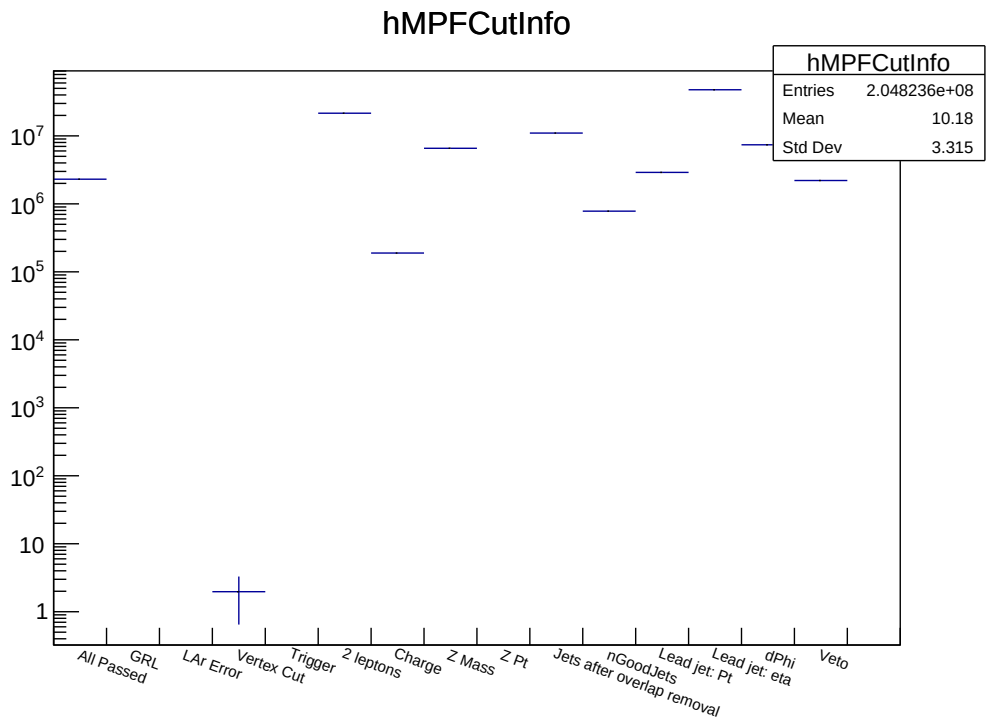

Figure C.14: The cutflow (each bin shows number of events that failed the corresponding cut) for EMTopo in the Z$\rightarrow \mu\mu$ decay channel, for Pythia.

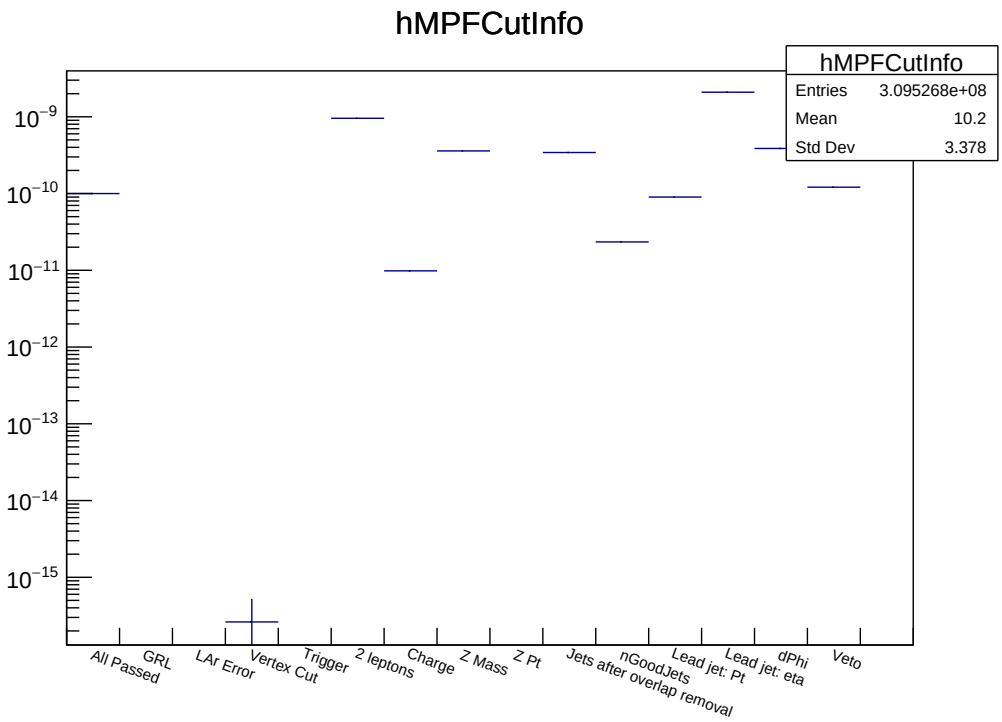

Figure C.15: The cutflow (each bin shows number of events that failed the corresponding cut) for EMTopo in the Z$\rightarrow \mu\mu$ decay channel, for Sherpa.

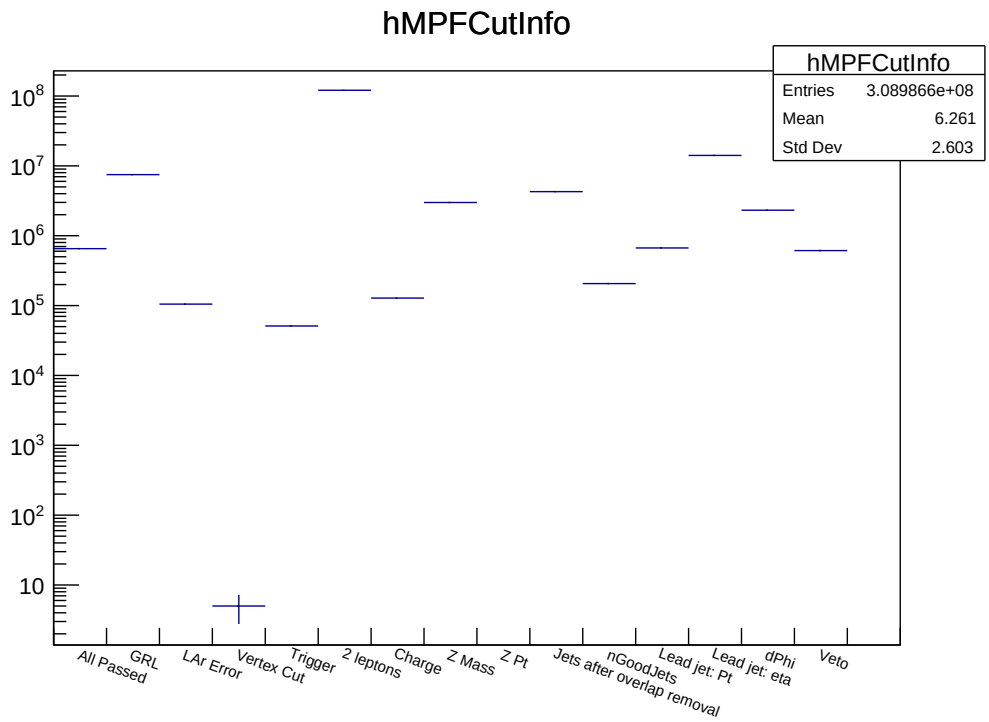

Figure C.16: The cutflow (each bin shows number of events that failed the corresponding cut) for EMTopo in the Z→ *ee* decay channel, for all data years.

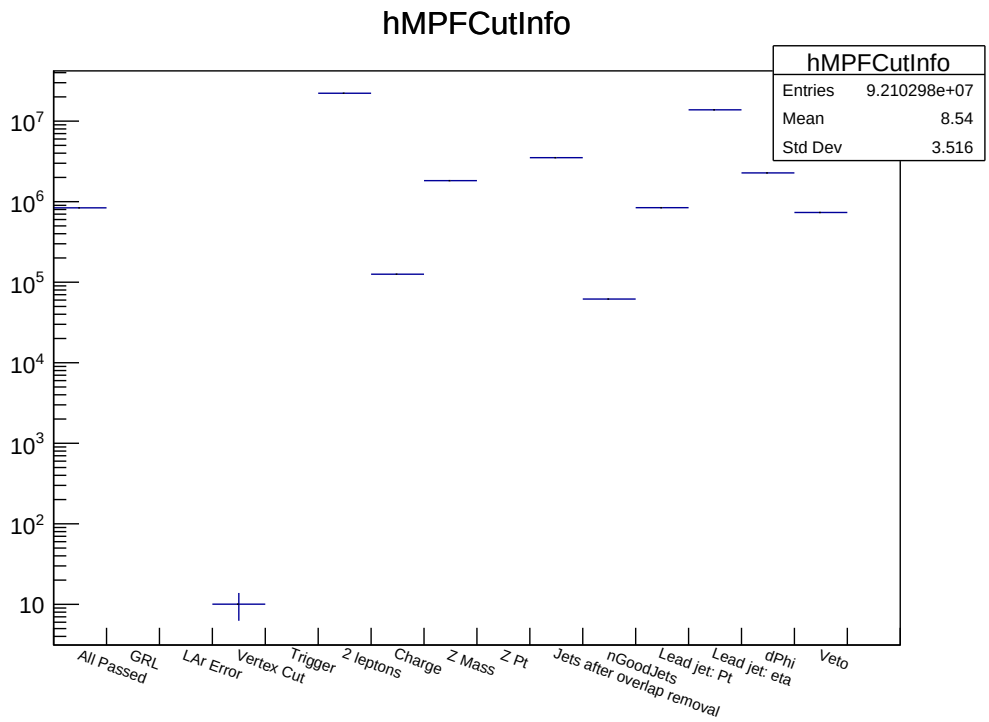

Figure C.17: The cutflow (each bin shows number of events that failed the corresponding cut) for EMTopo in the Z→ *ee* decay channel, for Pythia.

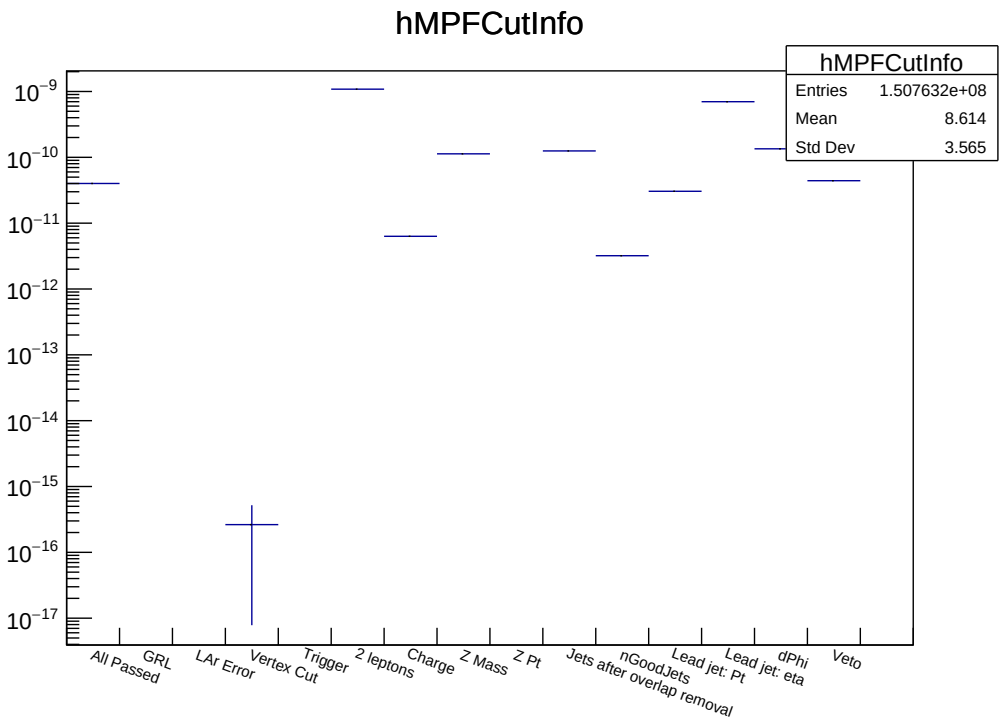

Figure C.18: The cutflow (each bin shows number of events that failed the corresponding cut) for EMTopo in the Z→ *ee* decay channel, for Sherpa.

C.4 Cutflow - PFlow

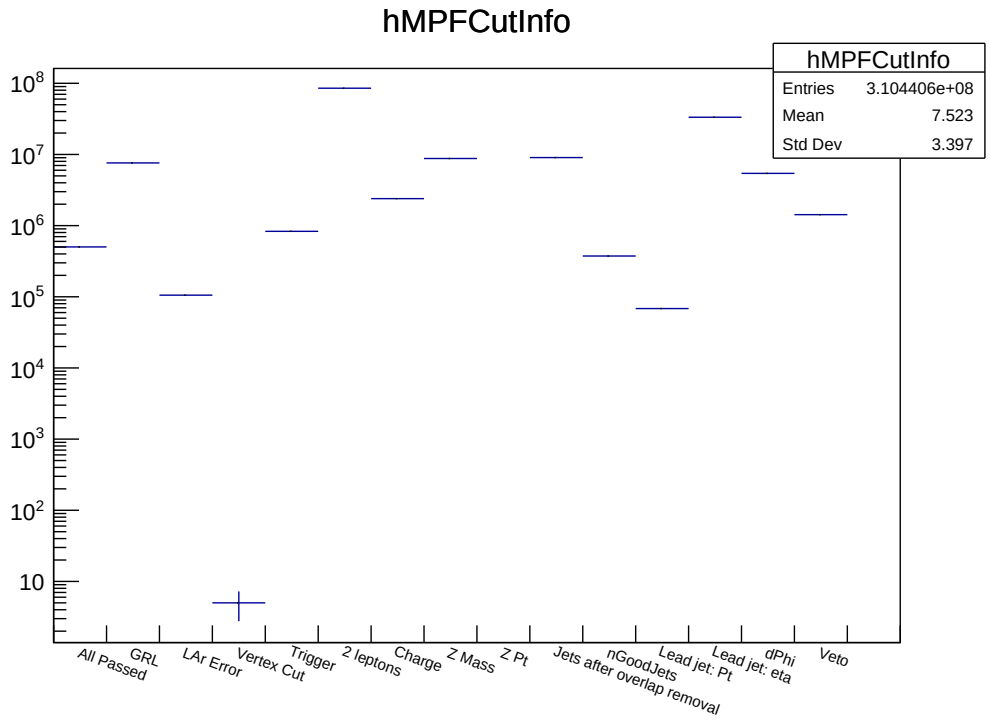

Figure C.19: The cutflow (each bin shows number of events that failed the corresponding cut) for PFlow in the Z$\rightarrow \mu\mu$ decay channel, for all data years.

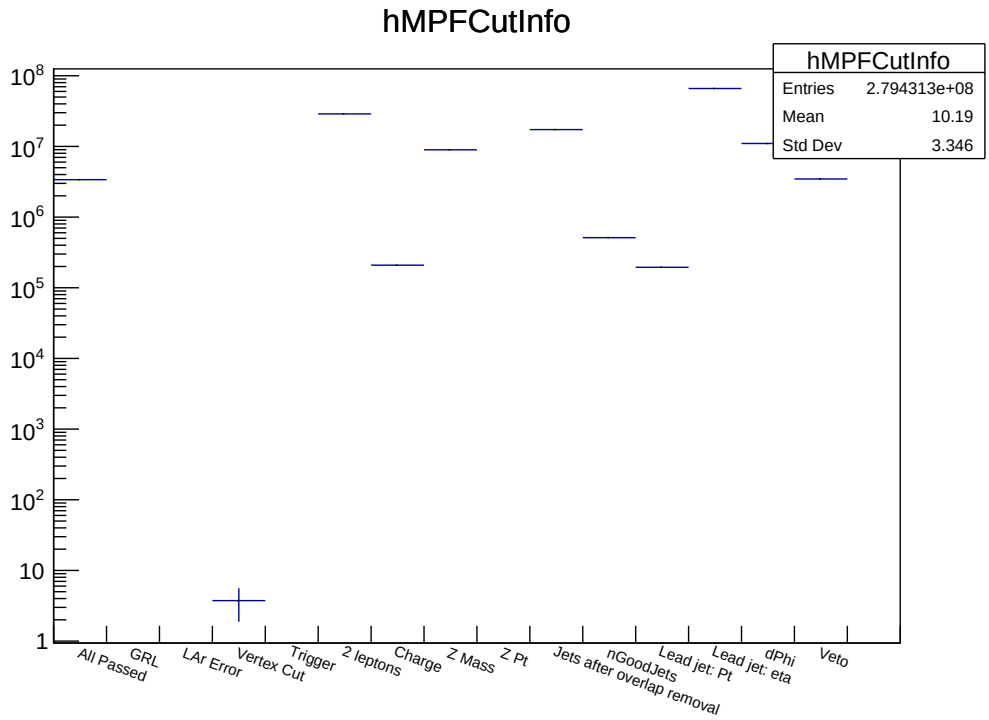

Figure C.20: The cutflow (each bin shows number of events that failed the corresponding cut) for PFlow in the Z$\rightarrow \mu\mu$ decay channel, for Pythia.

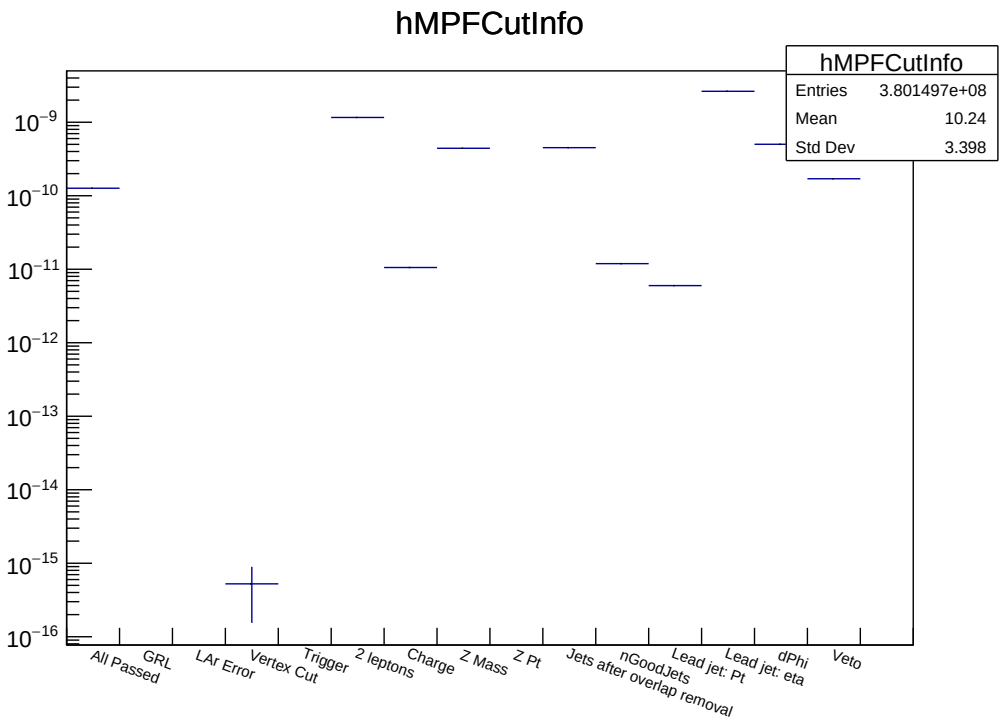

Figure C.21: The cutflow (each bin shows number of events that failed the corresponding cut) for PFlow in the Z$\rightarrow \mu\mu$ decay channel, for Sherpa.

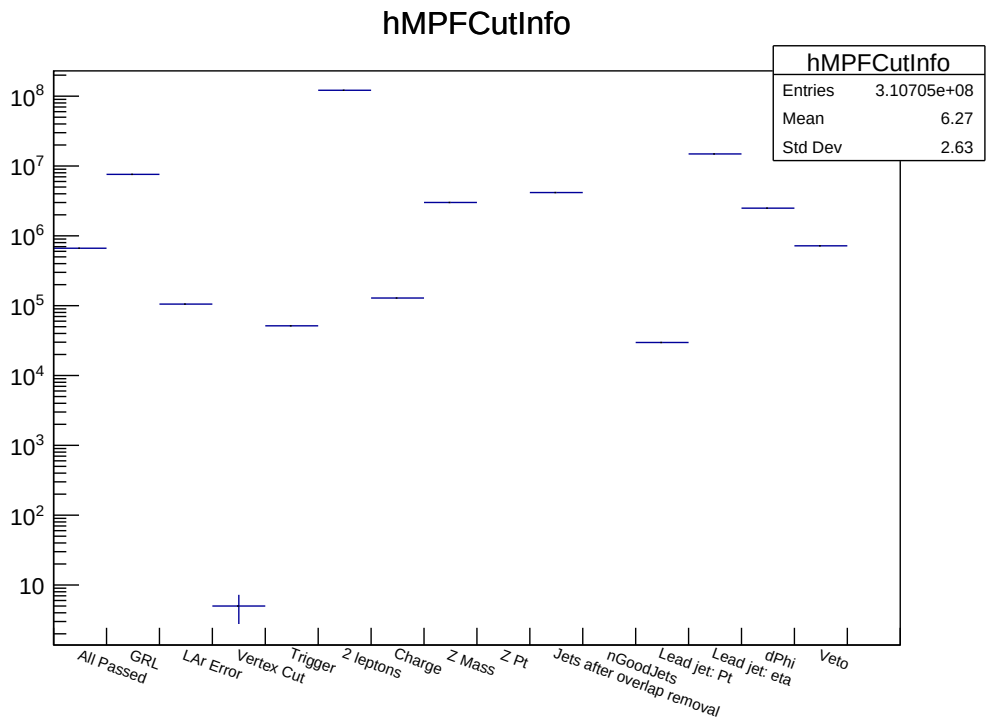

Figure C.22: The cutflow (each bin shows number of events that failed the corresponding cut) for PFlow in the Z→ *ee* decay channel, for all data years.

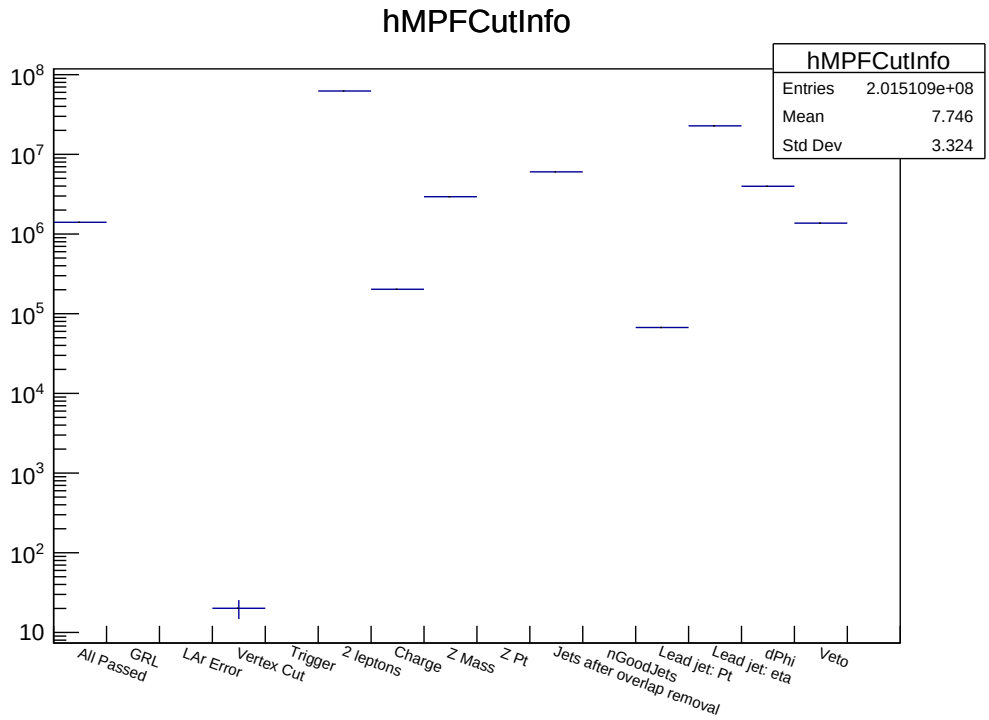

Figure C.23: The cutflow (each bin shows number of events that failed the corresponding cut) for PFlow in the Z→ *ee* decay channel, for Pythia.

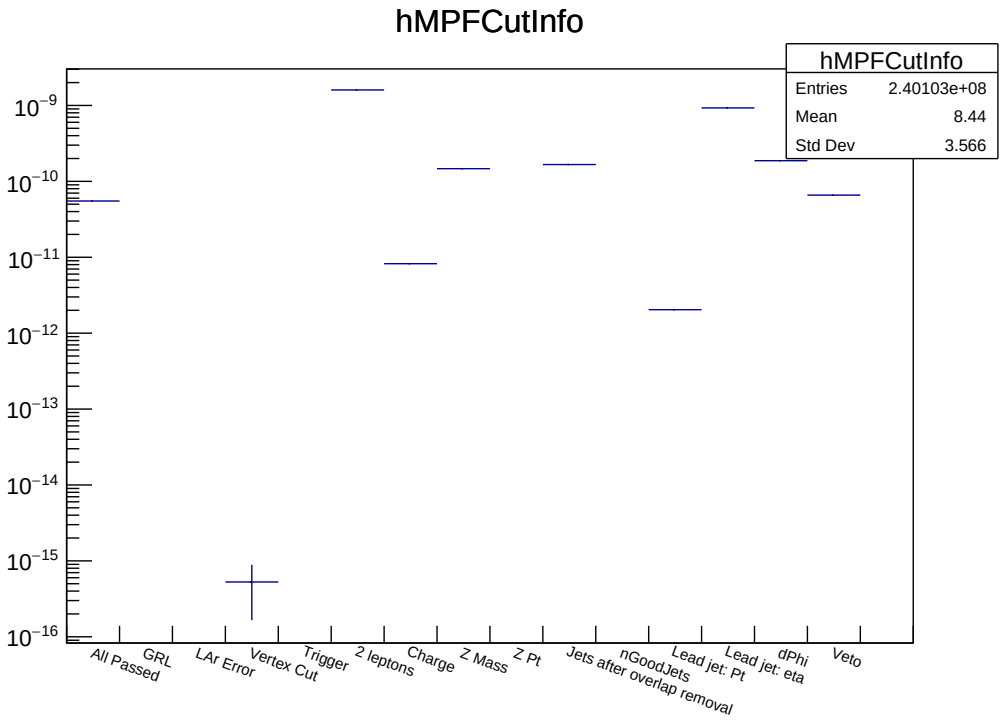

Figure C.24: The cutflow (each bin shows number of events that failed the corresponding cut) for PFlow in the Z→ *ee* decay channel, for Sherpa.